A

Structural, Thermodynamic and Equilibrium Study

of

Chiral Pendant Arm

Triaza Macrocyclic Ligand Complexes

Towards the formation of

Metal-Ion Activated

Molecular Receptors

A thesis submitted for the degree of

Doctor of Philosophy

at the

University of Adelaide (Faculty of Science)

by

Jennifer Megan Weeks

B.Sc. (Honours)

Department of Chemistry

To Mum and Dad

And in memory of
Grandma Weeks

Table of contents

Errata

On page 9, the sentence starting on line 3 should be replaced by:

Crystallographic studies show that the complex $[(NH_4)(18\text{-crown-}6)]^+$ has pseudo D_{3d} symmetry as do similar (18-crown-6) complexes formed with substituted ammonium ions.[60-62]

On page 51 in Table 2.4, the twist angle first twist angle should read $-7.3°$ not $-23.9°$.

Elsewhere, a few typographical corrections have been made by hand.

Acknowledgments

First and foremost, I would to extend my sincere gratitude to my supervisor Professor Stephen Lincoln for his guidance and support throughout this project. I would also like to thank him for the endless amount of career chats we had and his genuine interest in my future.

I would also like to thank all of the people in that I have worked and socialised with in the Chemistry Department. In particular, the Lincoln group 'lab boys' Mike, Lee, Oska and (more recently) Jason and also Mel, who have not only provided a great sounding board for ideas and problems, they have made the past three years a lot of fun. Also, a big thankyou is due for my very own 'on-call' computer administrator, Mike, for swiftly fixing all of my computer problems.

A special thankyou must also go to my housemates, Jen and Cam, and my close friends Georgie and Rikki who have been a huge support to me, especially in the last few months.

Finally, and most importantly, I would like to sincerely thank my family. My parents (Barry and Betty) have been the most support to me of all. I could not have done without their constant interest, advice and encouragement, not only in the past three years but also in the last twenty-five. I would like to thank Kaye, for her friendship, understanding and support, which has been so important to me. I would also like to thank Nick and Meg for their encouragement and support that constantly flows in all the way from Melbourne and my beautiful niece Amelia, whose gorgeous photo has played a huge part in limiting the stress involved in writing this thesis.

And to everyone... Am I finished yet? Yep!

Declaration

This work contains no material which has been accepted for the award of any other degree or diploma in any university or tertiary institution and, to the best of my knowledge and belief, contains no material previously published or written by another person, except where due reference has been made in the text.

I give consent to making this thesis available for copying or loan.

SIGNED: .   DATE: 24/12/99

Abstract

The study described in this thesis addresses the structural, equilibrium and thermodynamic aspects of the pendant arm donor triaza macrocyclic ligands 1,4,7-tris-((2S)-hydroxypropyl)-1,4,7-triazacyclononane, S-thpc9, 1,4,7-tris-((2S)-hydroxy-phenylethyl)-1,4,7-triazacyclononane, S-thpec9, 1,4,7-tris-((2S)-hydroxy-3-phenyl-propyl)-1,4,7-triazacyclononane, S-thppc9, and their alkali metal and zinc(II) complexes. It involves *ab initio* molecular modelling, X-ray crystallographic studies, potentiometric stability constant determinations and NMR kinetic studies.

The Gaussian 94 *ab initio* geometry optimisation calculations of tris-1,4,7-hydroxyethyl-1,4,7-triazacyclononane (thec9), 1,4,7-tris-((2S)-hydroxypropyl)-1,4,7-triazacyclononane (S-thpc9), 1,4,7-tris-((2S)-hydroxy-phenylethyl)-1,4,7-triazacyclononane (S-thpec9), 1,4,7-tris-((2S)-hydroxy-3-phenyl-propyl)-1,4,7-triazacyclononane (S-thppc9), and their alkali metal and zinc(II) complexes were performed. These calculations afforded structures that provide an insight into the structural aspects of the ligands and their metal complexes in the gas-phase. The steric requirements of the chiral pendant arms groups of the latter three ligands result in a preference of one diastereomeric conformation. The crystal structure of $[Zn(S\text{-thpc9})]^{2+}$ shows the complex to adopt a similar structure to that of the gas phase geometry optimised structure. The crystal structure of S-thpec9 shows the free ligand to adopt no particular diastereomer in the solid-phase.

The stability constants of the alkali metal and silver(I) complexes of S-thpc9, S-thpec9 and S-thppc9 were determined by potentiometric titrations and show each ligand to have selectivity for the lithium(I) ion.

Variable temperature ^{13}C NMR spectroscopy was used to study the diastereomeric exchange processes of S-thpc9, S-thpec9 and S-thppc9 and their lithium(I) and sodium(I) complexes in solution.

If the chiral pendant arms carry an aromatic substrate in addition to carrying a donor group, the possibility arises of using the coordination of a metal ion as a way of assembling a molecular receptor with a substantial cavity that arises from the juxtaposition of the aromatic groups. A brief outline of the preliminary host-guest complexation experiments performed with three potential guest molecules: tetraphenylborate, adamantane carboxylate and p-nitrophenolate is given. Electrospray techniques provided evidence for the existence of [Zn(S-thpec9)(tetraphenylborate)]$^+$ in solution, where tetraphenylborate is thought to occupy the receptor site.

Abbreviations

Å	Angstrom (10^{-10} m)
[Ag$^+$]	silver ion concentration
cyclen	1,4,7,11-tetraazacyclododecane
δ	chemical shift
dimethylformamide	N, N'-dimethylformamide
D_N	Guttman donor number
DNMR	dynamic nuclear magnetic resonance
E	electrode potential (volts)
E_0	standard electrode potential (volts)
ESI-MS	electrospray mass spectrometry
$\Delta H^{\ddagger}$	standard enthalpy
EXPT	experimental
I	ionic strength
K	stability (equillibrium) constant
$k_{298.2}$	rate constant (at 298.2 K)
k_B	Boltzmann's contant (1.3806×10^{-23} J K^{-1})
K_e	equilibrium constant
ln	natural logarithm (base e)
log	decadic logarithm (base 10)
M^{m+}	unspecified metal ion
Ms	milliseconds (10^{-3}s)
NMR	nuclear magnetic resonance
ppm	parts per million
R-thpec12	tetrakis-1,4,7,11-((2R)-hydroxyphenylethyl)-1,4,7,11-tetraazacyclododecane
$\Delta S^{\ddagger}$	standard entropy
S-thpc9	tris-1,4,7-((2S)-hydroxypropyl)-1,4,7-triazacyclononane

S-thpc12	tetrakis-1,4,7,11-((2*S*)-hydroxypropyl)-1,4,7,11-tetraazacyclododecane
S-thpec9	tris-1,4,7-((2*S*)-hydroxyphenylethyl)-1,4,7-triazacyclononane
S-thpec12	tetrakis-1,4,7,11-((2*S*)-hydroxyphenylethyl)-1,4,7,11-tetraazacyclododecane
S-thppc9	tris-1,4,7-((2*S*)-hydroxy-3-phenylpropyl)-1,4,7-triazacyclononane
S-thppc12	tetrakis-1,4,7,11-((2*S*)-hydroxy-3-phenylpropyl)-1,4,7,11-tetraazacyclododecane
T	temperature (K)
T_1	longtitudinal relaxation time (s)
T_2	Transverse relaxation time (s)
tacn	1,4,7-triazacyclononane
thec9	tris-1,4,7-(hydroxyethyl)-1,4,7-triazacyclononane
thec12	tetrakis-1,4,7,11-(hydroxyethyl)-1,4,7,11-tetraazacyclododecane
tmec9	tris-1,4,7-(methoxyethyl)-1,4,7-triazacyclononane
tmec12	tetrakis-1,4,7,11-(methoxyethyl)-1,4,7,11-triazacyclododecane

CHAPTER 1

Introduction

The significant attention polyaza macrocyclic ligands have attracted over the past decade has been predominantly due to the interesting properties of their metal complexes when compared to their non-cyclic analogues. Such properties include a high thermodynamic and kinetic stability (the macrocyclic effect), unusual spectral and magnetic properties, novel coordination geometries and the ability to stabilise unusual oxidation states.[1, 2, 3] Polyaza macrocycles are also involved in a number of fundamental biological processes, such as the mechanism of photosynthesis (the chlorin ring in chlorophyll) and the transport of oxygen in respiratory systems (the porphyrin ring of the iron containing haem proteins).[1] A considerable amount of research involving synthetic polyaza macrocycles has been directed towards the preparation of model compounds for naturally occurring macrocycles, such as these, with the purpose of developing an understanding of the metal ion environment which is of considerable importance in many living systems.[4-8]

Pendant arm donor macrocyclic ligands were created in an effort to combine the properties of the relatively rigid and kinetically stable macrocyclic structure with the more flexible and labile properties of the open-chain ligands.[1, 9-12] The term "pendant donor" macrocycle, as applied to a macrocyclic ligand that has had additional donor groups attached to its periphery, appears to have first been used in the chemical literature in 1980.[13] The first ligand of its type was reported some four years earlier.[14] However, the coining of the term paid formal recognition to

the importance of this structural motif as one with the potential to influence the direction of future research in a major way. By systematic variation of the pendant arm, the properties of the parent macrocycle may be tailored towards a number of interesting applications. By covalent attachment of a suitable organic group to the periphery of the macrocycle, metal ion promoted reactions such as ester, amide and nitrile hydrolysis may be studied.[13, 15, 16] Other applications include enzyme simulation,[17] the synthesis of iron sequestering agents for the treatment of acute iron poisoning,[18, 19] the attachment to monoclonal antibodies for the purpose of carrying a radionuclide to a targeted cell[20, 21] and as magnetic resonance imaging reagents for cancer therapy.[22] One of the major areas of current interest is in the design of ligands that are selective for particular metal ions.[23] In particular, research has been directed towards the design of ligands that are selective for toxic heavy metals such as Cd^{2+}, Hg^{2+} and Pb^{2+}. In this area, the use of pendant arms containing oxygen donor groups has proven to be particularly effective at altering the metal ion selectivity of ligands.[23-25]

Until the early 1980's, successful complexation of alkali metal ions had generally been achieved using ligands containing predominantly oxygen donor atoms, such as cryptands and crown ethers.[26-28] The stability of these complexes is strongly dependent on the 'size-match' compatibility of the ligand cavity and the ionic radius of the metal ion.[29, 30] As the cryptands were found to form stable complexes with the alkali metal ions as a consequence of their three-dimensional cavity,[30] it was anticipated that pendant arm macrocylic ligands would demonstrate some of their complexation properties. In addition to this, pendant arm donor polyaza macrocyclic ligands generally have an increased flexibility when compared to cryptands, and do not have as rigid or preformed a cavity. Thus, they can more readily adapt to the size of the metal ion without enhancing the inherent conformational strain associated with binding an incompatibly sized metal ion.

Unsubstituted tetra- and triaza macrocycles do not form detectable complexes with the alkali metal ions in aqueous solution, whereas they were found to complex strongly with transition and heavy metal ions.[9] It was thought that one way to

increase their affinity for alkali metal ions would be to add oxygen donor groups into the macrocyclic ring structure, or more readily, through the addition of oxygen donor pendant arms.

The tri- and tetraaza pendant donor macrocyclic ligands discussed in this study are cyclic tri- and tetraamines with the general structure and adopted trivial nomenclature shown in Figure 1.1. For example, the systematically named, 1,4,7-triazacyclononane is abbreviated to tacn. Similarly, the systematically named 1,4,7-tris(2-hydroxyethyl)-1,4,7-triazacyclononane is abbreviated to thec9, where the 'c9' represents the nine membered triaza macrocycle.

One of the first examples of alkali metal ion complexation with this type of ligand is the complexation of Li^+, Na^+ and K^+ by 1,4,7,10-tetrakis(2-hydroxyethyl)-1,4,7,10-tetraazacyclododecane (thec12) and their crystal structures are shown in Figure 1.2. In each case the metal ion is coordinated by all four nitrogen donors (sitting just above their common plane) and one, three and four oxygen donors, respectively. In the solid state, the ligand encapsulates the metal ion and the mode of binding appears to depend on the size of the metal ion as shown by an increase in coordination number as the ionic radii of the metal ions increase.

Subsequently, solution studies of the three-dimensional complexation of alkali metal ions by a number of pendant arm tetraaza macrocyclic ligands including thec12,[34] tmec12,[35] *S*-thpc12,[36] tmec14,[37] *S*-thpc14[37] and most recently *R*-thpec12,[38] have shown these complexes to exhibit stereochemistries and intramolecular processes unavailable to those of the parent macrocycle. Although pendant arm triaza macrocyclic systems have been involved in a number of investigations, most commonly towards biological applications such as biomimetic systems,[4-8, 39, 40] much less is known of the effects of pendant arm substitution of triaza macrocylic ligands on metal ion selectivity and their intramolecular exchange processes in solution.
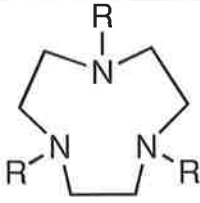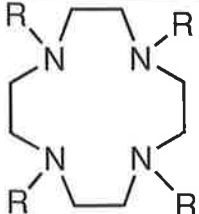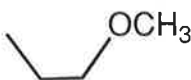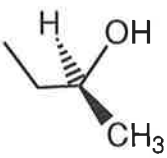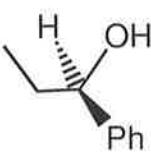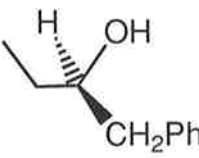
R	R (tacn)	R (cyclen)
H	tacn	cyclen
⎽⎽OH	thec9	thec12
⎽⎽OCH₃	tmec9	tmec12
H OH CH₃	(S)- or (R)-thpc9	(S)- or (R)-thpc12
H OH Ph	(S)- or (R)-thpec9	(S)- or (R)-thpec12
H OH CH₂Ph	(S)- or (R)-thppc9	(S)- or (R)-thppc12

Figure 1.1 Structures and trivial nomenclature of the tri- and tetraaza macrocyclic ligands and their pendant donor derivatives discussed in this study.
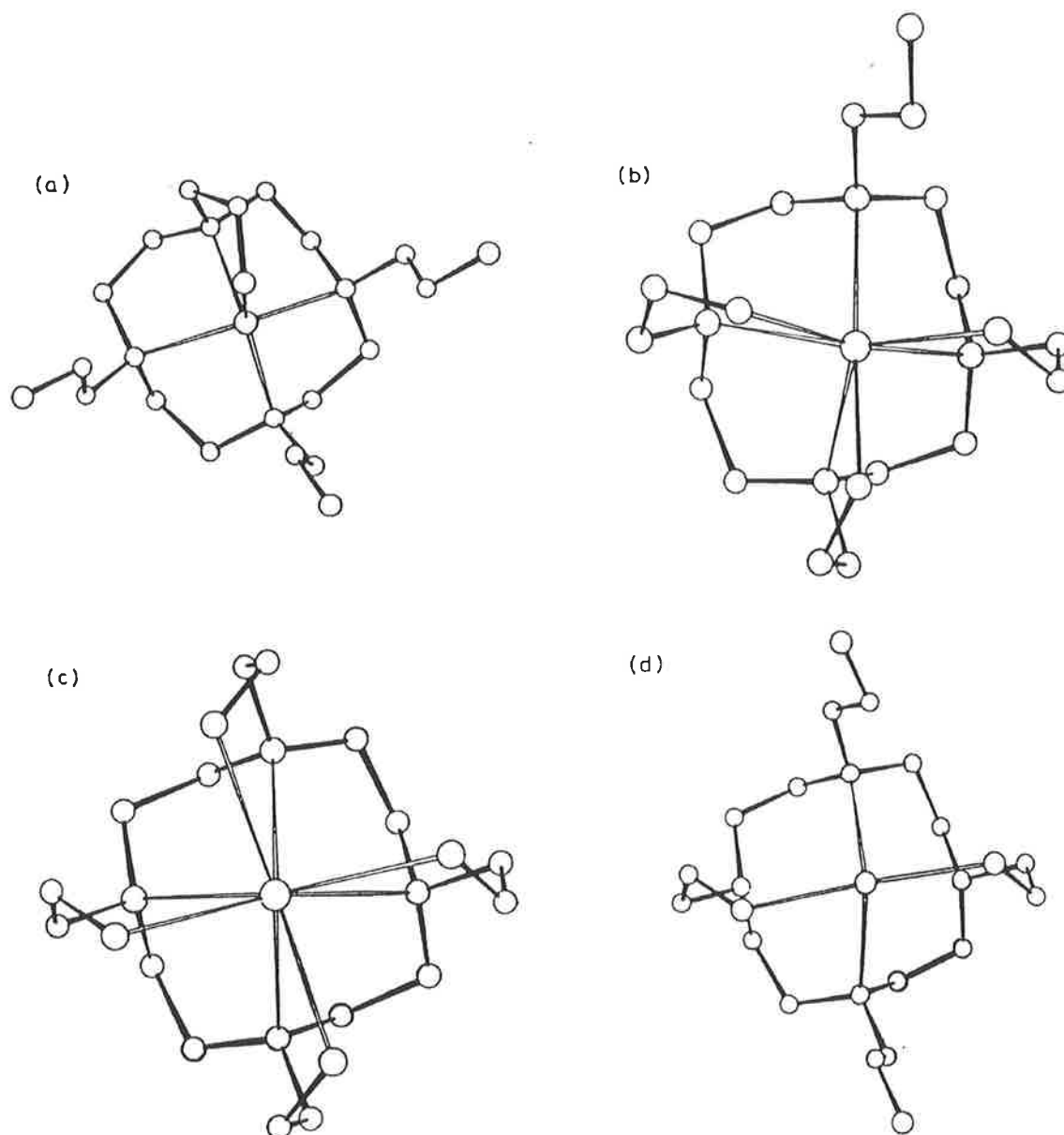
Figure 1.2   Solid state structures of the alkali metal complexes of thec12.[31-33] (a) [Li(thec12)]$^+$, (b) [Na(thec12)]$^+$, (c) [K(thec12]$^+$ and (d) thec12.H$_2$O.

1,4,7-Triazacylcononane (tacn) is too small a macrocycle to bind the metal ion in the plane of the nitrogen atoms and must bind facially, giving "sandwich" complexes[41] such as [Ni(tacn)2]$^{2+}$, or "piano stool" complexes[42] such as [Mo(tacn)(CO)$_3$Br]$^+$. Molecular mechanics calculations show that the +++ configuration is the most energetically favourable configuration for planar coordination of metal ions and thus is expected to be the most commonly adopted conformation of tacn.[43]
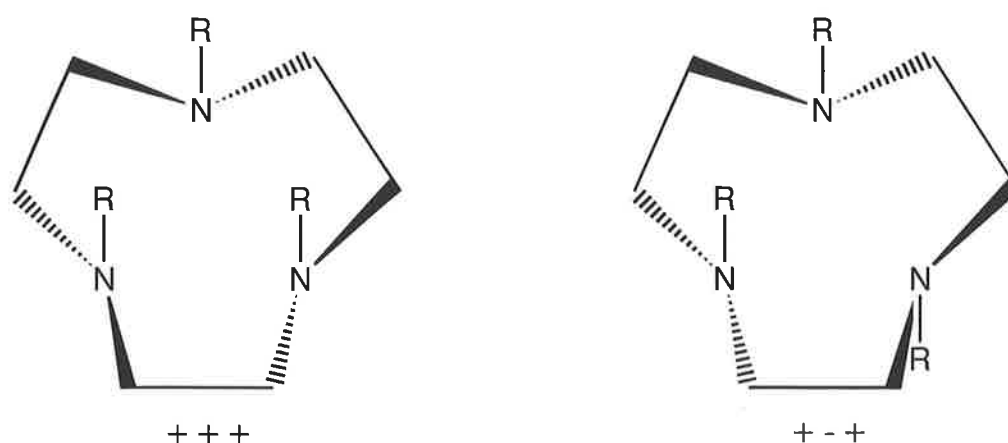
Figure 1.3   Possible configurational isomers of *N* substituted tacn.   The R groups orientated above the nitrogen plane are indicated with a +, while those below the plane are indicated with a -.

Consequently, pendant arm donor triaza macrocyclic ligands generally encapsulate a metal ion in a bifacial arrangement where the trigonal nitrogen plane is situated on one side of the metal ion and the trigonal oxygen plane on the other, often in a distorted trigonal prismatic arrangement (see Figures 1.4 and 1.5).[11, 39, 40, 44-47]

This study involves the pendant arm triaza macrocyclic ligands; *S*-thpc9, *S*-thpec9 and *S*-thpec9, and was prompted by the discovery of the enantiomeric exchange of the alkali metal complexes of thec9 in solution.[48]   It was anticipated that the incorporation of a chiral pendant arm would result in a thermodynamic preference

for one of the diastereomers and result in an induced homochirality of the secondary structure of the molecule.

This phenomen*on* has been observed in the crystal structures of many chiral pendant arm macrocycles including the chromium(III) and iron(III) complexes 1,4,7-tris-((2R)-2-propionoate)-1,4,7-triazacyclononane (Figures 1.4 and 1.5, respectively),[49] the yttrium(III) and lutetuim(III) complexes of 1,4,7-tris(carbamoylmethyl)-1,4,7-triazacyclononane[50] and the dimeric structures of a variety of transition metal complexes of S-thpc9.[39, 40, 51] The trigonal plane of the oxygen atoms twists either to the right (Δ) or left (Λ) of the trigonal plane of the nitrogens below (when looking directly down the C_3 axis) depending on the chirality of the pendant arm.[†] The steric requirements of the chiral pendant arms generate this homochirality over the secondary structure of the molecule.
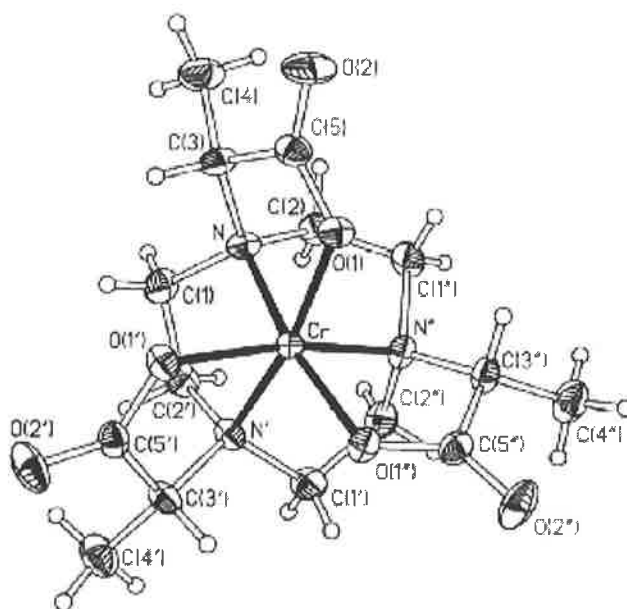
Figure 1.4   Crystal structure of Δ-[Cr(1,4,7-tris-((2R)-2-propionoate)-1,4,7-triaza-cyclononane] (The Δ conformation is assigned to the convention used throughout this thesis).[49]

[†] When the oxygen plane is twisted to the right with respect to the nitrogen this is termed Δ and when the oxygen plane is twisted to the left this is term Λ. It should be noted that this differs from the convention where the chelated arms are viewed as propeller blades and in some cases can lead to the opposite designation by the two conventions.
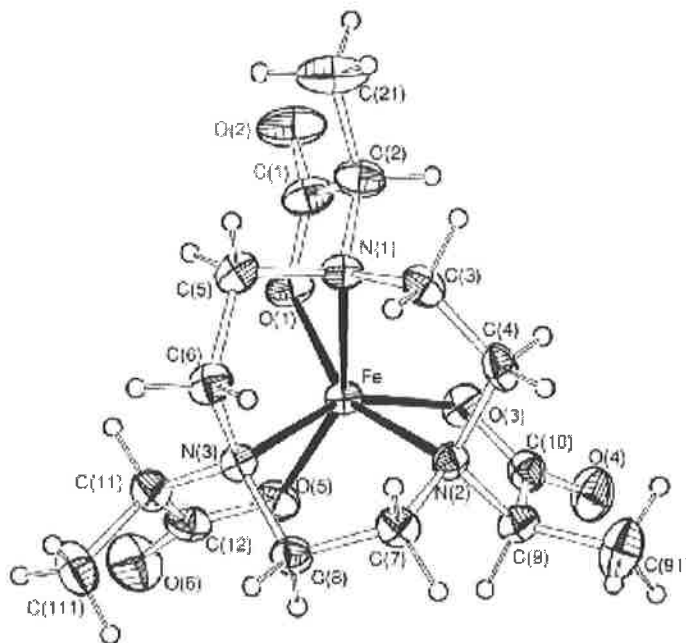
Figure 1.5   Crystal structure of Δ-[Fe(1,4,7-tris-((2*R*)-2-propionoate)-1,4,7-triaza-cyclononane] (The Δ conformation is assigned to the convention used throughout this thesis).[49]

Molecules such as these have attracted a great deal of interest due to their potential applications in many fields of research. This is exemplified by studies of chiral recognition, the organisation of amino acids in biomimetic studies,[52] magnetic resonance imaging contrast agents,[53-55] the detection of anion binding,[56] the chiral induction of electron transfer reactions[49] and here, molecular recognition and binding of guest molecule.[38, 57]

If the chiral pendant arms carry an aromatic substituent in addition to a donor group, the possibility arises of using the coordination of a metal ion as a way of assembling a molecular receptor with a substantial cavity that arises from the juxtaposition of the aromatic groups.

Host-guest complexation should be optimal when the symmetry of the guest is similar to that of the receptor. For instance, macrocycles designed for the potential

enantiomeric recognition of amino-acids contain a molecular frame of 18-crown-6 and related macrocycles possessing D_{3d} symmetry since this matches the molecular symmetry of NH_3 (C_{3v}).[58, 59] Crystallographic studies show that the complex cation [$(NH_4)(18$-crown-6$)]^+$ has a pseudo D_{3d} symmetry and has shows the macrocyclic ring to retain its D_{3d} symmetry, as is also the case with various substituted ammonium ions.[60-62]

By variation of the macrocylic backbone, the pendant arms and the complexed metal ion, the shape and symmetry of the cavity can be 'tuned' for optimal compatibility with, and the potential selectivity for, a diverse range guest molecules with differing symmetry requirements.

Recent successful host-guest complexation of this type has been achieved using the cadmium(II) complex of 1,4,7,10-tetrakis((2S)-hydroxy-3-phenoxypropyl)-1,4,7,10-tetraazacyclododecane (S-thphpc12) to form a ternary complex with guests such as *p*-nitrophenolate and *p*-toluene sulphonate which include in the receptor cavity formed by the chiral pendant arm phenoxy groups.[57] A crystal structure of the ternary complex with *p*-toluene sulphonate is shown in Figure 1.6.

The study described in this thesis addresses the structural, equilibrium and thermodynamic aspects of the pendant arm donor triaza macrocyclic ligands 1,4,7-tris-((2S)-hydroxypropyl)-1,4,7-triazacyclononane, S-thpc9, 1,4,7-tris-((2S)-hydroxyphenylethyl)-1,4,7-triazacyclononane, S-thpec9, , 1,4,7-tris-((2S)-hydroxy-3-phenylpropyl)-1,4,7-triazacyclononane, S-thppc9, and their alkali metal and zinc(II) complexes. It involves *ab initio* molecular modelling, X-ray crystallographic studies, potentiometric stability constant determinations and NMR kinetic studies.

It is intended that the study should extend and complement the current understanding of the metal complexes of macrocyclic ligands in addition to providing an insight into the structural and equilibrium characteristics of these ligands as potential molecular receptors. Each ligand studied shows C_3 symmetry and so host guest complexation with anionic guest of similar symmetry should be optimal. Following the initial discussion is a brief outline of the preliminary host-

guest complexation experiments performed with three potential guest molecules: tetraphenylborate (C_3), adamantane carboxylate (pseudo C_3) and *p*-nitrophenolate (C_{2v}).
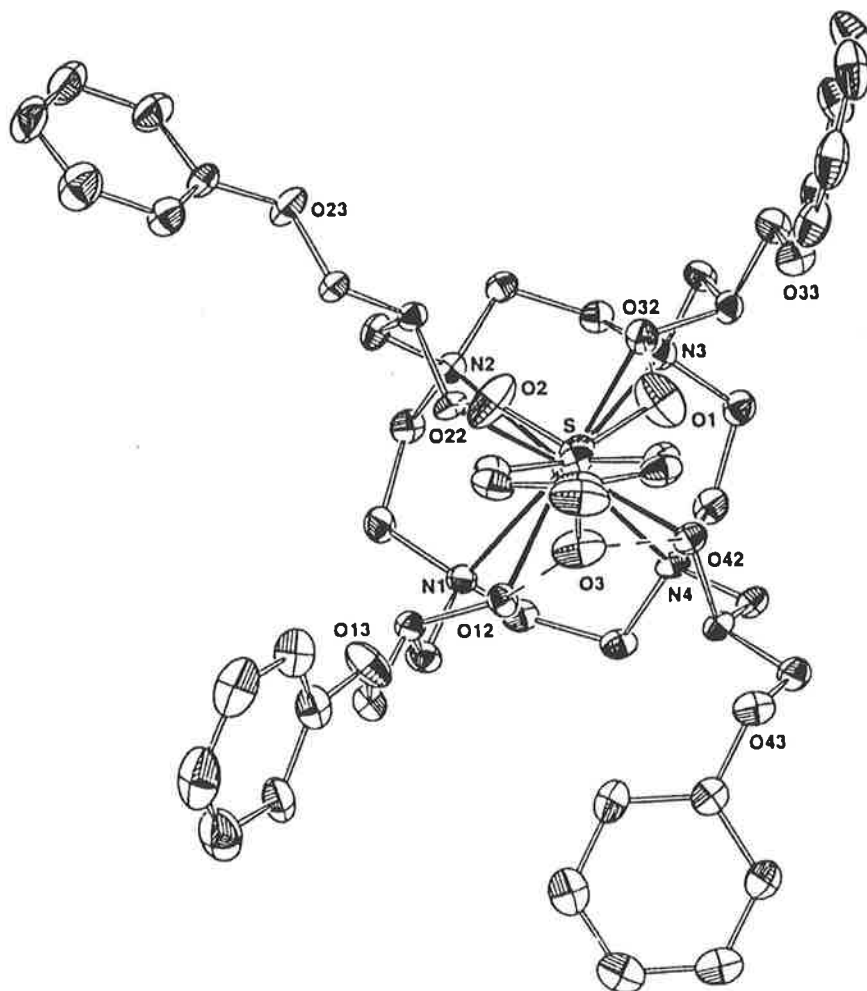
Figure 1.6 Crystal structure of the inclusion cation, [Cd(*S*-thphpc12)(p-toluenesulfonate)]⁺, viewed perpendicular to the plane of the of the hydroxyl oxygen atoms. Hydrogen atoms are omitted.[57]

References

1.   L. F. Lindoy, *The Chemistry of Macrocyclic Ligand Complexes*. 1989, Cainmbridge, England: Caimbridge University Press.

2.   V. J. Thom, J. C. A. Boeyens, G. J. Mcdougall and R. D. Hancock, *Journal of the American Chemical Society*, 1984. **106**, 3198-3207.

3.   G. A. Melson, *Coordination Chemistry of Macrocyclic Compounds*. 1979, New York: Plenum.

4.   D. J. Szalda, E. Fujita and C. Creutz, *Inorganic Chemistry*, 1989. **28**, 1446-1450.

5.   E. Fujita, D. J. Szalda, C. Creutz and N. Sutin, *Journal of the American Chemical Society*, 1988. **110**, 4870-4871.

6.   E. Kimura, T. Shiota, T. Koike, M. Shiro and M. Kodama, *Journal of the American Chemical Society*, 1990. **112**, 5805-5811.

7.   M. Kato and T. Ito, 1985. **24**, 504-508.

8.   M. Kodama and E. Kimira, *Journal of the Chemical Society, Dalton Transactions*, 1980, 327-333.

9.   T. A. Kaden, *Topics of Current Chemistry*, 1984. **121**, 154-170.

10.   P. V. Bernhardt and G. A. Lawrence, *Coordination Chemistry Reviews*, 1990. **104**, 207.

11.   K. P. Wainwright, *Coordination Chemistry Reviews*, 1997. **166**, 35-90.

12.   S. F. Lincoln, *Coordination Chemistry Reviews*, 1997. **166**, 255.

13.   K. P. Wainwright, *Journal of the Chemical Society, Dalton Transactions*, 1980, 2117-2120.

14.   H. Stetter and W. Frank, *Angewante Chem*, 1976. **15**, 686.

15.   D. Tschudin and T. A. Kaden, *Pure and Applied Chemsitry*, 1988. **60**, 489-493.

16.   T. A. Kaden, *Pure and Applied Chemistry*, 1988. **60**, 1117-1122.

17.   E. Kimura, Y. Kodama, T. Koike and M. Shiro, *Journal of the American Chemical Society*, 1995. **117**, 8304.

18.   F. L. Weitl and K. N. Raymond, *Journal of the American Chemical Society*, 1979. **101**, 2728-2731.

19. C. Bazzicalupi, A. Bencini, A. Bianchi, V. Fusi, C. Giorgi, L. Messori, M. Migliorini, P. Paoletti and B. Valtancoli, *Journal of the Chemical Society, Dalton Transactions*, 1998, 359-367.

20. D. Parker, *Chemistry in Britain*, 1990, 942.

21. D. Parker, *Chemical Society Reviews*, 1990. **19**, 271.

22. D. D. Dischino, E. J. Delaney, J. E. Emswiler, G. T. Gaughan, J. S. Prasad, S. K. Srivastava and M. F. Tweedle, *Inorganic Chemistry*, 1991. **30**, 1265.

23. R. D. Hancock, *Perspective Coordination Chemistry*, 1993, 129-151.

24. R. D. Hancock, *Pure and Applied Chemistry*, 1993. **65**, 941-946.

25. R. D. Hancock, *Chemical Reviews*, 1989. **89**, 1875-1914.

26. A. I. Popov and J.-M. Lehn, *Coordination Chemistry of Macrocyclic Compounds*, ed. G.A. Melson. 1979, New York: Plenum Press.

27. G. W. Gokel, *Crown Ethers and Cryptands*. 1991, Caimbridge: The Royal Society of Chemistry.

28. C. J. Pederson, *Journal of the American Chemical Society*, 1967. **89**, 2495.

29. J.-M. Lehn, *Accounts of Chemical Research*, 1988. **11**, 49.

30. B. G. Cox, R. Garcia-Rosas and H. Schneider, *Journal of the Amercican Chemical Society*, 1981. **103**, 1384.

31. P. Groth, *Acta Chimica Scandinavia*, 1983. **A37**, 283.

32. P. Groth, *Acta Chimica Scandinavia*, 1983. **A37**, 711.

33. S. Buoen, J. Dale, P. Groth and J. Krane, *Journal of the Chemical Society, Chemical Communications*, 1982, 1172.

34. A. K. W. Stephens and S. F. Lincoln, *Journal of the Chemical Society, Dalton Transactions*, 1993, 2123.

35. A. K. W. Stephens, R. S. Dhillon, S. E. Madbak, S. L. Whitbread and S. F. Lincoln, *Inorganic Chemistry*, 1996. **35**, 2019-2024.

36. R. Dhillon, S. E. Madbak, F. G. Ciccone, M. A. Buntine, S. F. Lincoln and K. P. Wainwright, *Journal of the American Chemical Society*, 1997. **119**, 6126.

37. J. Lucas, *Reaction Dynamics of Some Pendant Arm Macrocycles*, in *Chemistry*. 1994, Adelaide: Adelaide.

38. S. L. Whitbread, P. Valente, M. A. Buntine, P. Clements, S. F. Lincoln, R. T. M and K. P. Wainwright, *Journal of the American Chemical Society*, 1998. **43**, 120.

39. A. A. Belal, I. Fallis, L. J. Farrugia, N. M. Macdonald and R. D. Peacock, *Journal of the Chemical Society, Chemical Communications*, 1991, 402-403.

40. I. Fallis, L. J. Farrugia, N. M. Macdonald and R. D. Peacock, *Inorganic Chemistry*, 1993. **32**, 779-780.

41. L. J. Zompa and T. N. Margulis, *Inorganica Chimica Acta*, 1978. **28**, L157.

42. P. Chaudhuri, K. Weighardt, Y.-H. Tsai and C. Kruger, *Inorganic Chemistry*, 1982. **23**, 427.

43. R. D. Hancock and A. E. Martell, *Chemistry Reviews*, 1989. **89**, 1875.

44. H. Z. Cai and T. A. Kaden, *Helvetica Chimica Acta*, 1994. **77**, 383-.

45. A. A. Belal, P. Chaudhuri, I. Fallis, L. J. Farrugia, R. Hartung, N. M. Macdonald, B. Nuber, R. D. Peacock, J. Weiss and K. Weighardt, *Inorganic Chemistry*, 1991. **30**, 4397-4402.

46. B. A. Sayer, J. P. Michael and R. D. Hancock, *Inorganica Chimica Acta*, 1983. **77**, L63-L64.

47. J. Huskens and A. D. Sherry, *Chemical Communications*, 1997, 845-846.

48. S. L. Whitbread, J. M. Weeks, P. Valente, M. A. Buntine, S. F. Lincoln and K. P. Wainwright, *Australian Journal of Chemistry*, 1997. **50**, 853.

49. D. A. Dixon, M. Shang and G. Lappin, *Inorganica Chimica Acta*, 1999. **290**, 197.

50. A. Shahid, C. Marks, L. M. Toomey, M. R. Churchill and J. R. Morrow, *Inorganica Chimica Acta*, 1996. **246**, 99.

51. A. A. Belal, L. J. Farrugia, R. D. Peacock and J. Robb, *Journal of the Chemical Society, Dalton Transactions*, 1989, 931-935.

52. A. A. Watson, A. C. Willis and D. P. Fairlie, *Inorganic Chemistry*, 1997. **36**, 752.

53. D. Parker and J. A. Gareth Williams, *Journal of the Chemical Society, Dalton Transactions*, 1996, 3613.

54. H. G. Brittain and J. F. Desreux, *Inorganic Chemistry*, 1984. **23**, 4459.

55. D. Parker, P. Kanthi Senanyake and J. A. Gareth Williams, *Journal of the Chemical Society, Perkin Transactions*, 1998, 2.

56. R. S. Dickens, T. Gunnlaugsson, D. Parker and R. D. Peacock, *Journal of the Chemical Society, Chemical Communications*, 1998, 1643.

57. C. B. Smith, K. S. Wallwork, J. M. Weeks, M. A. Buntine, S. F. Lincoln, M. R. Taylor and K. P. Wainwright, *Inorganic Chemistry*, 1999. **38**, 4986.

58. M. J. Bovil, D. J. Chadwick, I. O. Sutherland and D. J. Watkin, *Journal of the Chemical Society. Perkin Transactions 2*, 1980, 1529.

59. I. Goldberg, *Inclusion Compounds*, ed. J.L. Atwood, J.E.D. Davies, and D.D. Macnicol. Vol. 2. 1984, London: Academic Press.

60. D. A. Pears, J. F. Stoddart, M. E. Flakey, B. L. Allwood and D. J. Williams, *Acta Crystallographica*, 1988. **C44**, 1426.

61. O. Nagana, A. Kobayashi and Y. Sasaki, *Bulletin of the Chemical Society of Japan*, 1989. **62**, 2807.

62. X. X. Zhang, J. S. Bradshaw and R. M. Izatt, *Chemistry Reviews*, 1997. **97**, 3313.

Chapter 2

Molecular Modelling
of four
Pendant Arm Triaza Macrocyclic Ligands
and their
Alkali Metal Complexes

2.1   Introduction to molecular modeling

Molecular modelling, or computational chemistry, can provide an invaluable supplement to experimental chemistry as it can offer a useful guide to problem solving in many genres of chemistry. It can provide a visualisation that is often a vital adjunct to experimental studies and in the development of new unexplored concepts.

Molecular modelling simulates chemical structures and reactions numerically, based in full or in part on the fundamental laws of physics. It allows a chemist to predict the outcome of a reaction or a structure of a particular compound by running calculations on a computer rather than by experimental studies. It can also be used to provide information on chemical phenomena which is impossible to obtain through observation, such as short-lived, unstable intermediates and transition states.[1]

In this study, molecular modelling has been used to predict the minimum energy conformations of the four triaza macrocylic pendant arm ligands tris-(hydroxyethyl)-1,4,7-triazacyclononane (thec9), tris-((2*S*)-hydroxypropyl)-1,4,7-triazacyclononane (*S*-thpc9), tris-((2*S*)-hydroxyphenylethyl)-1,4,7-triazacyclononane (*S*-thpec9) and tris-((2*S*)-hydroxy-3-phenylpropyl)-1,4,7-triazacyclononane (*S*-thppc9), and their alkali metal and zinc(II) complexes. The resulting structures have provided a valuable insight into the rationalisation of the outcomes of the experimental ^{13}C NMR and

metal complex stability studies. Molecular modelling has also been used in this study to predict the adopted conformation of a host guest complex.

2.2 A theoretical background to geometry optimisation calculations

Geometry optimisation calculations involve the location of the minimum energy conformation of a particular molecule. In principle, geometry optimisation calculations will eventually arrive at a global minimum. However this process can be facilitated by the users own chemical knowledge of the likely structure (Figure 2.1).
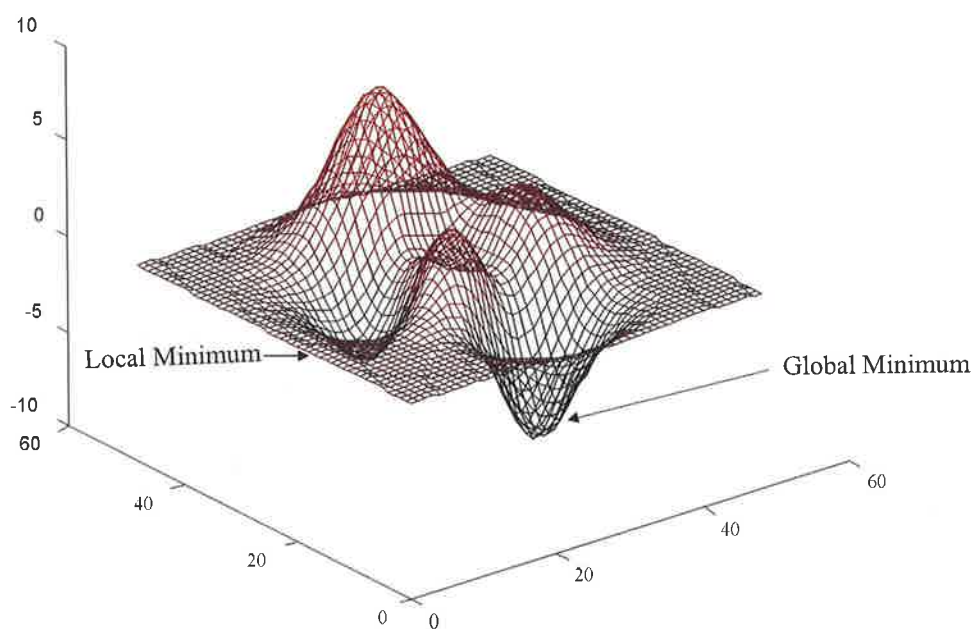
Figure 2.1 A potential energy surface.

2.2.1 Electronic structure methods

The calculations performed in this study were based on electronic structure methods, which utilise the laws of quantum mechanics rather than the laws of classical physics used in molecular mechanics calculations.[1]

Quantum mechanics states that the energy and other related properties of a molecule may be obtained by solving the Schrödinger equation:

$$H\Psi = E\Psi \qquad\qquad 2.1$$

where H is termed the Hamiltonian operator, E the energy of the system and Ψ is the wavefunction of the positions and momenta of the particles.[1]

For any but the smallest systems, exact solutions to the Schrödinger equation are not computationally practical and some mathematical approximations are necessary as a compromise between computational speed and accuracy of results. Electronic structure methods are characterised by their various mathematical approximations to its solution.[1]

There are two major classes of electronic structure methods; *semi-empirical* and *ab initio* methods.

Semi-empirical methods use parameters derived from experimental data to simplify the calculation. They solve an approximate form of the Schrödinger equation that depends on having appropriate parameters available for the type of chemical system under investigation. Semi-empirical calculations are relatively inexpensive with respect to computational power and time required. They provide reasonable qualitative descriptions of energies and structures for systems where a good parameter set exists.[1-3]

Ab initio is the Latin term for "first principles". This computational method is based solely on the laws of quantum mechanics and three physical constants; the speed of

light, the masses and charges of electrons and nuclei and Plank's constant. Unlike molecular mechanics and semi-empirical and methods, *ab initio* methods require no experimental parameters for the calculations.[1-3]

In contrast with semi-empirical methods, *ab initio* methods offer high quality quantitative predictions for a broad range of systems without being limited to any specific type of system. Modern *ab initio* programs in the Gaussian 94 suite[4] can predict the structure of molecules containing up to one hundred atoms and can handle any atom type, including metals.

The calculations performed in this study were done through Gaussian 94 and using *ab initio* methods. As an exact solution to the Schrödinger equation is not possible for any but the most trivial molecular systems mathematical approximations are used. Gaussian 94 provides a hierarchy of approximation methods corresponding to a number of different levels of theory. The higher the level of theory, the more accurate the calculation and the more computationally expensive it becomes.[1]

The model chemistry used for a geometry optimisation calculation generally consists of a combination of a chosen level of theory along with an appropriate basis set. A basis set provides a mathematical description of the orbitals within a system that is required to perform the theoretical calculation. In the true quantum mechanical picture, electrons have a finite probability of existing anywhere in space and larger basis sets more accurately approximate the orbitals by imposing fewer restrictions in the locations of electrons in space.

Hartree-Fock Theory is the crudest level of *ab initio* theory, as it does not take electron correlation effects into consideration. It approximates each electron to "see" all of the other electrons as an average distribution so that there are no instantaneous electron-electron interactions included. Taking electron correlation into account is important for accurate modelling of the energetics of reactions and bond dissociation but is not imperative in geometry optimisation studies[1]. As the purpose of this study has been to predict the gas phase conformations of various ligands and their metal complexes, Hartree-Fock Theory has been sufficient.

The LANL2DZ basis set is one that includes all elements of the periodic table, from hydrogen up to bismuth[1]. For the first row elements, the atoms are treated using the D95 [5] basis set and for the larger atoms, electrons near the nucleus are treated in an approximate way using effective core potentials (ECP's).[6-8] As complexes incorporating potassium(I), rubidium(I) and caesium(I) were studied, a basis set such as LANL2DZ was required and was found to have sufficient accuracy while remaining computationally practical for most of the geometry optimisation calculations performed.

For the bigger systems under investigation the LANL2DZ basis set was less practical to use as the calculations were taking three to four months to complete. For this reason, the LANL2MB basis set was used for the geometry optimisations of the sodium(I) to caesium(I) complexes of *S*-thppc9. This basis set still uses ECP's, but compromises the level of theory of the calculation by using a cruder basis set for the first row elements (STO-3G) [9, 10] and by treating the atoms sodium to bismuth in a more simplified way.[6-8]

For the single point energy calculations of the LANL2DZ minimised structures, the STO-3G** [9-11] basis set was utilised. This basis set treats all atoms from hydrogen up to xenon consistently. Unlike the LANL2DZ and LANL2MB basis sets, STO-3G** does not use effective core potential values in the treatment of atoms past the first row. These calculations were required for the development of a gas-phase 'stability series' for which consistent treatment of all atoms was necessary to enable the comparison of final energy values. This series of calculations has provided an insight for the size match compatibility of ligand and metal ion in the absence of solvent effects.

It is important to note that all geometry optimisation calculations performed were carried out in the gas phase, which restricted the possibility of direct comparison with solution kinetic and equilibrium studies. However, they have provided a reasonable guide and a visualisation that has been very important in interpreting experimental studies.

Also included in this chapter are the crystal structures of *S*-thpec9 and [Zn(*S*-thpc9)].1.5ClO$_4$.0.5Cl.

2.3 Geometry optimisation calculations for 1,4,7-tris(hydroxy)-1,4,7-triazacyclononane (thec9) and its alkali metal complexes

2.3.1 Enantiomeric exchange of thec9 and [Na(thec9)]$^+$

Variable temperature ^{13}C NMR studies suggest hexadentate thec9 and its alkali metal complexes to exist as two rapidly converting enantiomers in solution (Figure 2.2).[12] The ligand cavity forms a distorted trigonal prismatic geometry where the triangular plane formed by the oxygen atoms can either twist to the right (Δ) or to the left (Λ) of the triangular plane formed by the nitrogen donors below.

<center>Λ Δ</center>
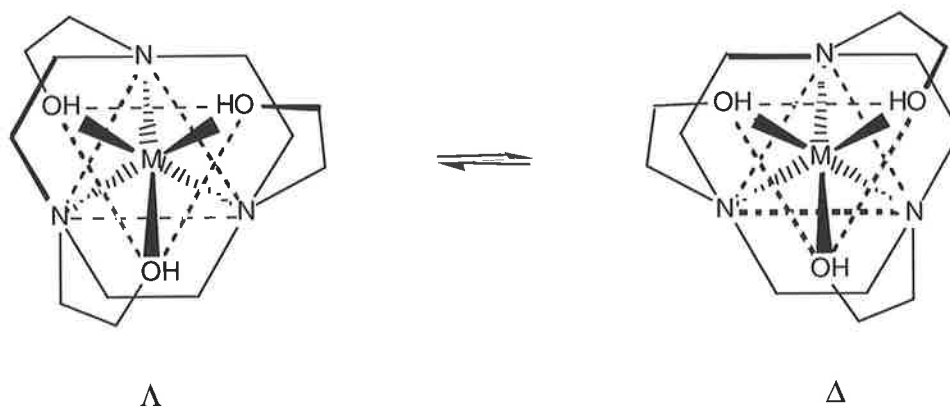
Figure 2.2 The delta (Δ) and lambda (Λ) enantiomers of [M(thec9)]$^{m+}$ shown in equilibrium.

Further evidence for the existence of the two enantiomers was sought after through gas phase geometry optimisation calculations.

The two global energy minimised structures located were equal in energy and were consistent with the Λ and Δ isomers predicted (Figure 2.3).

Λ   Δ
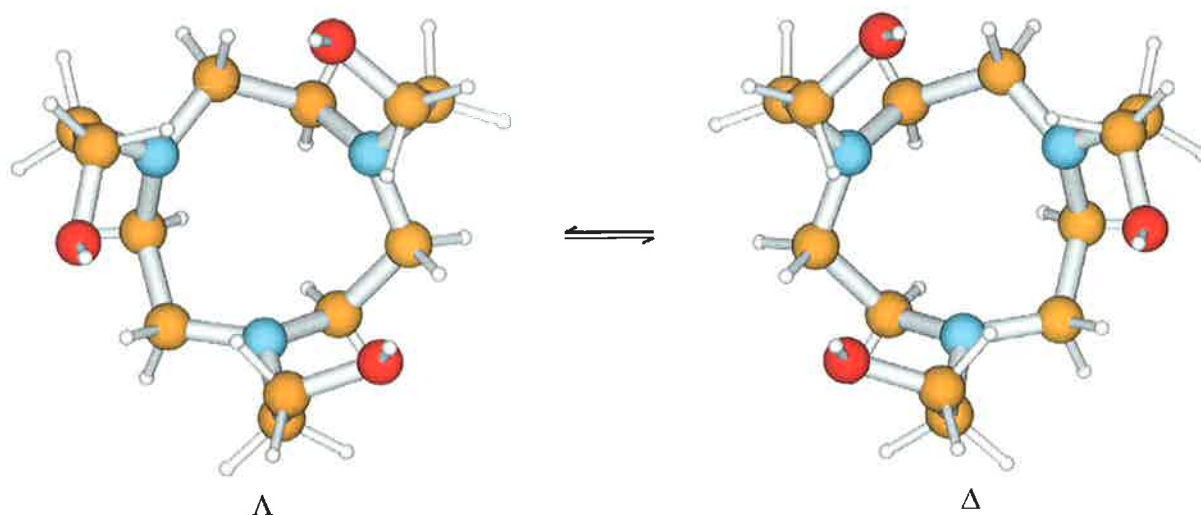
Figure 2.3 Gaussian 94 LAN2DZ geometry optimised structures of thec9 showing the Λ and Δ enantiomers, respectively.

The triangular plane formed by the oxygen atoms was found to either twist to the right (Δ) or to the left (Λ) of the triangular plane formed by the nitrogen donors below. The macrocyclic carbons were found to flip from an 'up-down, up-down, up-down' to a 'down-up, down-up, down-up' configuration clockwise around the ring when exchanged from the Λ to the Δ enantiomer.

A similar result was found for the sodium(I) complex of thec9 (Figure 2.4). The distorted prismatic ligand cavity of the sodium(I) complex was also found to either twist to the left or to the right, resulting in two equal global minima of the Λ and Δ conformations.
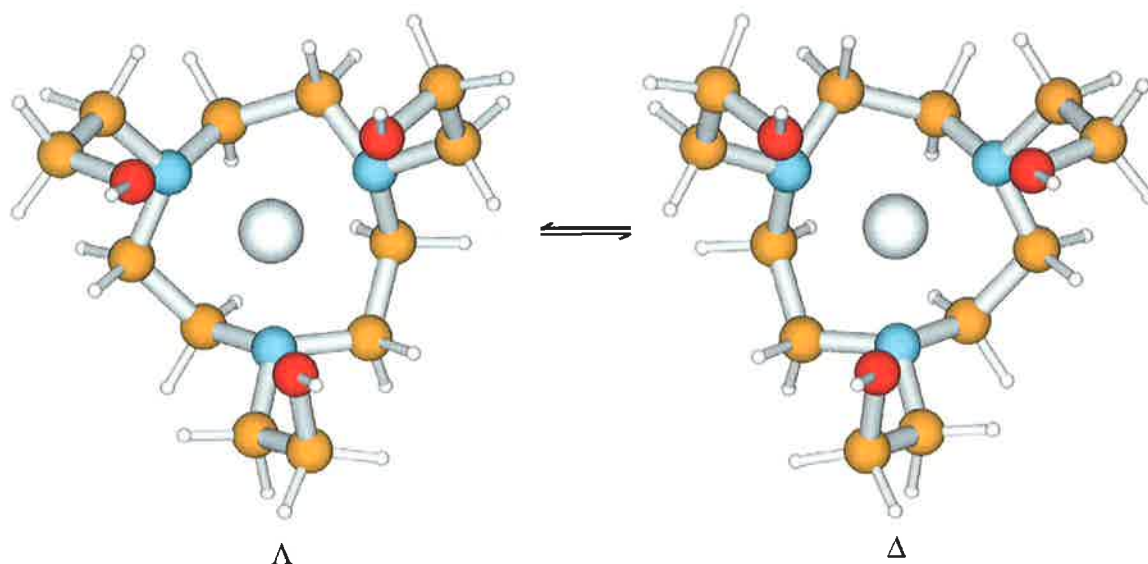
Figure 2.4   Gaussian 94 LANL2DZ geometry optimised structures of $[Na(thec9)]^+$ showing the Λ and Δ enantiomers, respectively.

2.3.2 Geometry optimisation calculations for the alkali metal complexes of thec9

For the remaining group (I) metals, only the Δ conformation was modelled as the second global minima, corresponding to the Λ enantiomer, is an exact mirror image of the Δ conformation modelled. The optimised structures for these are shown in Figures 2.5 through to 2.9 and the relevant distances and angles are shown in Table 2.1.

The pendant arms were found to adopt the +++ configuration (Figure 1.3) for both the free ligand and its group (I) metal ion complexes (Figures 2.5-2.9).
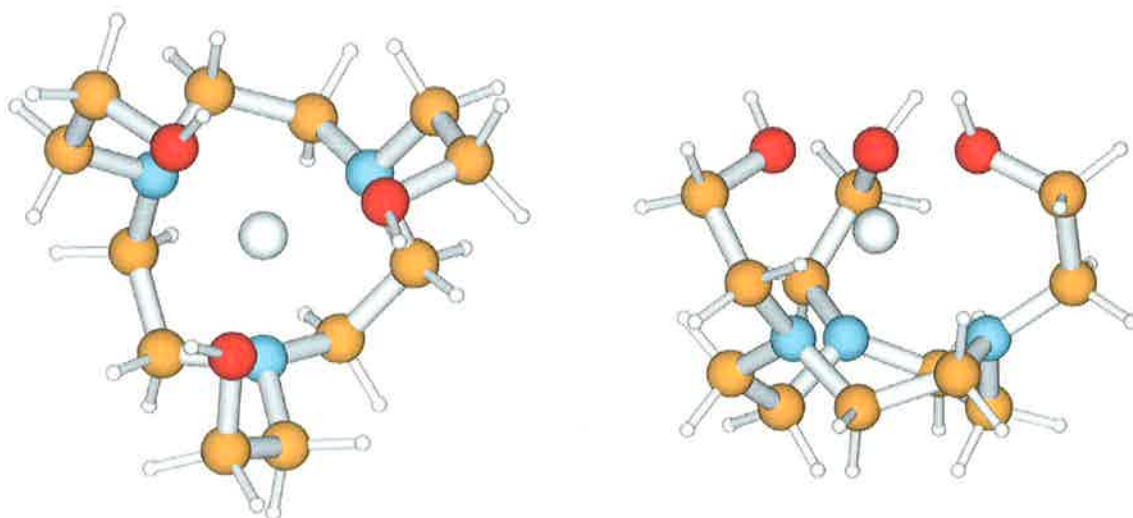
Figure 2.5 A view down and perpendicular to the C_3 axis of the Gaussian 94 LANL2DZ geometry optimised structure of [Li(thec9)]$^+$ on the left and right of the diagram, respectively.
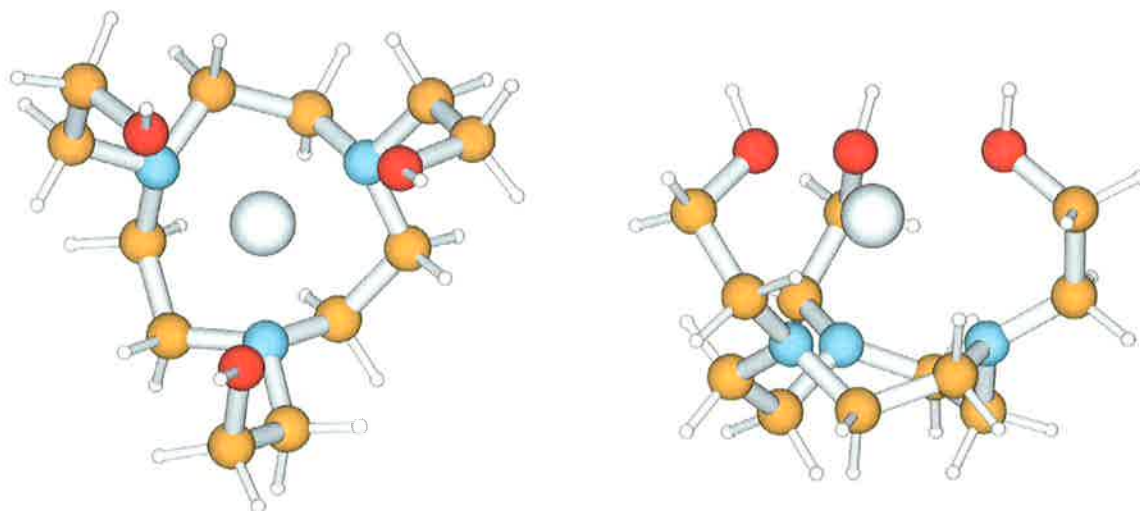
Figure 2.6 A view down and perpendicular to the C_3 axis of the Gaussian 94 LANL2DZ geometry optimised structure of [Na(thec9)]$^+$ on the left and right of the diagram, respectively.
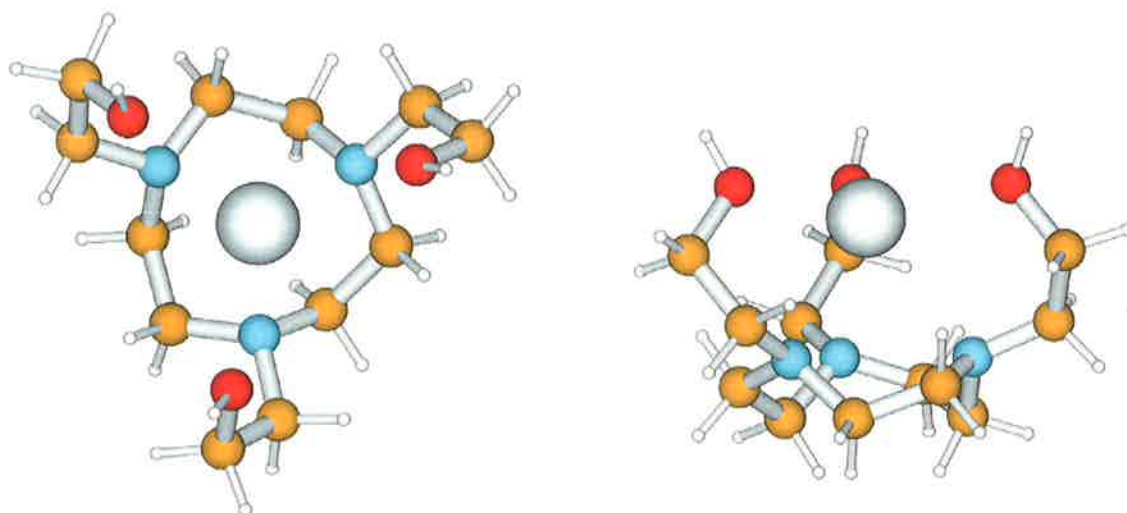
Figure 2.7 A view down and perpendicular to the C_3 axis of the Gaussian 94 LANL2DZ geometry optimised structure of $[K(thec9)]^+$ on the left and right of the diagram, respectively.
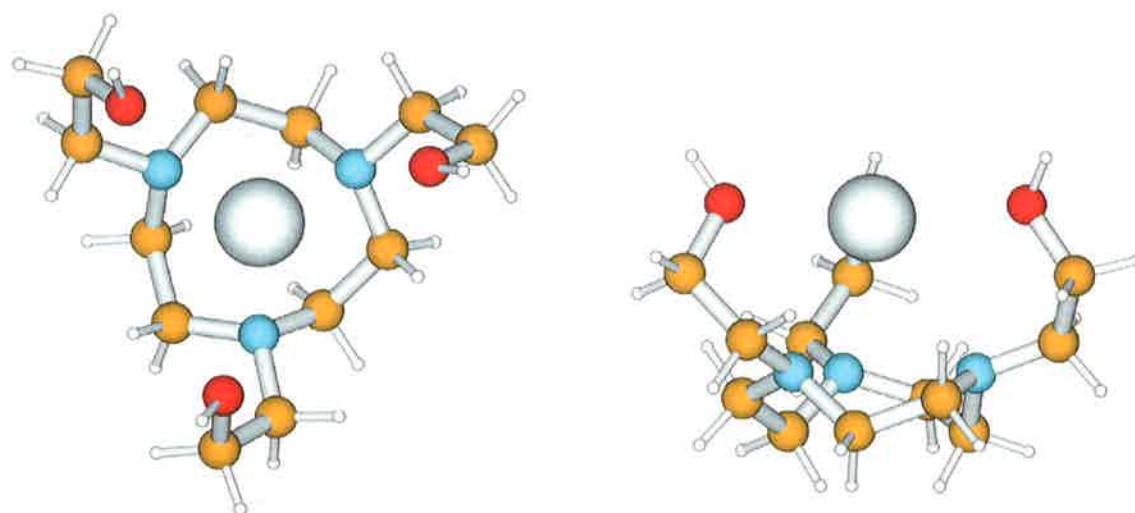
Figure 2.8 A view down and perpendicular to the C_3 axis of the Gaussian 94 LANL2DZ geometry optimised structure of $[Rb(thec9)]^+$ on the left and right of the diagram, respectively.
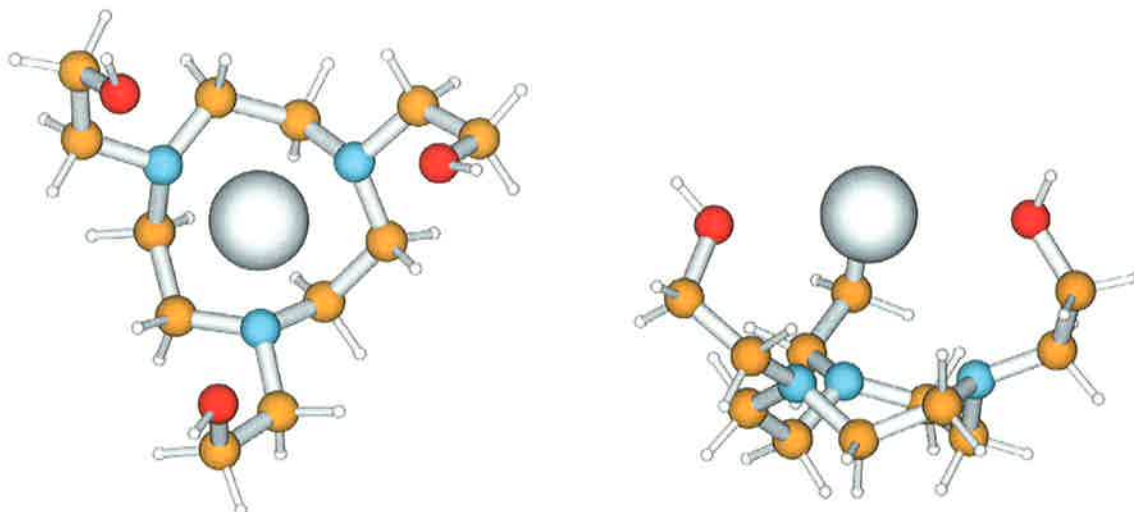
Figure 2.9 A view down and perpendicular to the C_3 axis of the Gaussian 94 LANL2DZ geometry optimised structure of $[Cs(thec9)]^+$ on the left and right of the diagram, respectively.

Table 2.1 Geometry of thec9 and its alkali metal complexes calculated from the LANL2DZ geometry optimised structures. [‡]

Metal Ion M(I)	Crystal Ionic Radii of M(I) (Å)	O-O (Å)	N-N (Å)	$O_{plane} - N_{plane}$ (Å)	$M-O_{plane}$ (Å)	$M-N_{plane}$ (Å)	Twist Angle (f) (°)
-		4.70	3.11	2.65	-	-	±38.0
Li(I)	0.76	2.98	2.94	2.72	1.17	1.56	±15.0
Na(I)	1.02	3.48	3.04	2.86	0.97	1.89	±9.2
K(I)	1.38	4.60	3.10	2.84	0.54	2.31	±11.1
Rb(I)	1.52	5.01	3.13	2.79	0.02	2.56	±11.7
Cs(I)	1.67	5.38	3.16	2.71	-0.12	2.83	±13.4

[‡] Total energies of the LANL2DZ geometry optimised structures are −2249.786, −2269.333, −2250.253, −2322.787, −2301.098 and −2301.098 kJ mol^{-1} for thec9, $[Li(thec9)]^+$, $[Na(thec9)]^+$, $[K(thec9)]^+$, $[Rb(thec9)]^+$ and $[Cs(thec9)]^+$, respectively.

The graphical representations in Figures 2.5 through to 2.9 along with the values shown in Table 2.1 show the conformational trend with increasing radii of the complexed metal ion. The main factors governing this conformational trend include the electrostatic and size requirements of the metal ion and the ability of the ligand to assume an optimum coordination for the metal ion.

As the ionic radius of the metal ion is increased, the metal ion is situated further and further out of the macrocyclic ligand cavity, away from the nitrogen plane and closer to the oxygen plane. In the case of caesium(I), the metal ion is situated 0.12 Å to the outside of the oxygen plane.

Oxygen, due to its relatively high electronegativity, is considered a harder Lewis base than nitrogen. On the basis of this, one would expect the metal to nitrogen plane distance to decrease down the group, as the larger softer group (I) metal ions have an increased affinity for the nitrogen donor atoms. The fact that the opposite occurs is reflective of the inability of the ligand to encapsulate the larger metal ions. This is consistent with the ligand cavity being a more ideal size match for the smaller lithium and sodium (I) ions.

Also shown in Table 2.1 are the twist angles, f, of the structure delineated by the parallel triangular planes of the three oxygen atoms and the three nitrogen atoms when viewed down the C_3 axis, where $f = 0°$ for trigonal prismatic stereochemistry (Figure 2.10). A positive value for the twist angle indicates a Δ (right hand) twist and a negative sign indicates a Λ (left hand) twist.

Apart from the lithium(I) complex, the twist angles, f, were found to increase with increasing ionic radii as the pendant arms expand outwards to accommodate the larger metal ions. The increasing oxygen to oxygen and nitrogen to nitrogen distance is also indicative of the expansion of the ligand cavity.
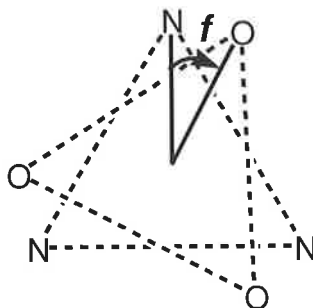
Figure 2.10 The twist angle, *f*, is delineated by the parallel triangular planes of the three oxygen atoms and the three nitrogen atoms when viewed down the C_3 axis, where *f* = 0° for trigonal prismatic stereochemistry.

When compared with the nitrogen plane to oxygen plane distance, the more contracted the ligand cavity becomes (a smaller nitrogen to oxygen plane distance) the greater the twist angle becomes. This could be due to the electrostatic repulsion of the oxygen and nitrogen donor electrons causing the trigonal prism to arrange itself in a more 'staggered' fashion the closer the donor planes become. Alternatively, this increase in twist angle may be a consequence of the inherent strain associated with the coordination of metal ions that are too large for the ligand cavity.

In general, similar trends are observed with the alkali metal complexes of *S*-thpc9, *S*-thpec9 and *S*-thppc9 discussed in this chapter. This was anticipated as they each have a similar ligand cavity.

2.4 Geometry optimisation calculations for 1,4,7-tris((*S*)-2-hydroxy propyl)-1,4,7-triazacyclononane (*S*-thpc9) and its alkali metal complexes

It was anticipated that the addition of (2*S*)-hydroxy propyl pendant arms would result in a right or left handed chirality over the secondary structure of the molecule due to the steric requirements of the CH_3 group attached to the chiral carbon.

In contrast with thec9, the chiral pendant arms result in the Λ and Δ isomers of *S*-thpc9 possessing a diastereomeric relationship rather than the enantiomeric relationship of the Λ and Δ isomers of thec9. This results in either one of the Λ or Δ conformations to be thermodynamically favourable over the other and consequently, geometry optimisation calculations of *S*-thpc9 should result in only one global minimum.

2.4.1 The Λ and Δ diastereomers of *S*-thpc9 and [Na(*S*-thpc9)]⁺

The geometry optimisation calculations were commenced from two starting geometries, one including a clockwise 'up-down' macrocyclic carbon conformation (similar to that of the optimised Δ-thec9 structure) and the other including the clockwise 'down-up' macrocyclic carbon conformation (similar to that of the Λ thec9 conformation). Both calculations imparted optimised structures with macrocyclic conformations corresponding to the macrocyclic conformation of the starting geometry (Figure 2.11).

The Δ conformation of *S*-thpc9, corresponding to a 'down-up' clockwise macrocyclic carbon conformation, was found to be 20 kJ mol⁻¹ lower in energy that of the Λ conformation. Consequently, this optimised structure has been assigned as the global minimum.

Λ

-2556872 kJ mol⁻¹

Δ

-2556892 kJ mol⁻¹

Figure 2.11 A view down the C_3 axes of LANL2DZ geometry optimised structures of the Λ ('up-down' ring carbon configuration) (local minimum) and Δ ('down-up' ring carbon conformation) (global minimum) diastereomers of S-thpc9.

Λ

-2557 314 kJmol⁻¹

Λ

-2557,363 kJmol⁻¹

Figure 2.11 A view down the C_3 axes of the LANL2DZ geometry optimised structures of the Λ ('up-down' ring carbon configuration) (local minimum) and the Λ ('down-up' ring carbon configuration) (global minimum) diastereomers of [Na(S-thpc9)]⁺.

As for the free ligand, the 'down-up' ring carbon configuration of the sodium(I) complex was found to be the globally minimised structure (Figure 2.11). However, the electrostatic attraction of the sodium atom results in the oxygen donors lying closer to the metal ion were found to lie to the left of the nitrogen donors, forming the Λ conformation as opposed to the Δ conformation of the free ligand. This was also found to be the case for the rest of the group(I) metal complexes.

2.4.2 Geometry optimisation calculations of the alkali metal complexes of *S*-thpec9

The globally minimised structures found for the *S*-thpc9 complexes of lithium(I) through to rubidium(I) are shown in Figures 2.12-2.16. Each has incorporated a 'down-up' macrocyclic carbon conformation clockwise around the ring and the oxygen donor atoms lie to the left of the nitrogen donor atoms forming the Λ conformation.
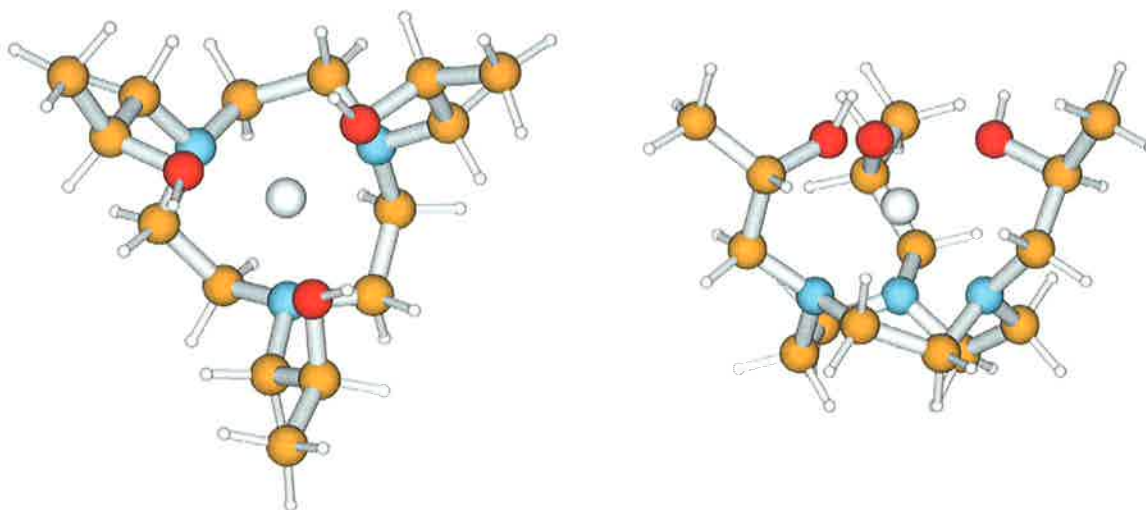
Figure 2.12 A view down and perpendicular to the C_3 axis of the Gaussian 94 LANL2DZ geometry optimised structure of [Li(*S*-thpc9)]$^+$ to the left and right of the diagram, respectively.
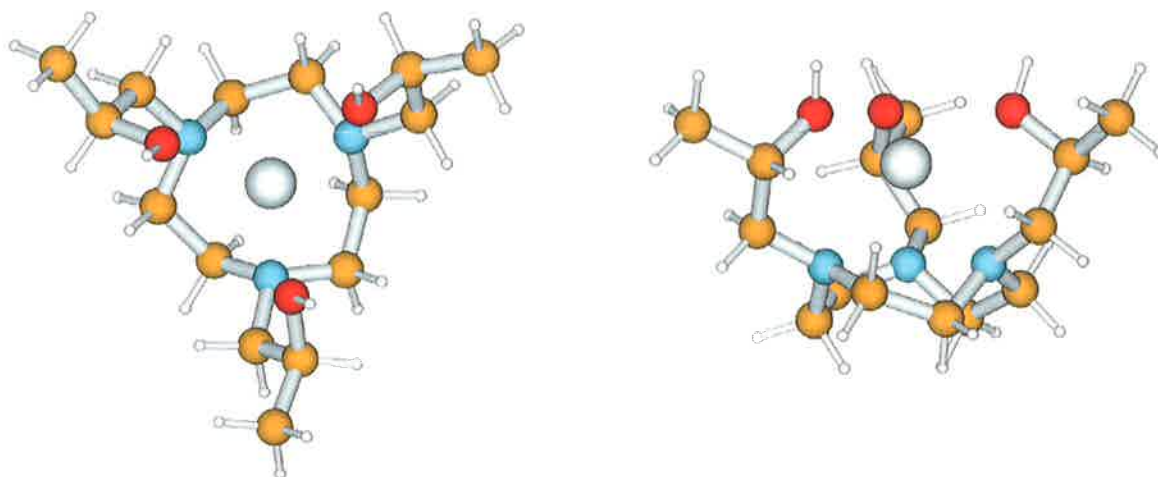
Figure 2.13 A view down and perpendicular to the C_3 axis of the Gaussian 94 LANL2DZ geometry optimised structure of [Na(S-thpc9)]$^+$ to the left and right of the diagram, respectively.

Figure 2.14 A view down and perpendicular to the C_3 axis of the Gaussian 94 LANL2DZ geometry optimised structure of [K(S-thpc9)]$^+$ to the left and the right of the diagram, respectively.

Figure 2.15 A view down and perpendicular to the C_3 axis of the Gaussian 94 LANL2DZ geometry optimised structure of [Rb(S-thpc9)]$^+$ to the left and the right of the diagram, respectively.

Figure 2.16 A view down and perpendicular to the C_3 axis of the Gaussian 94 LANL2DZ geometry optimised structure of [Cs(S-thpc9)]$^+$ to the left and the right of the diagram respectively.

Table 2.2 Geometry of *S*-thpc9 and its alkali metal complexes calculated from the LANL2DZ geometry optimised structures.[‡]

Metal Ion M(I)	Crystal Ionic Radii of M(I) (Å)	O-O (Å)	N-N (Å)	$O_{plane} - N_{plane}$ (Å)	$M\text{-}O_{plane}$ (Å)	$M\text{-}N_{plane}$ (Å)	Twist Angle (f) (°)
-		3.11	4.82	2.57	-	-	39.2
Li(I)	0.76	2.97	2.94	2.71	1.17	1.55	-14.2
Na(I)	1.02	3.72	3.03	2.83	0.95	1.88	-9.9
K(I)	1.38	4.59	3.10	2.82	0.53	2.29	-9.5
Rb(I)	1.52	5.01	4.13	2.74	0.20	2.54	-12.3
Cs(I)	1.67	5.37	3.16	2.67	-0.15	2.82	-13.9

The graphical representations in Figures 2.11 through to 2.16, along with the values in Table 2.2, show the conformational trend with increasing radii of the complexed metal ion. As with thec9, the main factors governing this conformational trend include the electrostatic and size requirements of the metal ion and the ability of the ligand to assume an optimum coordination for the metal ion. The ligand cavity dimensions are almost identical to that of thec9 and similar trends are observed.

[‡] Total energies of the LANL2DZ geometry optimised structures are –2556.891, -2576.476, -2557.363, -2629.893, -2618.656 and –2608.202 kJ mol^{-1} for S-thpc9, [Li(*S*-thpc9)]$^+$, [Na(*S*-thpc9)]$^+$, [K(*S*-thpc9)]$^+$, [Rb(*S*-thpc9)]$^+$ and [Cs(*S*-thpc9)]$^+$, respectively.

2.5 Geometry optimisation calculations for 1,4,7-tris((*S*)-2-hydroxy-2-phenylethyl)-1,4,7-triazacyclononane (*S*-thpec9) and its alkali metal complexes

It was anticipated that the addition of (2*S*)-hydroxyphenylethyl pendant arms to tacn would result also in a right or left handed chirality over the secondary structure of the ligand. Due to the increased size of the pendant arm phenyl substituent of *S*-thpec9 when compared with the methyl group of *S*-thpc9, it was also anticipated that they might have more of an influence on the ligand cavity dimensions.

2.5.1 The Λ and Δ diastereomers of *S*-thpec9 and [Na(*S*-thpec9)]⁺

As with *S*-thpc9, the geometry optimisation calculations were commenced from two starting geometries, each incorporating one of the macrocyclic conformations. One including a clockwise 'up-down' macrocyclic carbon conformation (similar to that of the optimised Δ-thec9 structure) and the other including the clockwise 'down-up' macrocyclic carbon conformation (similar to that of the Λ thec9 conformation). Again, both calculations imparted optimised structures with macrocyclic conformations corresponding to the macrocyclic conformation of the starting geometry (Figure 2.17).

For *S*-thpec9 the Δ conformation, corresponding to a 'down-up' clockwise macrocyclic carbon conformation was found to be 100 kJ mol⁻¹ lower in energy than the Λ conformation. Consequently, this optimised structure has been assigned as the global minimum (Figure 2.17).
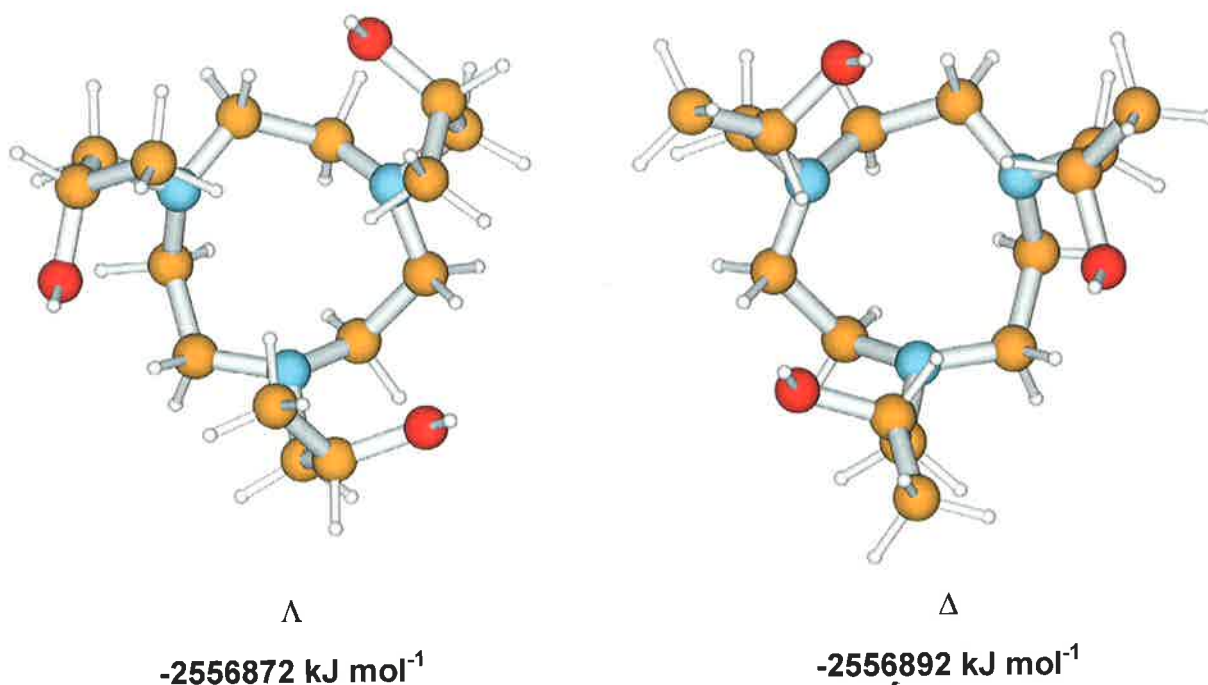
As for the *S*-thpec9, the 'down-up' ring carbon configuration of the sodium(I) complex was found to be the globally minimised structure. However, electrostatic attraction has resulted in the oxygen atoms being pulled in closer to the metal ion. They lie to the left of the nitrogen atoms, forming the Λ conformation as opposed to the Δ conformation of the free ligand. This was also found to be the case for the rest of the group(I) metal complexes (Figure 2.18).

Λ

-4055526 kJ mol^{-1}

Δ

-4055626 kJ mol^{-1}
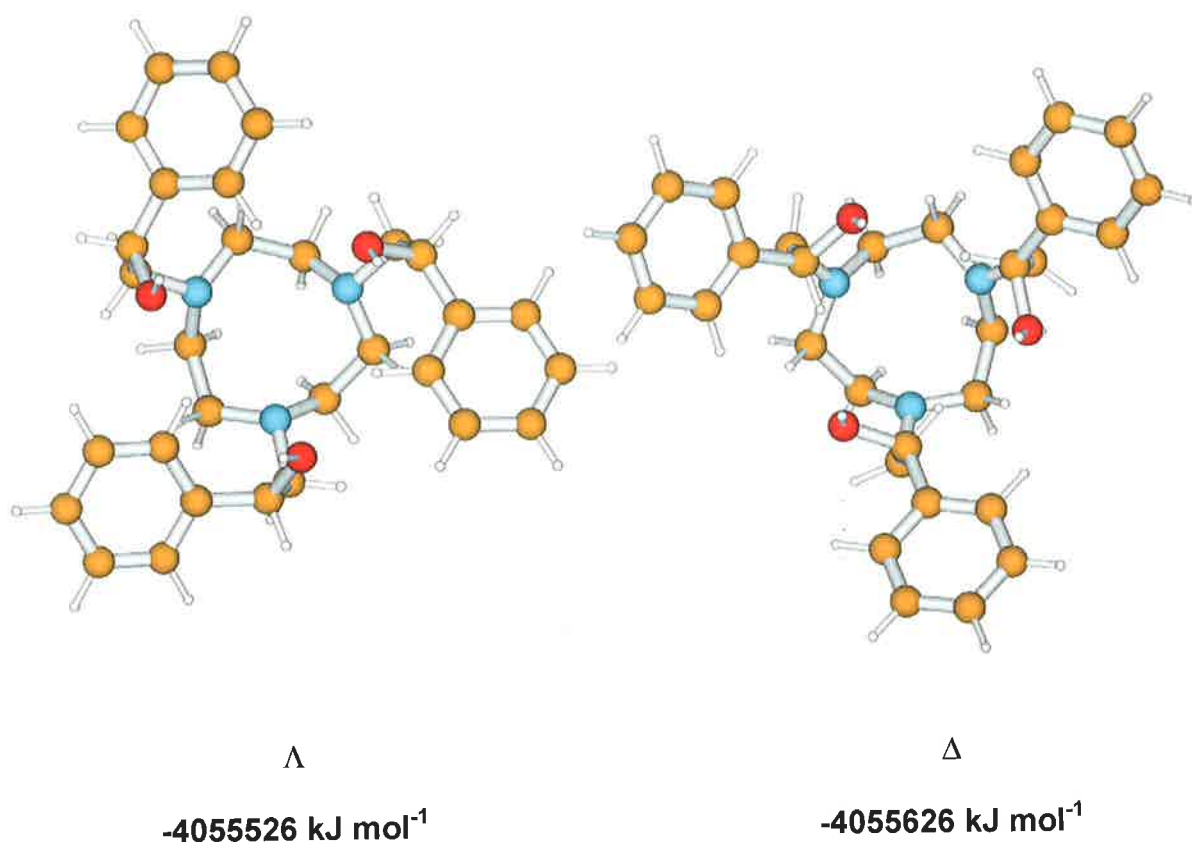
Figure 2.17 A view down the C_3 axes of the Gaussian 94 LANL2DZ geometry optimised structures of the Λ ('up-down' ring carbon configuration) (local minimum) and Δ ('down-up' ring carbon conformation) (global minimum) diastereomers of *S*-thpec9.
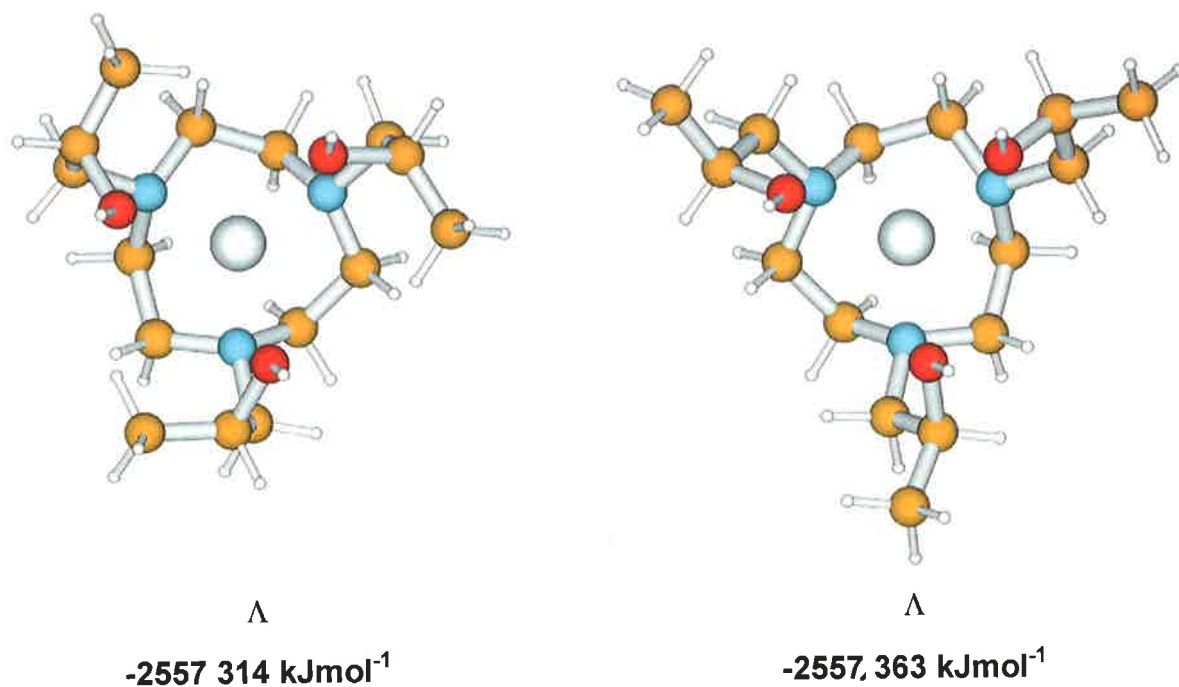
Λ

-4056028 kJ mol^{-1}

Λ

-4056081 kJ mol^{-1}
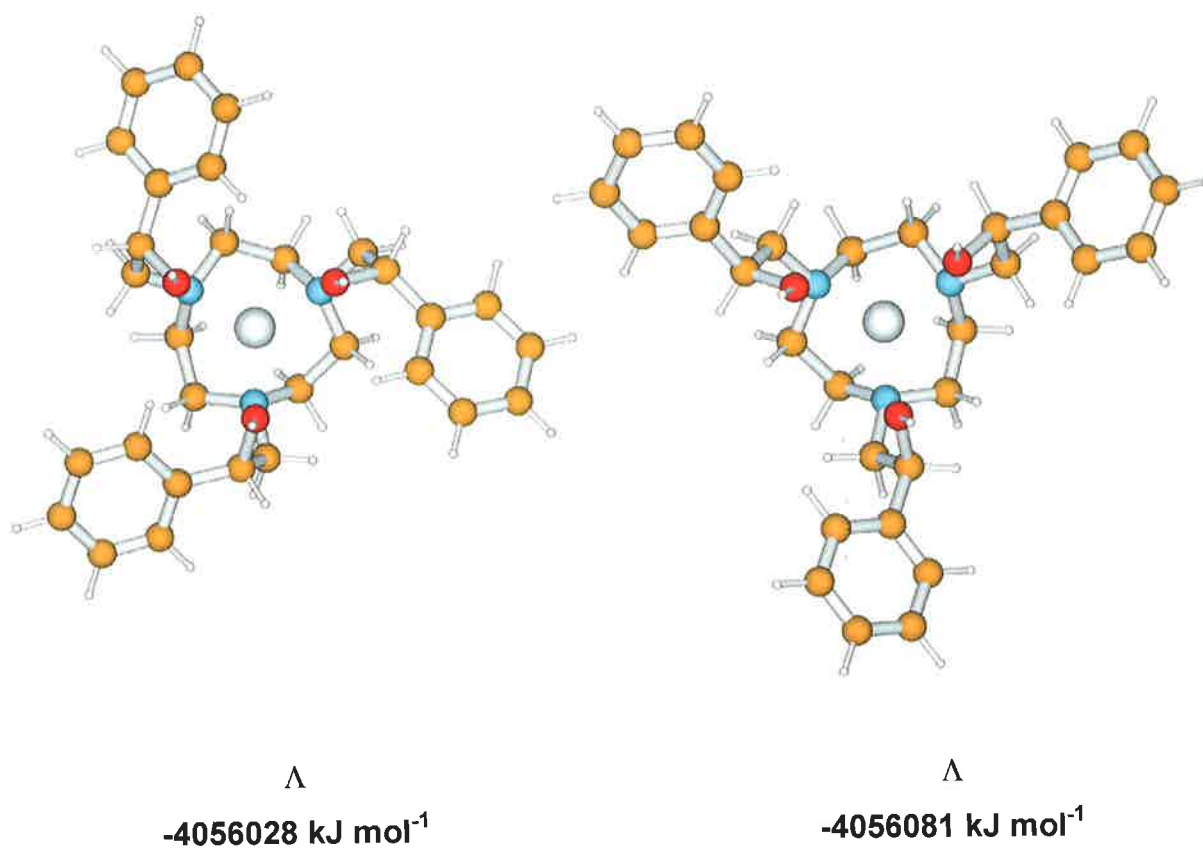
Figure 2.18 A view down the C_3 axes of the Gaussian 94 LANL2DZ geometry optimised structures of the Λ ('up-down' ring carbon configuration) (local minimum) and the Λ ('down-up' ring carbon configuration) (global minimum) diastereomers of [Na(S-thpec9)]$^+$.

2.4.2 Geometry optimisation calculations of the alkali metal complexes of *S*-thpec9

Figure 2.19 A view down and perpendicular to the C_3 axis of the Gaussian 94 LANL2DZ geometry optimised structure of $[Li(S\text{-}thpec9)]^+$ on the left and right of the diagram, respectively.
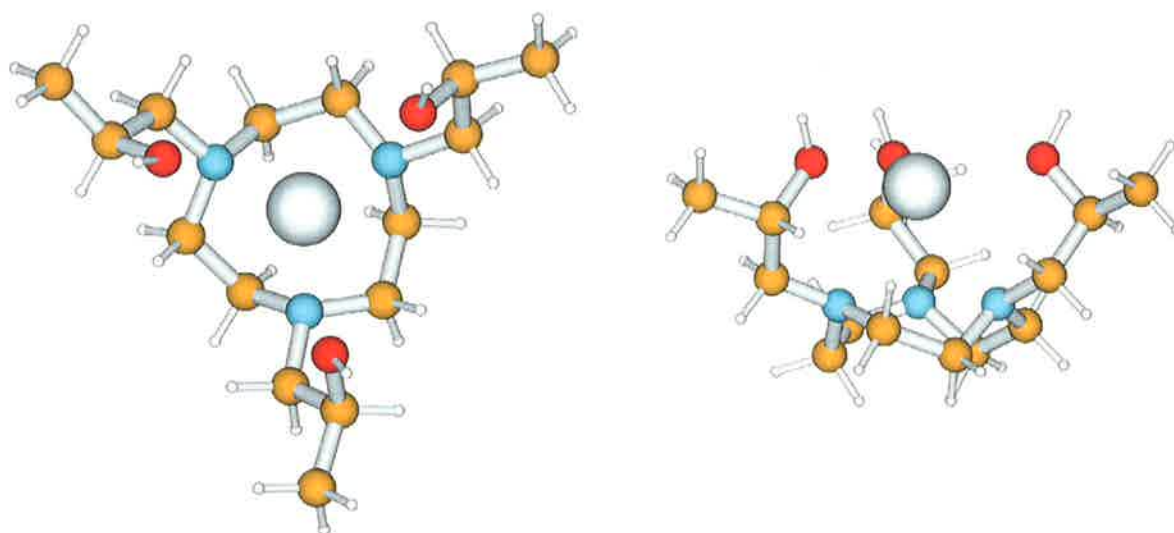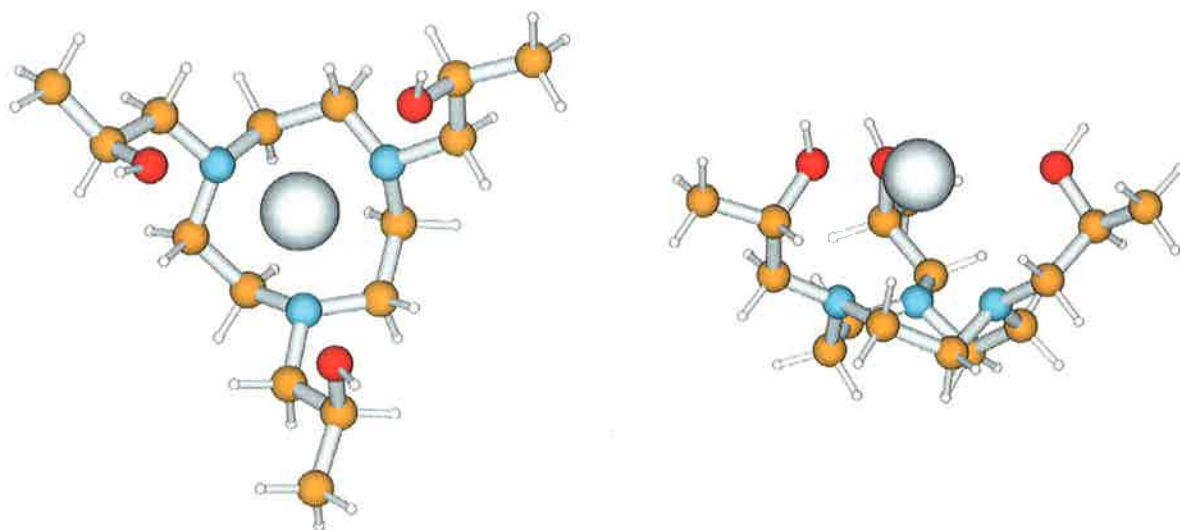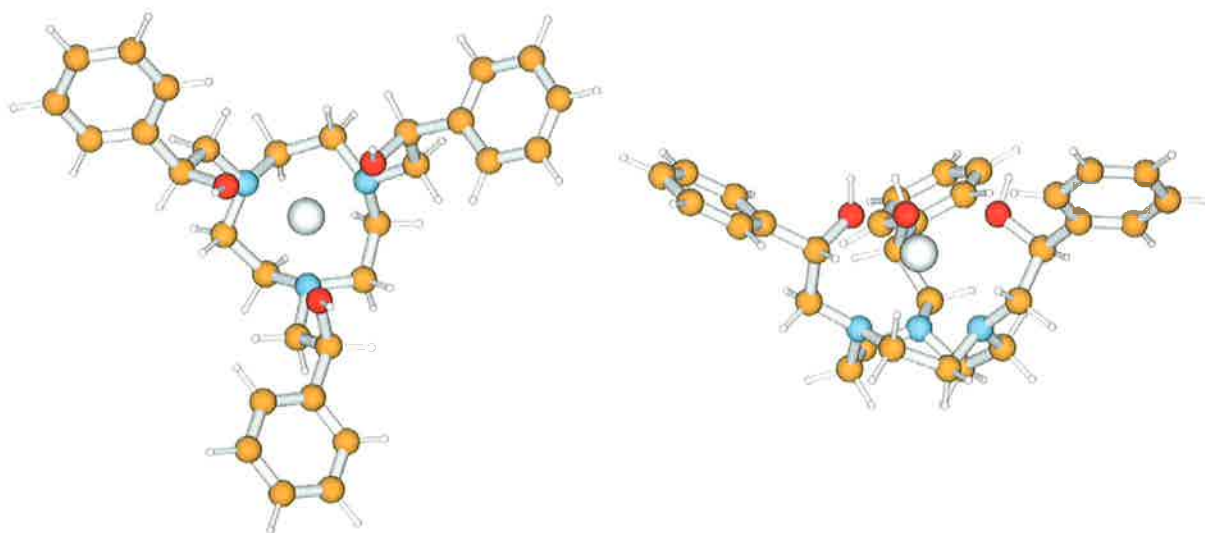

Figure 2.20 A view down and perpendicular to the C_3 axis of the Gaussian 94 LANL2DZ geometry optimised structure of $[Na(S\text{-}thpec9)]^+$ on the left and right of the diagram, respectively.
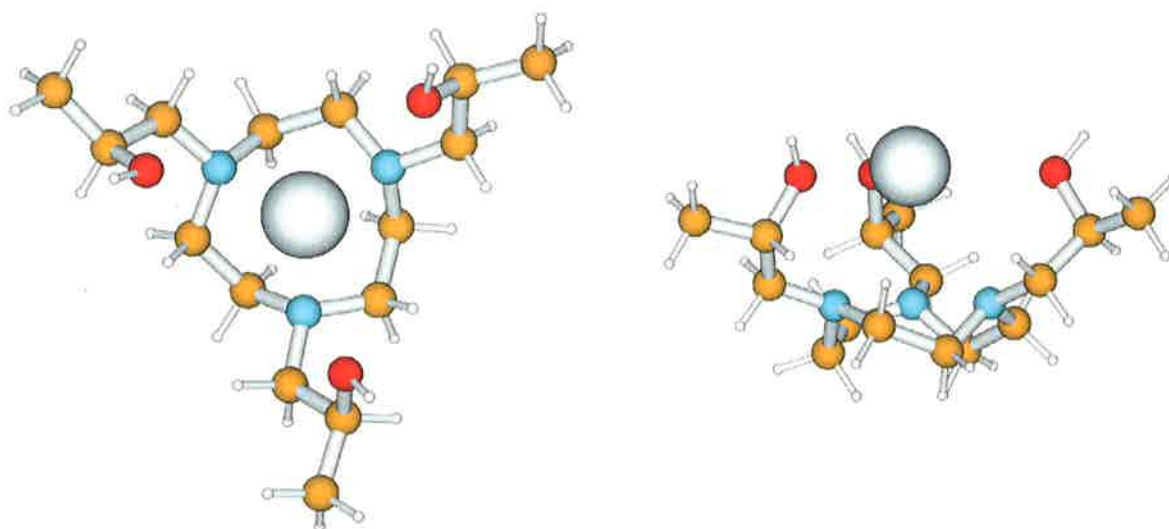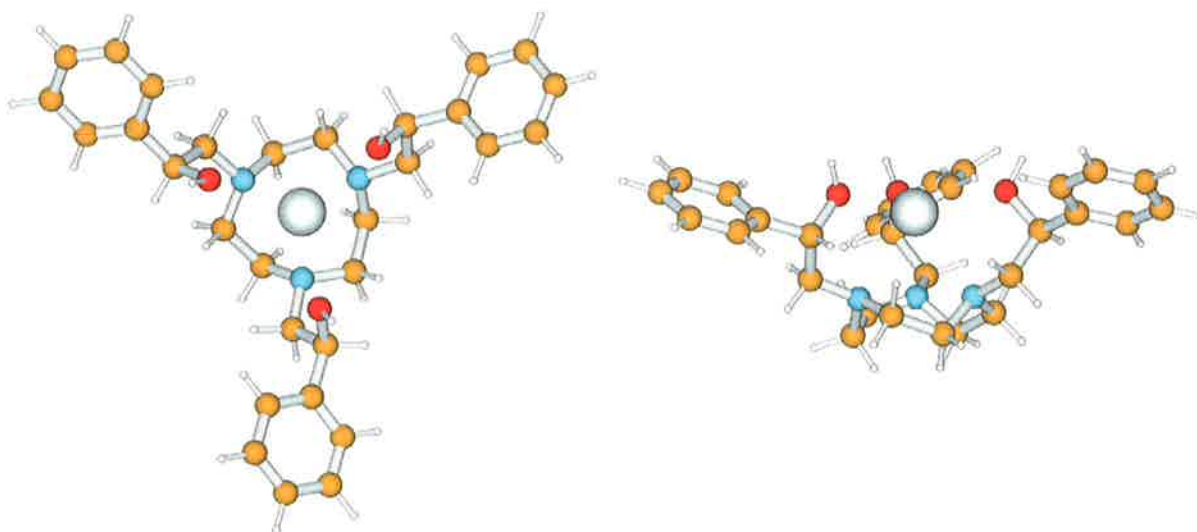
Figure 2.21 A view down and perpendicular to the C_3 axis of the Gaussian 94 LANL2DZ geometry optimised structure of [K(S-thpec9)]$^+$ on the left and right of the diagram, respectively.

Figure 2.22 A view down and perpendicular to the C_3 axis of the Gaussian 94 LANL2DZ geometry optimised structure of [Rb(S-thpec9)]$^+$ on the left and right of the diagram, respectively.

Figure 2.23 A view down and perpendicular to the C_3 axis of the Gaussian 94 LANL2DZ geometry optimised structure of $[Cs(S\text{-}thpec9)]^+$ on the left and right of the diagram, respectively.

Table 2.3 Geometry of S-thpec9 and its alkali metal complexes calculated from the LANL2DZ geometry optimised structures.[‡]

Metal Ion M(I)	Crystal Ionic Radii of M(I) (Å)	O-O (Å)	N-N (Å)	$O_{plane} - N_{plane}$ (Å)	$M\text{-}O_{plane}$ (Å)	$M\text{-}N_{plane}$ (Å)	Twist Angle (*f*) (°)
–	–	4.41	3.10	2.80	–	–	34.0
Li(I)	0.76	3.02	2.94	2.72	1.15	1.57	-13.7
Na(I)	1.02	3.71	3.03	2.84	0.96	1.88	-7.9
K(I)	1.38	4.60	3.11	2.81	0.52	2.29	-9.1
Rb(I)	1.52	5.02	3.14	2.76	0.21	2.55	-10.5
Cs(I)	1.67	5.37	3.15	2.67	-0.16	2.83	-25.9

[‡] Total energies of the LANL2DZ geometry optimised structures are –4055.626, –4075.190, -4056.081, -4128.611, -4117.410 and –4106.937 kJ mol^{-1} for S-thpec9, $[Li(S\text{-}thpec9)]^+$, $[Na(S\text{-}thpec9)]^+$, $[K(S\text{-}thpec9)]^+$, $[Rb(S\text{-}thpec9)]^+$ and $[Cs(S\text{-}thpec9)]^+$, respectively.

The graphical representations in Figures 2.19 through to 2.23 along with the values shown in Table 2.3 show the conformational trend with increasing radii of the complexed metal ion. Again the dimensions of the ligand cavity and trends are similar to those of thec9 and *S*-thpc9 despite the large pendant arm phenyl substituent.

The potential receptor cavity formed by the pendant arm phenyl substituents is a 'saucer-like' shape that becomes less concave with the increasing size of the metal ion. This implies that the choice a metal ion with appropriate size requirements can alter the shape of the cavity to form a compatible receptor for a chosen guest molecule.

2.6 Geometry optimisation calculations for 1,4,7-tris((2*S*)-hydroxy-3-phenylpropyl)-1,4,7-triazacyclononane (*S*-thppc9) and its alkali metal complexes

It was anticipated that the addition of a -CH$_2$- group in between the chiral pendant arm carbons to give *S*-thppc9, that the phenyl groups might result in a deeper more 'basket-like' cavity, rather than the 'saucer-like' cavity of *S*-thpec9 due to the free rotation about its σ bonds.

Again, a single global minimum was expected for both the free ligand and its metal complexes due to the chiral nature of the pendant arms.

2.6.1 The Λ and Δ diastereomers of *S*-thppc9

As for *S*-thpc9 and *S*-thpec9, the geometry optimisation calculations were again commenced from two starting geometries, each incorporating one of the macrocyclic conformations. One including a clockwise 'up-down' macrocyclic carbon conformation and the other including a clockwise 'down-up' carbon configuration. Both calculations imparted optimised structures with macrocyclic conformations corresponding to the macrocyclic conformation of the starting geometry. In contrast to the global minima for *S*-thpc9 and *S*-thpec9, and the Δ conformation, corresponding to a 'up-down' clockwise macrocyclic carbon conformation for *S*-thppc9, was found to be 107 kJ mol^{-1} lower in energy than the Λ conformation found for the opposite macrocyclic conformation. Consequently, this optimised structure has been assigned as the global minimum (Figure 2.24). Similarly the Δ conformation with the 'up-down' clockwise macrocyclic conformation corresponded to the global minimum energy structures for [M(*S*-thppc9)]$^+$ complex where M = Li, Na and K.

As for the free ligand, the 'up-down' ring carbon configuration of the lithium(I) complex also afforded the globally minimised structure, also showing a Δ conformation.
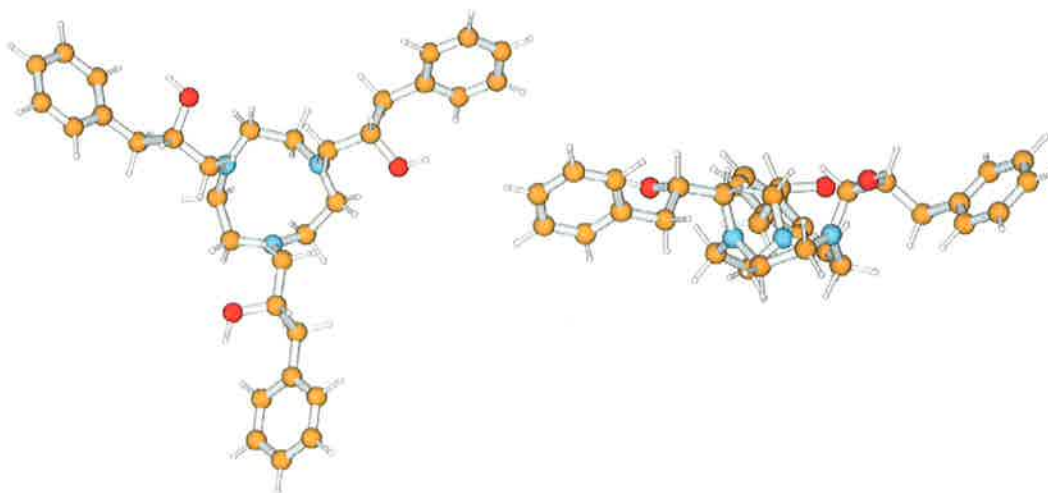
Figure 2.24 A view down and perpendicular to the C_3 axis of the Gaussian 94 LANL2DZ geometry optimised structure of S-thppc9 shown to the left and the right of the diagram, respectively.
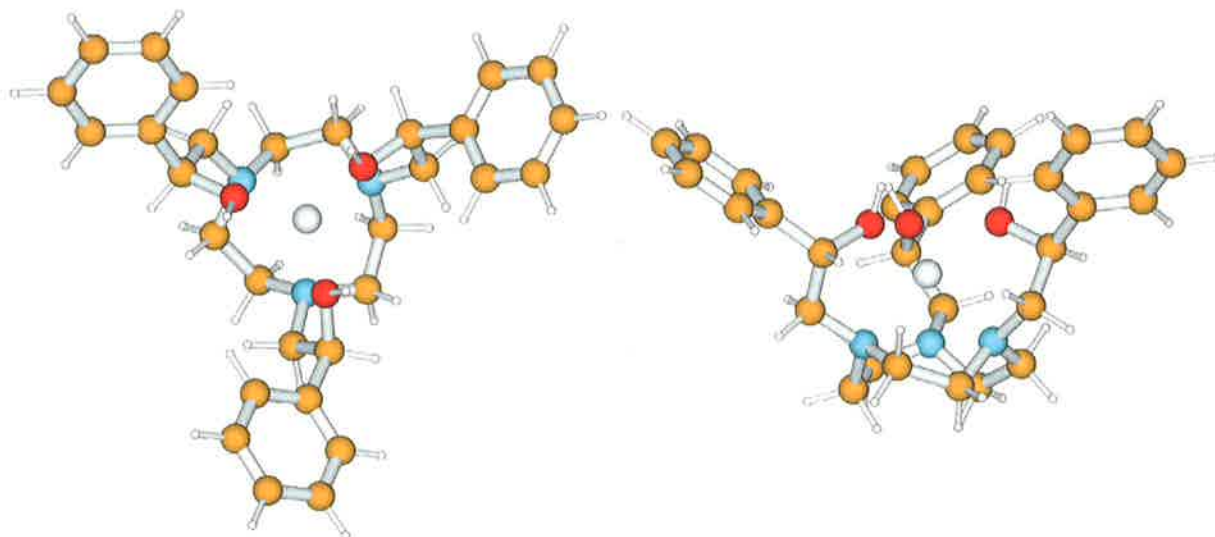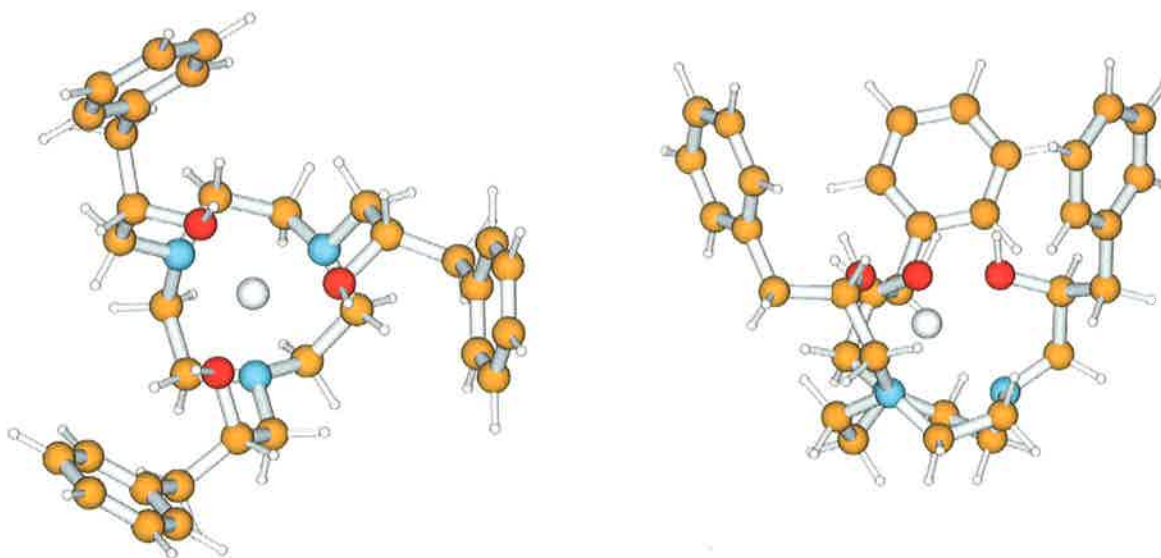

Figure 2.25 A view down and perpendicular to the C_3 axis of the Gaussian 94 LANL2DZ geometry optimised structure of [Li(S-thppc9)]$^+$ on the left and right of the diagram, respectively.

It can be seen from the globally minimised structure of the lithium(I) complex that the phenyl groups are now situated in a more up-right fashion in comparison to the more restricted phenyl groups of S-thpec9, which results in a more basket-like receptor cavity.

Comparison of the globally minimised conformations of $[Zn(S\text{-thpec9})]^{2+}$ and $[Zn(S\text{-thppc9})]^{2+}$ also show the pendant arm phenyl substituents to form a deeper cavity for the latter complex (Figure 2.26).
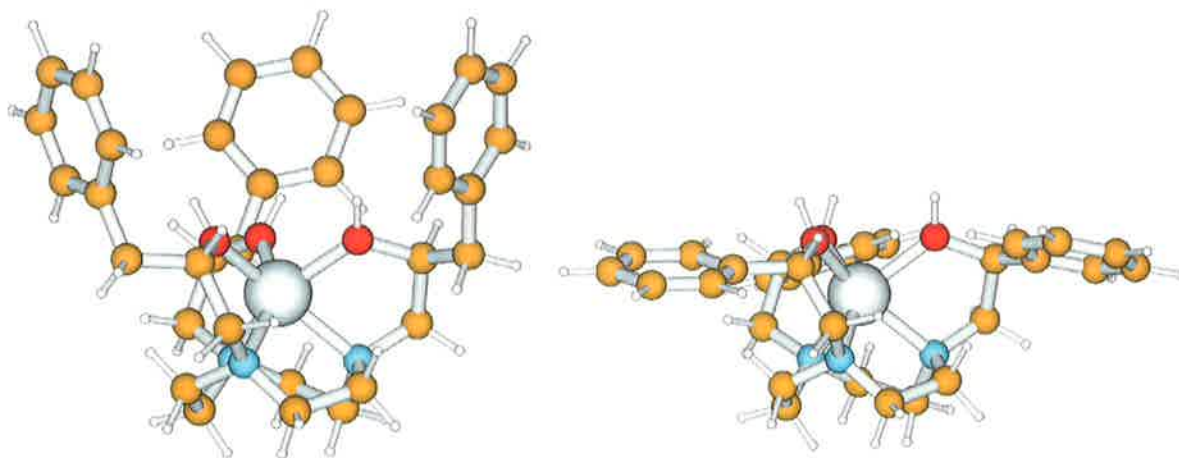
Figure 2.26 A view perpendicular to the C_3 axes of the Gaussian 94 LANL2DZ geometry optimised structures of $[Zn(S\text{-thppc9})]^{2+}$ and $[Zn(S\text{-thpec9})]^{2+}$ on the left and the right of the diagram, respectively.

2.4.2 Geometry Optimisation Calculations of the lithium(I), sodium(I), and potassium(I) complexes of S-thppc9

Due to the increasing impracticability of the use of the LANL2DZ basis set because of its computing time requirements, the following calculations of [M(S-thppc9)]$^+$, where M = Li, Na and K, were performed using the LANL2MB basis set as previously discussed.
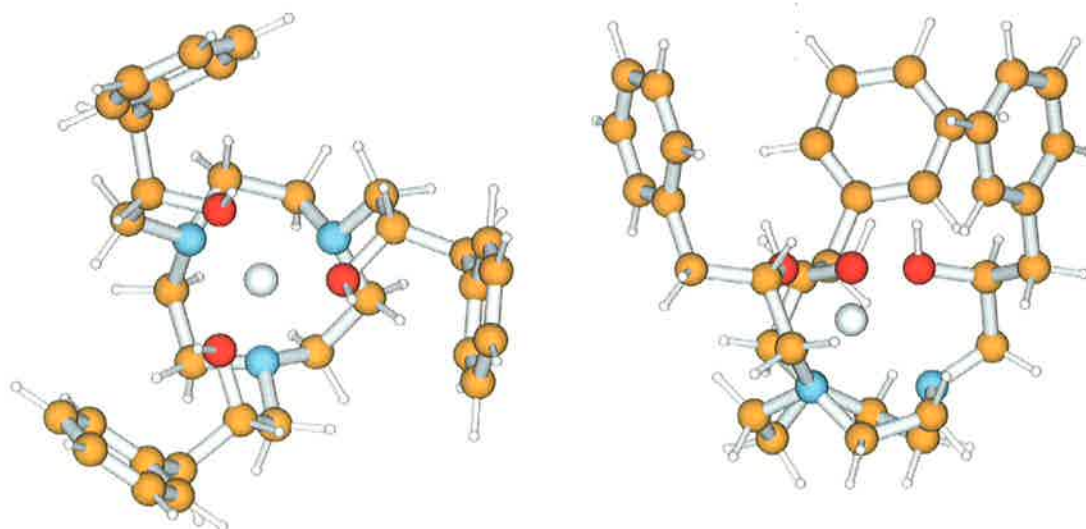
Figure 2.27 A view down and perpendicular to the C_3 axis of the Gaussian 94 LANL2MB geometry optimised structure of [Li(S-thppc9)]$^+$ on the left and right of the diagram, respectively.
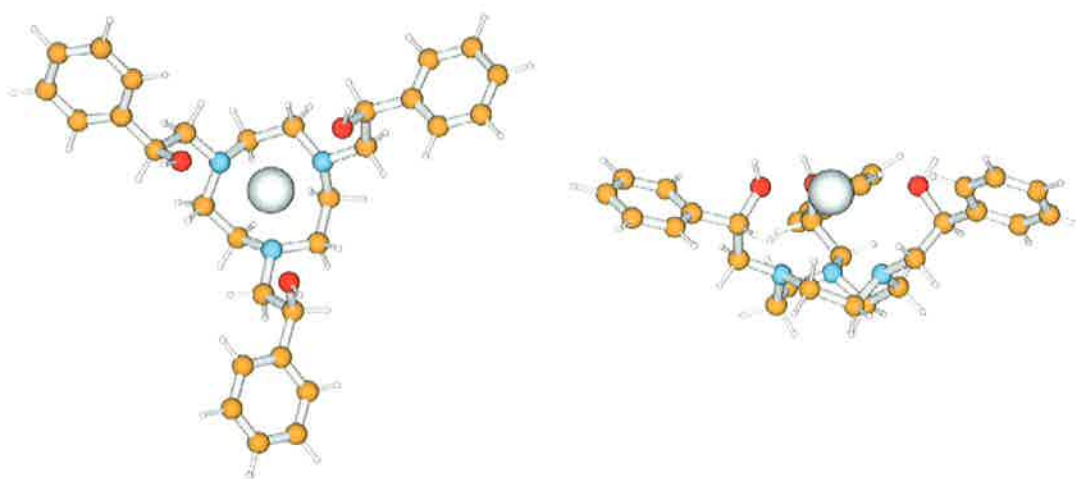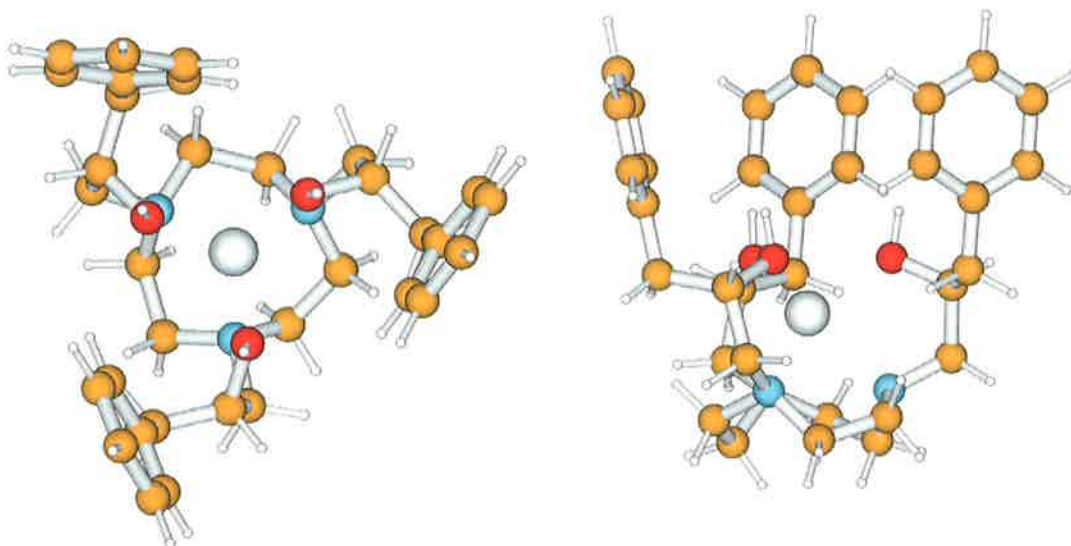
Figure 2.28 A view down and perpendicular to the C_3 axis of the Gaussian 94 LANL2MB geometry optimised structure of [Na(S-thppc9)]$^+$ on the left and right of the diagram, respectively.

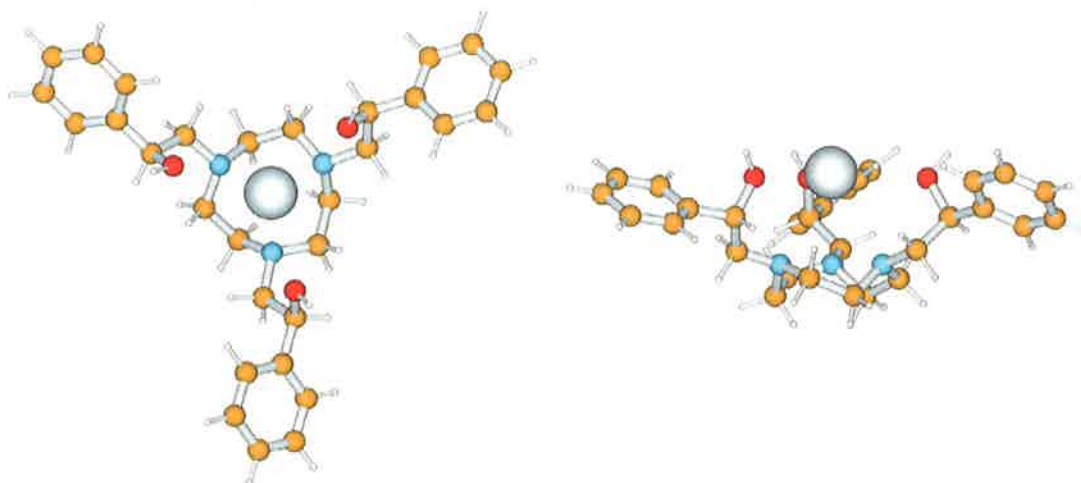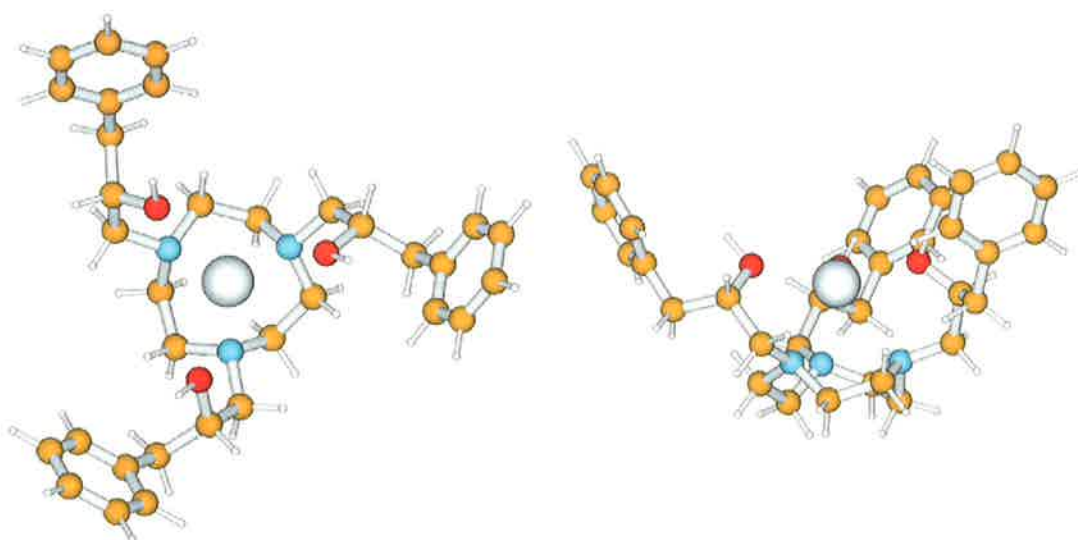**Figure 2.29** A view straight down and perpendicular to the C_3 axis of the Gaussian 94 LANL2MB geometry optimised structure of [K(S-thppc9)]$^+$ on the left and right of the diagram, respectively.

Table 2.3 Geometry of *S*-thppc9 and its alkali metal complexes calculated from the Gaussian 94 LANL2DZ and LANL2MB geometry optimised structures.[‡]

Metal Ion M(I)	Crystal Ionic Radii of M(I) (Å)	O-O (Å)	N-N (Å)	$O_{plane} - N_{plane}$ (Å)	$M-O_{plane}$ (Å)	$M-N_{plane}$ (Å)	Twist Angle (*f*) (°)
_[a]	-	7.27	3.06	1.62	-	-	18.9
Li(I)[a]	0.76	3.05	2.94	2.56	1.05	1.51	25.2
Li(I)[b]	0.76	2.78	2.83	2.41	1.05	1.36	30.4
Na(I)[b]	1.02	3.14	2.93	2.51	0.88	1.63	7.3
K(I)[b]	1.38	4.50	3.05	2.64	0.50	2.14	16.2

[a]LANL2DZ optimised structures

[b]LANL2MB optimised structures

The LANL2MB geometry optimised structure of [Li(*S*-thppc9)]$^+$ results in the ligand cavity to be more contracted when compared with that of the LANL2DZ geometry optimised structure. This is due to the differing treatment of atoms for the two basis sets (outlined in section 2.2.1). For this reason, the geometry optimised structures calculated using differing basis sets can not be directly compared.

The graphical representations in Figures 2.27 through to 2.29 along with the values shown in Table 2.3 show the geometric trends within the LANL2MB geometry optimised structures of [Li(*S*-thppc9)]$^+$, [Na(*S*-thppc9)]$^+$ and [K(*S*-thppc9)]$^+$ to be similar to those observed for the analogous complexes of LANL2DZ optimised structures of thec9, *S*-thpc9 and *S*-thpec9.

[‡] The total energies of the LANL2DZ geometry optimised structures are –4632.697, -4382.228 kJ mol^{-1} for *S*-thppc9 and [Li(*S*-thppc9)]$^+$, respectively. The total energies of the LANL2MB geometry optimised structures are -4330.302, -4311.278 and -4433.553 kJ mol^{-1} for [Li(*S*-thppc9)]$^+$, [Na(*S*-thppc9)]$^+$ and [K(*S*-thppc9)]$^+$, respectively.

It can also be seen that the shape of the receptor cavity of *S*-thppc9 is effected by the size of the metal ion where complexation of the larger metal ions results in a wider and shallower cavity. These results support the possibility of adjusting the shape of the receptor cavity by changing the size of the coordinated metal ion.

2.7 The relative gas-phase Δ energy series of the alkali metal complexes of thec9, *S*-thpc9 and *S*-thpec9

The gas-phase complexation reaction is as in Equation 2.2.

$$M^+ \quad + \quad Ligand \quad \longrightarrow \quad [M(ligand)]^+ \qquad \textbf{2.2}$$

If calculated single point energies of the geometry optimised structures of the free ligand and the free metal ion are subtracted from that of the geometry optimised structure of the complex, the resulting electronic energy difference (ΔE) can be compared with other systems that have been treated in a similar way. The values obtained for ΔE can then be used to form a relative gas-phase stability trend that can give an indication of the structural compatibility of the ligand and metal ion in the absence of solvation effects.

This process was carried out for the alkali metal complexes, lithium(I) to rubidium(I), of thec9, *S*-thpc9 and *S*-thpec9 using the STO-3G** single point energy calculations of the LANL2DZ geometry optimised structures. The resultant trends are graphically displayed in Figure 2.30. As no entropy or thermal corrections have been made in the calculations, ΔE is a purely a measure of the electronic gas phase stabilisation energy of the complex when compared to the free ligand and metal ion. The more negative the value of ΔE, the greater the stabilisation energy involved in the complexation.

The ΔE trend shows each ligand to have the greatest size compatibility with the smallest of the metal ions lithium(I). The inherent strain associated with the complexation of a metal ion that is too large for the cavity is reflected in the lesser electronic stabilisation energy of the larger metal ions.

Energy Series from Optimised Structures
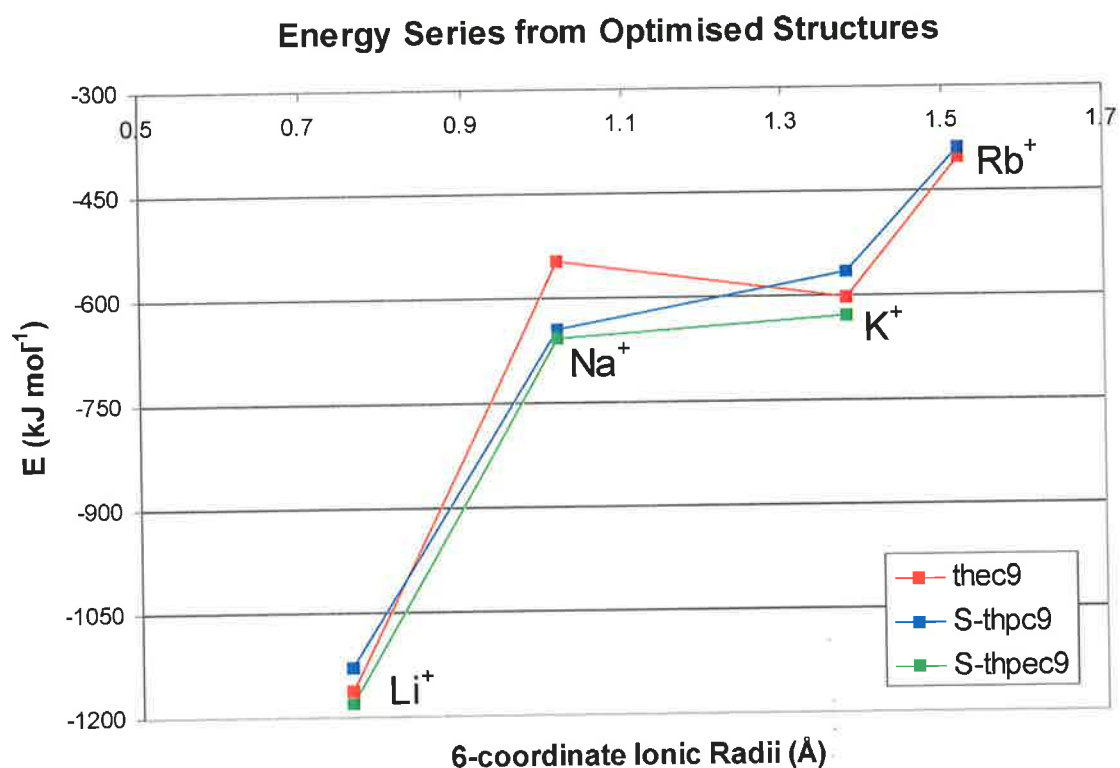
Figure 2.30 Plot of the calculated electronic energy difference (ΔE) between the complexed ligand and metal ($[M(ligand)]^+$) and the free ligand and metal ion against the six-coordinate crystal ionic radii of the alkali metal ions lithium(I) to rubidium. Electronic energies were calculated from STO-3G** single point energy calculations of the LANL2DZ geometry optimised structures using Gaussian 94.

2.8 X-ray crystal structures of [Zn(*S*-thpc9)]1.5ClO$_4$.0.5Cl and *S*-thpec9

2.8.1 X-ray crystal structure of [Zn(*S*-thpc9)]1.5ClO$_4$.0.5Cl[13]

Crystals of [Zn(*S*-thpc9)]1.5ClO$_4$.0.5Cl were grown by slow evaporation of an aqueous solution containing Zn(ClO$_4$)$_2$ and *S*-thpc9. The chloride anion was probably picked up from the demineralised water. The –OH protons were not located in the structure. The [Zn(*S*-thpc9)]$^{2+}$ cation (Figures 2.30 and 2.31) shows a 'down-up' macrocylic carbon configuration clockwise around the ring and was found to assume the Λ configuration.

The gas-phase Gaussian 94 *ab initio* geometry optimised structure also shows 'down-up' macrocyclic carbon configuration clockwise around the ring and also was found to assume the Λ conformation (Figures 2.30 and 2.31). The geometries of the two are shown in Table 2.4. The structural similarities between the two structures are significant, and show that gas-phase geometry optimisation calculations, such as these, can sometimes act as a reasonable guide to the solid-state conformation.

Table 2.4 Geometry of the X-ray crystal structure and the Gaussian 94 *ab initio* LANL2DZ geometry optimised structure of [Zn(*S*-thpc9)]$^{2+}$.[‡]

[Zn(*S*-thpc9)]$^{2+}$	O-O (Å)	N-N (Å)	O$_{plane}$ – N$_{plane}$ (Å)	M-O$_{plane}$ (Å)	M-N$_{plane}$ (Å)	Twist Angle (*f*) (°)
X-ray crystal structure	2.93	2.83	2.73	1.31	1.42	-23.9 −7·3
Gaussian 94 optimised structure	3.05	2.90	2.64	1.19	1.45	-19.1

[‡] The total energy of the LANL2DZ geometry optimised structure of [Zn(S-thpc9)]$^{2+}$ is –2722 833 kJ mol^{-1}.
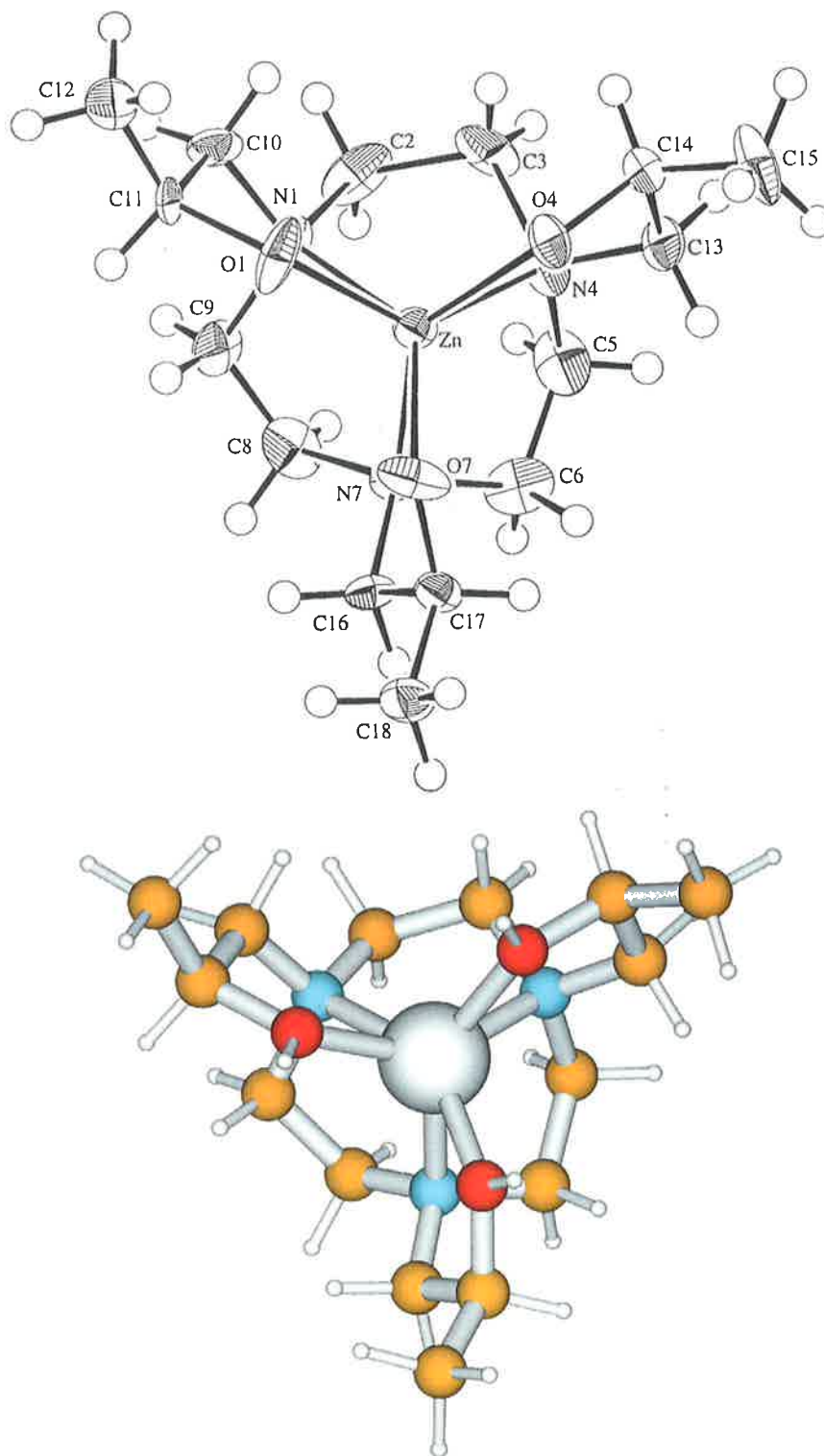
Figure 2.31 A view down the C_3 axis of the X-ray crystal structure[13] (above) and the Gauusian 94 *ab initio* LANL2DZ geometry optimised structure (below) of Λ-[Zn(S-thpc9)]$^{2+}$. Intramolecular bond distances of the X-ray crystal structure are shown in Appendix (i).
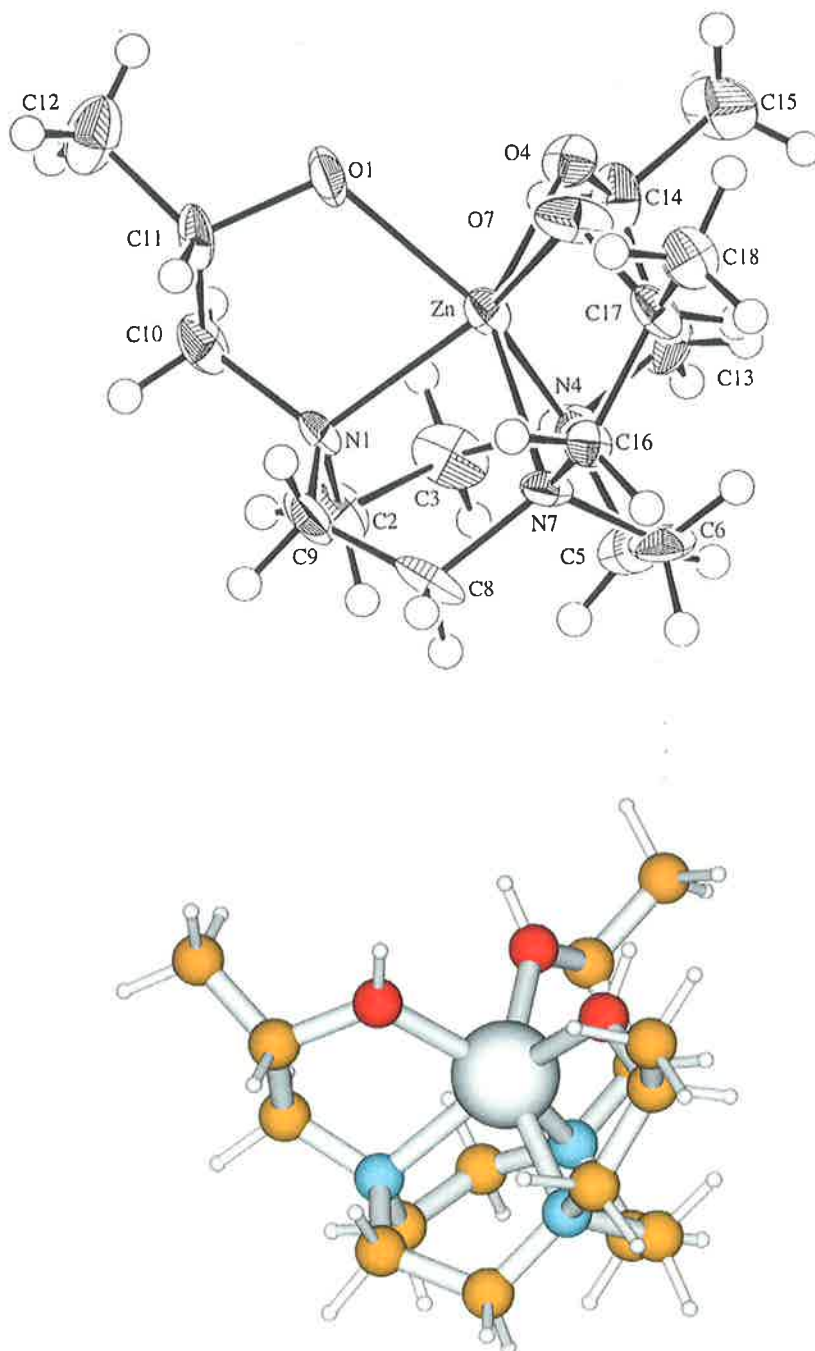
Figure 2.32 Similar views of the X-ray crystal structure[13] (above) and the Gaussian 94 *ab initio* LANL2DZ geometry optimised structure (below) of Λ-[Zn(*S*-thpc9)]$^{2+}$. Intramolecular distances for the X-ray crystal structure are shown in Appendix (i)

2.8.2 X-ray crystal structure of *S*-thpec9

The crystals of *S*-thpec9 were grown by slow evaporation of a dimethylformamide solution. The pendant arms were found to occupy the +++ configuration that is expected for pendant arm triazacyclononane ligands (see p6). The calculated gas-phase structure (p36) possesses a C_3 axis. It appears that in the solid-state the equivalence of the phenyl groups required by a C_3 axis is disrupted by intermolecular interactions in the crystal.
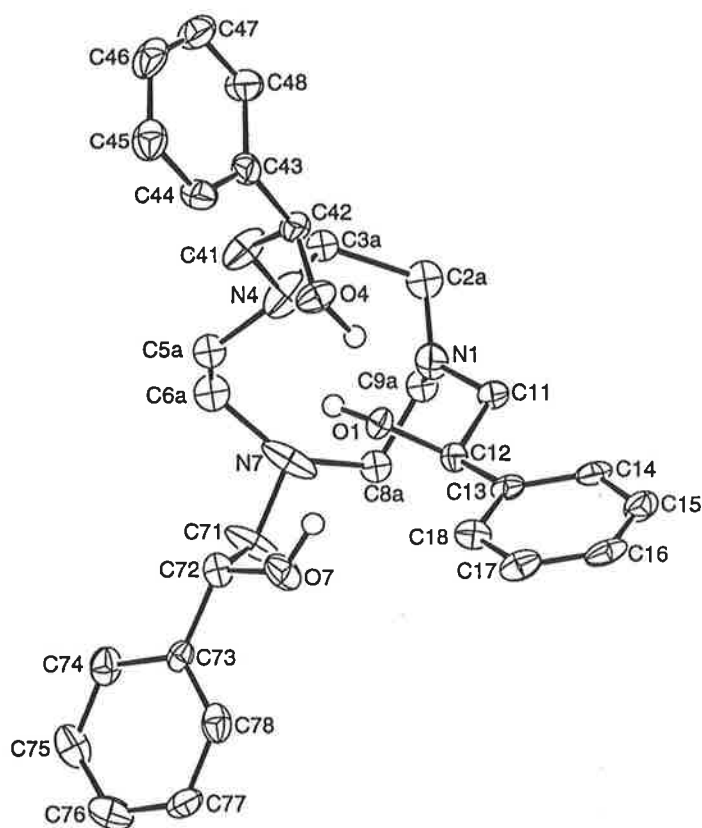
Figure 3.32 A top view of the X-ray crystal structure of *S*-thpec9. Intermolecular distances are shown in Appendix (ii)).[13]
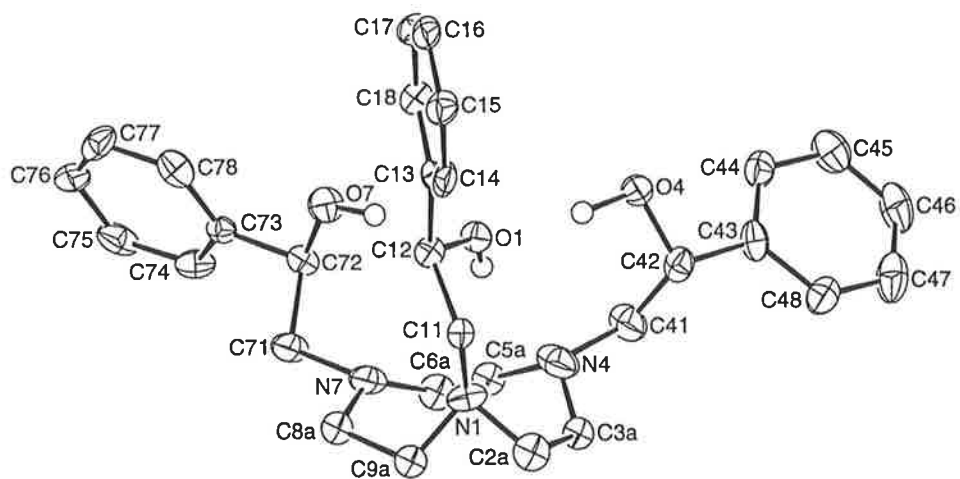
Figure 3.32 A side view of the X-ray crystal structure of *S*-thpec9. Intramolecular distances are shown in Appendix (ii)).[13]

References

1. J. B. Foresman and A. Frisch, *Exploring Chemistry with Electronic Structure Methods.* 2 ed. 1993, Pittsburgh: Gaussian Inc.

2. G. H. Grant and W. G. Richards, *Computational Chemistry.* 1995, Oxford: Oxford University Press.

3. W. J. Hehre, L. Radom, P. R. Schleyer and J. A. Pople, *Ab Initio Molecular Orbital Theory.* 1986, New York: John Wiley.

4. M. J. Frisch, G. W. Trucks, H. B. Schlegel, P. M. w. Gill, B. G. Johnson, M. A. Robb, J. R. Cheeseman, G. A. P. T. Keith, J. A. Mongomery, K. Raghavachari, M. A. Al-Laham, V. G. Ortiz., J. B. Foresman, J. Ciolowski, B. B. Stefanov, A. Nanayakkara, M. Challacombe, C. Y. Peng, P. Y. Ayala, W. Chen, M. W. Wong, J. L. Andres, E. Replogle, R. Gomperts, R. L. Martin, D. J. Fox, J. S. Binkly, D. J. Defrees, J. Baker, J. P. Stewart, M. Head-Gordon, C. Gonzalez and J. A. Polple, *Gaussian 94, Revision D.3,* . 1994.

5. T. H. J. Dunning and P. J. Hay, *Modern Theoretical Chemistry.* III, ed. H.F. Schaefer. 1976, New York: Plenum.

6. P. J. Hay and W. R. Wadt, *Journal of Physical Chemistry,* 1985. **82**, 299.

7. P. J. Hay and W. R. Wadt, *Journal of Physical Chemistry,* 1985. **82**, 270.

8. W. R. Wadt and P. J. Hay, *Journal of Physical Chemistry,* 1985. **82**, 284.

9. W. J. Hehre, R. F. Stewart and J. A. Pople, *Journal of Physical Chemistry,* 1969. **51**, 2657.

10. J. B. Collins, P. R. Schleyer, J. S. Binkley and J. A. Pople, *Journal of Physical Chemistry,* 1976. **64**, 5142.

11. M. J. Frisch, A. Frisch and J. B. Foresman, *Gaussian 94 User's Reference.* 1995, Pittsburgh: Gaussian Inc.

12. S. L. Whitbread, J. M. Weeks, P. Valente, M. A. Buntine, S. F. Lincoln and K. P. Wainwright., *Australian Journal of Chemistry,* 1997. **50**, 853-856.

13. E. Teikink, 1998, Crystallographer.

    R-T.

CHAPTER 3

Complexation Studies

of the

Alkali Metal Ions and Silver(I)

by

Three Chiral Pendant Arm Triaza Macrocylic Ligands

3.1   Introduction

A major focus in the study of pendant arm macrocyclic ligands is the determination of the factors influencing the stability of their metal complexes for the equilibrium shown in Equation 3.1 measured by the magnitude of the stability constant, K (Equation 3.2).

$$M^{n+} \quad + \quad L \quad \rightleftharpoons \quad [ML]^{n+} \qquad\qquad 3.1$$

$$K = \frac{[ML^{n+}]}{[M^{n+}][L]} \qquad\qquad 3.2$$

The factors governing complex stability include; size compatibility of the metal ion and ligand cavity, the ability of the ligand to assume a conformation which optimises bonding with the metal ion and the compatibility of the nature of the

donor atoms and the metal ion. The conformation of the solvated ligand may not be the same as the complexed ligand.

The complexation of a metal ion by a ligand involves a competition between the ligand and the solvent for coordination of the metal ion. Thus, complex stability is also largely dependent on the nature of the solvent used and the solvation energy of the metal ion in solution.

Up until the early 1980's, successful complexation of hard alkali metal ions had generally been achieved using ligands containing predominantly oxygen donor atoms, such as cryptands and crown ethers whose selectivity is primarily governed by a 'size-match' compatibility.[1-3]

Unsubstituted tri- and tetraaza macrocycles do not form detectable complexes with the alkali metal ions in aqueous solution, whereas they complex with transition and heavy metal ions strongly.[4] It was thought that one way to increase the alkali metal ion affinity of ligands such as these, would be to add oxygen donor groups into the macrocyclic ring structure, or more readily, through the addition of oxygen donor pendant arms.

Functionalising macrocyclic ligands, 1,4,7-triazacyclononane (tacn) and 1,4,7,11-tetraazacyclododecane (cyclen), with nitrogen attached pendant arms affords a means of forming six or eight coordinate complexes in which there are two groups of facial donors: the macrocyclic nitrogen atoms on the one side and the pendant donors on the other.[5-8] This bi-facial arrangement is a consequence of the fact that invariably, all three or all four pendant donors, project in the same direction, above or below the plane of the macrocycle. The added flexibility of pendant arms on the macrocyclic backbone results in a less rigid ligand cavity than that of the cryptands. Consequently, these pendant arm macrocyclic ligands have an

increased ability to form a cavity of appropriate size upon complexation of a metal ion.

The stability of metal complexes of different sized pendant arm macrocyclic ligands are governed primarily by the size of the chelate ring formed upon complexation rather than the size of macrocylic ring.[9-12] According to molecular mechanics calculations, a five-membered chelate ring will form an ideal low strain geometry with larger metal ions (~2.5 Å) while a six-membered ring requires smaller metal ions (~1.6 Å).[11]

Some of the first alkali metal complexes of pendant arm macrocyclic ligands to be the subject of quantitative stability and kinetic studies were those of 1,4,7,10-tetrakis(2-hydroxyethyl)-1,4,7,10-tetraazacyclododecane (thec12) and its 2-methoxy (tmec12) and 2-(*S*)-hydroxypropyl (*S*-thpc12) analogues (Figure 3.1).[5-7, 13-15]
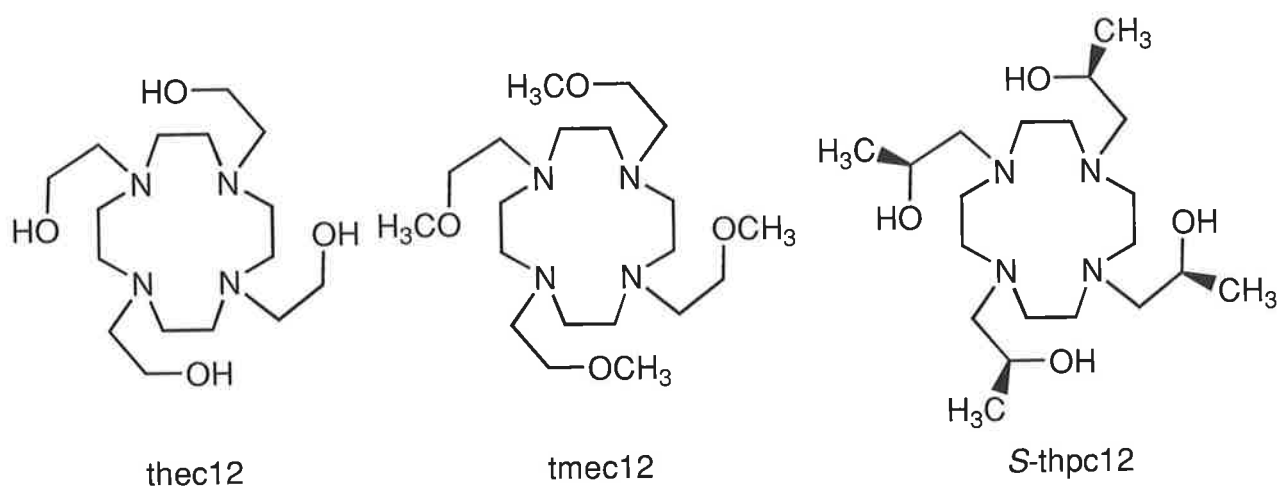
Figure 3.1   Structures of thec12, tmec12 and *S*-thpc12.

These three ligands, all based on the cyclen macrocylic backbone, form stable complexes with the alkali metal ions and silver(I) in methanol and dimethylformamide. The stability constants of these complexes are shown in Table 3.1 along with the stability constants found for thec9.[16]

Table 3.1 Stability constants of silver(I) and the alkali metal complexes of thec9,[17] [M(thec12)]+,[7, 13], [M(tmec12)]+,[14] and [M(S-thpc12]+ [15] determined in methanol and/or dimethylformamide where I = 0.05 mol dm^{-3} (NEt$_4$ClO$_4$).

Ligand	$\log(K/\text{dm}^3\text{mol}^{-1})$					
Solvent	M^+=					
	Li$^+$	Na$^+$	K$^+$	Rb$^+$	Cs$^+$	Ag$^+$
thec9						
Methanol	3.13	3.52	3.23	2.8	2.47	7.65
[M(thec12)]$^+$						
Methanol	3.09	4.53	2.43	2.20	1.90	12.57
Dimethylformamide	2.99	3.37	1.59	1.39	1.23	11.16
[M(tmec12)]$^+$						
Methanol	4.1	6.2	3.9	3.0	2.5	14.2
Dimethylformamide	3.61	5.68	3.62	2.73	2.28	13.73
[M(S-thpc12)]$^+$						
Methanol	4.0	4.8	3.5	3.4	3.2	12.8

It can be seen that the stabilities of the metal complexes in Table 3.1 are largely dependent on the nature of the solvent and the ligand. This is consistent with the complex stability being governed by a combination of (i) the solvation energy of the alkali metal ion, (ii) the electron donating power of the solvent as indicated by the Gutmann donor number (D_N), (iii) the coordinating power of the ligand donor groups and (iv) the ability of the ligand to assume a conformation which optimises the bonding with the metal ion. Thus, as the solvation energy of M^+ increases with the donator power of the solvent the balance among (i)-(iv) changes and the variation of complex stability with the nature of M^+ changes.

The greater stability of the silver(I) complexes of the ligands shown in Table 3.1, when compared with those of the alkali metal ions, is due to the softer Lewis base macrocyclic amine groups competing more effectively with the hard Lewis base solvents for border-line soft silver(I) rather than for the hard Lewis acid alkali metal ions.[18-20] In addition, due to their spherical charge distribution the alkali metal ions have non-directional metal to ligand bonding whereas silver tends to form two strong coaxial bonds.[18, 21] This tendency for the silver(I) complex to be more stable is observed throughout this chapter.

The stability of the silver(I) complex of thec9 in methanol is much smaller than those of the thec12, tmec12 and S-thpc12 (log$K$ of 7.65 for thec9 as compared with 12-14 for the cyclen based ligands). This can be attributed to the strong interaction of silver(I) with the macrocyclic nitrogen donor atoms. A typical bond energy of an Ag-N bond (23 kJ mol^{-1}) is significantly higher than that of an Ag-O bond (6 kJ mol^{-1}), so that the stability of the silver(I) complexes would be proportional to the number of donor nitrogen atoms of the ligand.[22]

A notable trend displayed by all macrocyclic ligands in Table 3.1 is the selectivity for the sodium(I) ion when compared with the other alkali metal complexes ions studied which is consistent with complex stability varying in the sequence $Li^+ < Na^+ > K^+ > Rb^+ > Cs^+$ for each ligand.

Bidentate coordination by the pendant arm group ($-NHCH_2CH_2O-$) and the macrocycle ($-NCH_2CH_2N-$) of each ligand results in five-membered chelate ring formation. Thus, these ligands ideally stabilise metal ions with an ionic radius of 2.5 Å.[12] Based on this, it would be expected that the selectivity of these ligands would greatest for the largest alkali metal ion, caesium, with a six-coordinate radius of 1.67 Å and an eight-coordinate ionic radius of 1.74 Å, and that the stability of the other alkali metal complexes would decrease with size.

In addition, the solvation energy of the group (I) metal ions decrease down the group as the size of the metal ion increases and the charge density decreases; with the smallest ion, lithium(I) possessing the largest solvation energy and caesium(I), the smallest. Thus, it would be predicted that the lithium(I) complexes would have the lowest stability through to caesium(I) with the highest, as the ligand competes with the solvent for complexation.

As this is not observed to be the case, it is evident that the effective size of the ligand cavity plays a significant role in the stability of the complex and outweighs the chelation and solvation effects in determining the selectivity of the ligand.

On the basis of to the ionic radii shown in Table 3.2, it may be inferred that the effective ligand cavity size for the octadentate cyclen based ligands is approximately that of eight-coordinate sodium (1.18 Å) for the least strained situation. By similar reasoning, it may be inferred that the effective ligand cavity size is closer to that of six-coordinate sodium(I) (1.02 Å) for hexadentate thec9.

The changing relative stabilities of the alkali metal thec9 and thec12 complexes probably reflect the varying contributions of ligand cavity size and donor atom number to complex stability.

Table 3.2   Ionic radii of the alkali metal ions and silver(I)[23]

Coordination	Ionic Radii (Å)					
	Li^+	Na^+	K^+	Rb^+	Cs^+	Ag^+
6-coordinate	0.76	1.02	1.38	1.52	1.67	1.19
7-coordinate		1.12	1.46	1.56		1.22
8-coordinate	0.92	1.18	1.51	1.61	1.74	1.28

The change from hydroxy to methoxy pendant arms in thec12 and tmec12, respectively, causes a substantial increase in metal complex stability that is attributable to the greater electron donating power of the methoxy group. The increased stabilities of [M(S-thpc12)]$^+$ when compared with [M(thec12)]$^+$ are probably due to the steric effects of the methyl groups decreasing access of methanol to the metal centre in the decomplexation process.

This study is designed to provide a deeper insight into the thermodynamic and kinetic characteristics of chiral macrocyclic ligands and their metal complexes, with the long-term goal of the production of selective metal ion activated molecular receptors. Thus, the determination of the metal-ion selectivity of ligands such as those discussed above provides an insight into the effective ligand cavity size and the conformation of the complexed ligand.

The group(I) complexation studies of S-thpc9, S-thpec9 and S-thppc9 discussed in this chapter were performed primarily to study the effect of size of the metal ion on the stability of the complex and coincidently find an approximation of the effective cavity size of the ligand. It was also important to make sure the complexes were of sufficient stability to continue with the ^{13}C NMR studies outlined in Chapter 4.

Zinc(II) and cadmium(II) complexes are expected to have a higher stability than those of the alkali metal ions due to their higher charge and tendency to form strong coordinate bonds.[18] In addition to this, the border line hard Lewis acids have an increased affinity for the macrocyclic nitrogen donor atoms than the hard alkali metal ions.

For *S*-thpc9, aqueous titrations with zinc(II) and cadmium(II) were attempted but quantitative results were precluded due to hydroxide precipitation. Non-aqueous silver(I) competitive titrations were also attempted with *S*-thpc9, *S*-thpec9 and *S*-thppc9, but their zinc(II) and cadmium(II) complexes were found to be of a higher stability than that of the silver(I) complex which precluded quantitative stability constant determination.

3.2 Stability constant determination techniques

Several methods have been developed for the determination of metal complex stability constants including calorimetry, nuclear magnetic resonance titration methods, UV-Vis spectroscopy and electrospray ionisation mass spectrometry. However, the most common technique is that of potentiometric titration using either a pH or metal ion specific electrode for aqueous and non-aqueous systems, respectively.

The technique employed to determine the stability of the metal complexes in this study was a potentiometric titration technique using a silver(I) specific electrode and is outlined in the following section.

3.2.1 The potentiometric titration method

The potentiometric titration method was employed to determine the stability constants, K_s, of [M(*S*-thpc9)]$^+$, [M(*S*-thpec9)]$^+$ and [M(*S*-thppc9)]$^+$, where M = Ag$^+$, Li$^+$, Na$^+$, K$^+$, Rb$^+$ and Cs$^+$ in either methanol or dimethylformamide depending on the solubility of the ligand and the complex formed.

The silver(I) complex stability constants were determined through direct titration using silver electrodes. This involves titrating a solution of free silver(I) with a solution of the ligand and measuring the variation of the amount of free silver(I).

The relationship between the electrode potential, E, and the free silver ion concentration is pseudo-Nernstian and is given by Equation 3.3, where E_0 is the standard electrode potential and C is a constant typifying the equilibrium studied.

$$E = E_0 + C\ln[M^+] \qquad\qquad \textbf{3.3}$$

For the alkali metal ions, the stability constants, K, were determined by a competitive titration method. This involves the titration of the free silver(I) with the ligand in the presence of a competing metal ion (Equation 3.4). The competition between the metal ion, M^+, and silver(I) is again monitored by measuring the free silver(I) using a silver(I) selective electrode.

$$[ML]^+ + Ag^+ \rightleftharpoons [AgL]^+ + M^+ \qquad\qquad \textbf{3.4}$$
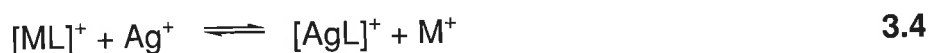
Thus, if the stability constant of the silver(I) complex, $K(Ag^+)$, is known then the stability constant of the metal complex, $K(M^+)$, can be determined from;

$$K_e = \frac{[AgL^+][M^+]}{[Ag^+][ML^+]} \qquad\qquad \textbf{3.5}$$

$$K(M^+) = \frac{K(Ag^+)}{K_e} \qquad\qquad \textbf{3.6}$$

The FORTRAN program VISP was used to extract the stability constants, $K(M^+)$, from the experimental data. The basis of the calculations is outlined below. If $[Ag^+]_t$ and $[L]_t$ are the total (or initial) concentrations of metal ion and ligand, respectively, and $[Ag^+]$ and $[L]$ represent the free metal ion and ligand, respectively, then for the case of a direct titration K is given by:

$$K(Ag^+) = \frac{[AgL^+]}{[Ag^+][L]} \qquad\qquad \textbf{3.7}$$

or:

$$K(Ag^+) = \frac{[Ag^+]_t - [Ag^+]}{[Ag^+][L]}$$

3.8

where:

$$[L] = [L]_t - [Ag^+]_t + [Ag^+]$$

3.9

substituted into 3.7 becomes:

$$K = \frac{[Ag^+]_t - [Ag^+]}{[Ag^+]([L]_t - [Ag^+]_t + [Ag^+])}$$

3.10

expanded becomes:

$$K = \frac{[Ag^+]_t - [Ag^+]}{[Ag^+][L]_t - [Ag^+][Ag^+]_t + [Ag^+]^2}$$

3.11

rearranged becomes:

$$K [Ag^+]^2 + (K [L]_t - K [Ag^+]_t + 1)[Ag^+] - [Ag^+]_t = 0$$

3.12

solving for [Ag$^+$] gives:

$$[Ag^+] = \frac{K ([Ag^+]_t - [L]_t - 1 + \sqrt{K\ 2([L]_t - [Ag^+]_t + 2K\ ([L]_t + [Ag^+]) + 1}}{2K}$$

3.13

Using Equation 3.13 VISP varies K over a range with set increments until the sum of residuals is minimised giving a best fit value for K.

In the case of a competitive titration the equilibrium is described by Equation 3.5. If $[Ag^+]_t$, $[M^+]_t$ and $[L]_t$ are used for the total (or initial) concentration of silver, metal ion and ligand respectively and $[Ag^+]$, $[M^+]$ and $[L]$ is used to represent the solvated

silver, metal ion and ligand in solution, the K_e as defined in Equation 3.5 is given by:

$$K_e = \frac{[Ag^+]_t - [Ag^+]}{[Ag^+]} \times \frac{[M^+]}{[ML^+]} \qquad \textbf{3.14}$$

where:

$$[M^+] = [M^+]_t - [ML^+]_t + [Ag^+]_t - [Ag^+] \qquad \textbf{3.15}$$

and:

$$[ML^+] = [ML^+]_t - [Ag^+]_t + [Ag^+] \qquad \textbf{3.16}$$

substitution of equations 3.15 and 3.16 into 3.14 gives:

$$K_e = \frac{[Ag^+]_t - [Ag^+]}{[Ag^+]} \times \frac{[M^+]_t - [ML^+]_t + [Ag^+]_t - [Ag^+]}{[ML^+]_t - [Ag^+]_t + [Ag^+]} \qquad \textbf{3.17}$$

which expands to:

$$K_e = \frac{[Ag^+]_t([M^+]_t - [ML^+]_t + [Ag^+]_t - 2[Ag^+]) + [Ag^+](-[M^+]_t + [ML^+]_t - [Ag^+])}{[Ag^+]}$$

$$\textbf{3.18}$$

which when rearranged becomes:

$$(K_e^{-1})[Ag^+]^2 + (K_e[ML^+]_t - K_e[Ag^+]_t + 2[Ag^+]_t + [M^+]_t - [ML^+]_t)[Ag^+]$$
$$+ ([ML^+]_t - [M^+]_t - [Ag^+]_t)[Ag^+]_t = 0 \qquad \textbf{3.19}$$

and solving for $[Ag^+]$ gives:

$$[Ag^+] = (K_e^{-2})[Ag^+]_t + (1-K_e)[ML^+]_t - [M^+]_t + \sqrt{S} \qquad \textbf{3.20}$$

where S = $K_e^2([ML^+]_t - [Ag^+]_t + K_e([M^+]_t(2[Ag^+]_t + [ML^+]_t) + 2[ML^+]_t([Ag^+]_t - [ML^+]_t) + ([ML^+]_t - [M^+]_t)^2$

Using equation 3.20, VISP varies K_e over a range with set increments until the sum of residuals is minimised, giving a best fit value for K_e, which then allows the derivation of the stability constant $K(M^+)$ using Equation 3.5.

3.3   Stability constants of the *S*-thpc9 complexes of silver(I) and the alkali metal ions

The stability constants of the silver(I) and the alkali metal complexes of *S*-thpc9 were determined in dry methanol and dry dimethylformamide. The values obtained are shown in Table 3.3 below.

Table 3.3 Stability constants of [M(*S*-thpc9)]$^+$ in methanol and dimethylformamide along with those of [M(thec9)]$^+$ in methanol for comparison determined by potentiometric titration at 298.2 K and $I = 0.05$ mol dm^{-3} (NEt$_3$ClO$_4$). The errors in log(K / dm^3 mol^{-1}) are less than 0.05.

Ligand & Solvent	log(K / dm^3 mol^{-1}) $M^+=$					
	Li$^+$	Na$^+$	K$^+$	Rb$^+$	Cs$^+$	Ag$^+$
[M(thec9)]$^{+\,a}$						
Methanol	3.13	3.52	3.23	2.8	2.47	7.65
[M(*S*-thpc9)]$^+$						
Methanol	3.39	2.50	*b*	*b*	*b*	7.39
Dimethylformamide	3.29	2.29	2.28	2.27	2.29	7.59

^{a}From reference 16

^{b}Insufficient solubility for titrations

The ligand was found to be selective for lithium(I) in both methanol and dimethylformamide. Due to the insolubility of metal salts, the stability constants for the potassium(I), rubidium(I) and caesium(I) complexes could not be determined. The stability trend found in dimethylformamide was consistent with the sequence

Li$^+$ >> Na$^+$ $\approx$ K$^+$ $\approx$ Rb$^+$ $\approx$ Cs$^+$.

As previously discussed, it would be expected that the selectivity of *S*-thpc9 (and the other ligands discussed in this chapter) would be directed towards the largest alkali metal ion, caesium, that the stability of the other alkali metal ions would decrease with size due to five-membered ring chelation and the relative solvation energies of the metal ions.[23]

As *S*-thpc9 is found to be selective for lithium(I), it is evident that the effective cavity size of the free ligand plays a significant role in the stability of the complex and outweighs the chelation and metal ion solvation effects.

The increase in stability of $[Li(S\text{-thpc9})]^+$ when compared with $[Li(thec9)]^+$ in methanol is probably due to the steric nature of the methyl groups of *S*-thpc9 decreasing the access of the methanol to the metal centre in the decomplexation process.

The stability of $[Na(thec9)]^+$, $[K(thec9)]^+$, $[Rb(thec9)]^+$ and $[Cs(thec9)]^+$ are higher than those of their *S*-thpc9 analogues probably because the latter ligand has a smaller effective ligand cavity size, inferring the effective cavity size of *S*-thpc9 to be a optimal fit for six-coordinate lithium(I) (0.76Å) rather than six-coordinate sodium(I) (1.02Å) for which thec9 is selective.

The Gaussian 94 *ab initio* gas phase optimised geometry of $[Li(S\text{-thpc9})]^+$ (Figure 2.12) shows the lithium(I) ion encapsulated by the ligand in a bifacial arrangement where the metal ion is situated 1.17 Å from the oxygen donor atom plane and 1.55 Å from the nitrogen donor atom plane. The larger metal ions become situated further from the nitrogen plane and closer to the oxygen donor atom plane and in the case of caesium, the metal ion is situated 0.1 Å outside of the ligand cavity (see Figures 2.12-16 and Table 2.2). The oxygen to oxygen and nitrogen to nitrogen distances also increase as the ligand expands to accommodate the larger metal ions. As oxygen is a harder Lewis base than nitrogen, the metal to oxygen distance would be expected to increase down the group as the metal ions get larger and less electron dense. The fact that the opposite occurs is consistent with the effective ligand cavity size of *S*-thpc9 being too small to encapsulate the larger

alkali metal ions and a more compatible size match with lithium(I). The calculated relative gas-phase Δ energy series outline in section 2.6 is also consistent with this, showing the greatest electronic stabilisation energy for the lithium(I) complex of *S*-thpc9 (Figure 2.31). A similar outcome is observed from the gas phase geometry optimised structures and calculated energy series of the other ligands discussed in the two following sections.

The increase in D_N in going from methanol to dimethylformamide results in a decrease in stability of the group(I) metal ion complexes with *S*-thpc9 as the because dimethylformide competes more effectively for the metal ion.

3.4 Stability constants of the *S*-thpec9 complexes of silver(I) and the alkali metal ions

The stability constants of silver(I) and the alkali metal complexes of *S*-thpec9 were determined in dry dimethylformamide. This ligand was insufficiently soluble in both water and methanol for stability constant determination in those solvents.

The stability constants determined are shown in Table 3.4 along with the corresponding values for *S*-thpc9 and those of its twelve membered macrocyclic ring analogue *R*-thpec12 for comparison.

Table 3.4 Stability constants of $[M(S\text{-thpec9})]^+$ along with $[M(S\text{-thpc9})]^+$ and $[M(R\text{-thpec12})]^+$ [24] determined in dimethylformamide by potentiometric titration at 298.2 K and $I = 0.05$ mol dm^{-3} (NEt$_3$ClO$_4$). The errors in log(K/dm^3 mol^{-1}) are less than 0.05.

Ligand	log(K/dm^3 mol^{-1})					
	M$^+$=					
	Li$^+$	Na$^+$	K$^+$	Rb$^+$	Cs$^+$	Ag$^+$
$[M(S\text{-thpc9})]^+$	3.29	2.29	2.28	2.27	2.29	7.59
$[M(S\text{-thpec9})]^+$	3.64	2.03	1.91	1.91	1.62	7.59
$[M(R\text{-thpec12})]^+$	3.13	4.25	4.10	3.57	3.47	8.14

As for *S*-thpc9, *S*-thpec9 shows a selectivity for the smallest of the alkali metal ions and is consistent with complex stability decreasing with M$^+$ in the sequence: Li$^+$ > Na$^+$ ≈ K$^+$ ≈ Rb$^+$ > Cs$^+$.

As *S*-thpec9 is found to be selective for lithium(I), it is evident that the effective cavity size plays a significant role in the stability of the complex and again, outweighs the chelation and metal ion solvation effects.

The increase in stability of [Li(*S*-thpec9)]$^+$ when compared with [Li(*S*-thpc9)]$^+$ is probably due to the increased steric effects of the pendant arm phenyl substituents in *S*-thpec9 when compared with the pendant arm methyl groups in *S*-thpc9 more effectively decreasing the access of dimethylformamide to the metal centre in the decomplexation process.

The decrease in stability of [Na(*S*-thpec9)]$^+$ when compared with [Na(*S*-thpc9)]$^+$ is indicative of a decrease in effective ligand cavity size which would have a destabilising effect on sodium(I) and larger alkali metal complexes where the stabilities are even more dramatically reduced when compared those complexes of *S*-thpc9. For example, in the case of caesium(I), the stability drops from 2.29 for *S*-thpc9 to 1.62 for *S*-thpec9.

This, along with the increased stability of [Li(S-thpec9)]$^+$ when compared to [Li(*S*-thpc9)]$^+$, suggests that the effective ligand cavity size of *S*-thpec9 may be more compatible with six-coordinate lithium(I) than the larger group(I) metal ions sodium(I) to caesium(I) and also more compatible with lithium(I) than is *S*-thpc9. However, the influence of substituting methyl groups for phenyl groups may change the ability of dimethylformamide to solvate the complexes, which in turn may affect their complexation and decomplexation rates.

Gaussian 94 *ab initio* gas phase optimised geometries of [M(*S*-thpec9)]$^+$ (where M = Li, Na, K, Rb and Cs) and the calculated gas phase Δ energy series (section 2.6) correspond with these results (see Figures 2.19-23) and suggest lithium(I) to be the most compatible size-match.

3.5 Stability constants of the *S*-thppc9 complexes of silver(I) and the alkali metal ions

The stability constants of silver(I) and the alkali metal complexes lithium(I) to caesium(I) of *S*-thppc9 were determined in dry dimethylforamide. The ligand was insufficiently soluble in both water and methanol for stability constant determination in those solvents.

The stability constants determined are shown in Table 3.4 below along with those of *S*-thpc9 and *S*-thpec9 for comparison.

Table 3.4 Stability constants of [M(*S*-thppc9)]$^+$ along with [M(*S*-thpc9)]$^+$ and [M(*S*-thpec9)]$^+$ determined in dimethylformamide by potentiometric titration at 298.2 K and I = 0.05 mol dm^{-3} (NEt$_3$ClO$_4$). The errors in log(K/dm^3 mol^{-1}) are less than 0.05.

Ligand	log(K/dm^3 mol^{-1})					
	M$^+$=					
	Li$^+$	Na$^+$	K$^+$	Rb$^+$	Cs$^+$	Ag$^+$
[M(*S*-thpc9)]$^+$	3.29	2.29	2.28	2.27	2.29	7.59
[M(*S*-thpec9)]$^+$	3.64	2.03	1.91	1.91	1.62	7.59
[M(*S*-thppc9)]$^+$	3.01	2.65	2.66	2.65	2.42	7.59

As for both *S*-thpc9 and *S*-thpec9, *S*-thppc9 shows a selectivity for the smallest of the alkali metal and complex stability decreases with M+ in the sequence: Li$^+$ > Na$^+$ ≈ K$^+$ ≈ Rb$^+$ > Cs$^+$.

As *S*-thppc9 is also found to be selective for lithium(I), it is evident that the effective cavity size of the ligand again plays a significant role in the stability of the complex outweighs the chelation and metal ion solvation effects.

The selectivity for the smaller lithium(I) ion indicates the effective cavity size of *S*-thppc9 to be closer to the ionic radii of six-coordinate lithium(I), 0.76Å, such that the complexes of the larger metal ions are less stable.

The stability of the lithium(I) complexes decrease in the sequence: $[Li(S\text{-thpec9})]^+$ > $Li(S\text{-thpc9})]^+$ > $[Li(S\text{-thppc9})]^+$.

The stability of the sodium(I), potassium(I), rubidium(I) and caesium(I) decrease in the sequence: $[M(S\text{-thppc9})]^+$ > $[M(S\text{-thpc9})]^+$ > $[M(S\text{-thpec9})]^+$ where M = Na, K, Rb and Cs. This is consistent with the effective cavity size of *S*-thppc9 being larger than the other two ligands, the effective ligand cavity size of *S*-thpec9 being the smallest of the three and the most compatible with lithium(I).

Gaussian 94 *ab initio* gas phase optimised geometries of $[M(S\text{-thppc9})]^+$ (where M = Li, Na, K, Rb and Cs) are compatible with these conclusions (see Figures 2.26-30) and suggest lithium(I) to be the most compatible cavity size-match.

Thus, is seems that the addition of the larger, more flexible pendant arm benzyl group has had the effect of increasing the cavity size from that engendered by both the methyl and the phenyl groups such that the effective ligand cavity size trend according to pendant arm substituent is consistent with the decreasing sequence: benzyl > methyl > phenyl. However, the influence of the methyl, phenyl or benzyl substituent may change the ability of dimethylformamide to solvate the complexes which in turn may change the ability of dimethylformamide to solvate the complexes, which in turn may affect their complexation and decomplexation rates.

References

1. B. G. Cox, R. Garcia-Rosas and H. Schneider, *Journal of the Amercican Chemical Society*, 1981. **103**, 1384.

2. J.-M. Lehn, *Journal of Inclusion Phenomena*, 1988. **6**, 351.

3. J.-M. Lehn, *Accounts of Chemical Research*, 1988. **11**, 49.

4. T. A. Kaden, *Topics of Current Chemistry*, 1984. **121**, 154-170.

5. M. L. Turonek, P. Clarke, G. S. Lawrence, S. F. Lincoln, P.-A. Pittet, S. Politis and K. P. Waiwright, *Inorganic Chemistry*, 1993. **32**, 2195.

6. R. S. Dhillon, A. K. W. Stephens, S. L. Whitbread, S. F. Lincoln and K. P. Wainwright., *Journal of the Chemical Society, Chemical Communications*, 1995. **1**, 97.

7. S. L. Whitbread, S. Politis, A. K. W. Stephens, J. Lucas, R. S. Dhillon, S. F. Lincoln and K. P. Wainwright., *Journal of the Chemical Society, Dalton Transactions*, 1996, 1379.

8. J. M. Weeks, M. R. Taylor and K. P. Wainwright, *Journal of the Chemical Society, Dalton Transations*, 1997, 317.

9. R. D. Hancock, *Pure and Applied Chemistry*, 1986. **58**, 1445.

10. R. D. Hancock, *Progress in Inorganic Chemistry*, 1989. **37**, 187.

11. R. D. Hancock, *Accounts of Chemical Research*, 1990. **23**, 253.

12. R. D. Hancock, R. Bhaven, P. W. Wade, J. C. A. Boeyens and S. M. Dobson, *Inorganic Chemistry*, 1989. **28**, 187.

13. A. K. W. Stephens and S. F. Lincoln, *Journal of the Chemical Society, Dalton Transactions*, 1993, 2123.

14. A. K. W. Stephens, R. S. Dhillon, S. E. Madbak, S. L. Whitbread and S. F. Lincoln, *Inorganic Chemistry*, 1996. **35**, 2019-2024.

15. R. Dhillon, S. E. Madbak, F. G. Ciccone, M. A. Buntine, S. F. Lincoln and K. P. Wainwright, *Journal of the American Chemical Society*, 1997. **119**, 6126.

16. S. L. Whitbread, J. M. Weeks, P. Valente, M. A. Buntine, S. F. Lincoln and K. P. Wainwright, *Australian Journal of Chemistry*, 1997. **50**, 853.

17. S. L. Whitbread, J. M. Weeks, P. Valente, M. A. Buntine, S. F. Lincoln and K. P. Wainwright, *Australian Journal of Chemistry*, 1997. **50**, 853.

18. F. A. Cotton and G. Wilkinson, *Advanced Inorganic Chemitry*. 5th Edition ed. 1988, New York: Inter-Science.

19. R. G. Pearson, *Coordination Chemistry Reviews*, 1990. **100**, 403.

20. J. Emsley, *Chemical Society Reviews*, 1980. **9**, 91.

21. R. D. Hancock, P. W. Wade, M. P. Ngwenya, A. S. de Sousa and K. V. Damu, *Inorganic Chemistry*, 1990. **29**, 1968.

22. H. J. Buschmann, *Inorganica Chimica Acta*, 1985. **102**, 95.

23. R. D. Shannon, *Acta Crystallographica., Section A*, 1976. **32**, 751.

24. S. L. Whitbread, P. Valente, M. A. Buntine, P. Clements, S. F. Lincoln, M. R. Taylor and K. P. Wainwright, *Journal of the American Chemical Society*, 1998. **43**, 120.

CHAPTER 4

Diastereomeric Exchange Processes
of the
Lithium(I) and Sodium(I) complexes
of three
Pendant Arm Triaza Macrocyclic Chiral Ligands

4.1   Introduction

The nature of the pendant arm is influential in governing the structure, stability and lability of pendant arm macrocyclic ligands and their metal complexes.[1-4] The increased denticity of pendant arm macrocyclic ligands when compared with their macrocyclic analogues may allow the ligand to completely encapsulate the metal ion upon complexation. This results in stereochemistries and intramolecular processes in these complexes that are unavailable to those of the parent macrocycle.[5-7] This has been observed for a number pendant arm polyaza macrocyclic ligands including tmec12,[8] thec12,[9] *S*-thpc12 [10] and *R*-thpec12.[7] These ligands encapsulate the metal ion in a bifacial arrangement with the macrocyclic nitrogen donors situated to one side of the metal ion, and the pendant donor atoms to the other.

The conformation of a metal complex determined by either X-ray crystallography or modelled through gas phase molecular orbital calculations may be used as a guide to the conformation in solution.

Dynamic Nuclear Magnetic Resonance Spectroscopy (DNMR) is an established technique that can be used for the determination of intramolecular and intermolecular chemical exchange rates of a system in solution.[11-15] Generally, it may be used to determine rate constants in the range of 10^{-1} to 10^{-6} s^{-1}.

NMR spectroscopy can be used to deduce metal complex coordination geometries and interchanging macrocyclic ring conformations that are in slow exchange on the NMR time scale. A specific example is the enantiomeric exchange of tris-(hydroxy)-1,4,7-triazacyclononane (thec9) where ^{13}C DNMR has been successfully utilised to determine the nature and thermodynamic properties of this process.[16]

4.1.1 Enantiomeric Exchange of tris-(hydroxy)-1,4,7-triazacyclononane (thec9) and its Lithium(I) and Sodium(I) Complexes in Solution

Variable temperature ^{13}C NMR spectroscopic studies (Figure 4.1) are consistent with the lithium(I) and sodium(I) complexes of hexadentate thec9 existing as two rapidly inter-converting enantiomers in solution (Figure 4.2).[16] The ligand cavity forms a distorted trigonal prismatic geometry where the triangular plane formed by the oxygen atoms can either twist to the right (Δ) or to the left (Λ) of the triangular plane formed by the nitrogen donors below (Figure 4.2).

The intramolecular exchange processes of the free thec9 are too rapid for detection within the NMR time scale. However, the addition of each of the group I metal ions slows the enantiomerisation sufficiently for detection at low temperature. The ^{13}C NMR spectra of [Li(thec9)]$^+$ and [Na(thec9)]$^+$ in ^{12}C enriched $^2H_4$ methanol show two broad macrocyclic ring ^{13}C resonances, *a* and *b*, at low temperature which coalesce to a singlet at higher temperatures (Figure 4.1). No modifications of the ^{13}C resonances, *c* and *d*, assigned to the pendant arm carbons $-CH_2N-$ and $-OCH_2-$, occur apart from some narrowing as the temperature increases and viscosity decreases. This is consistent with enantiomerisation causing macrocyclic ring carbon exchange between

inequivalent environments *a* and *b*, while pendant arm $-CH_2N-$ and $-OCH_2-$ carbons, *c* and *d*, exchange between equivalent environments (Figure 4.2). The broadening of resonances *a* and *b* is a result of enantiomerisation occurring just within the slow exchange regime.
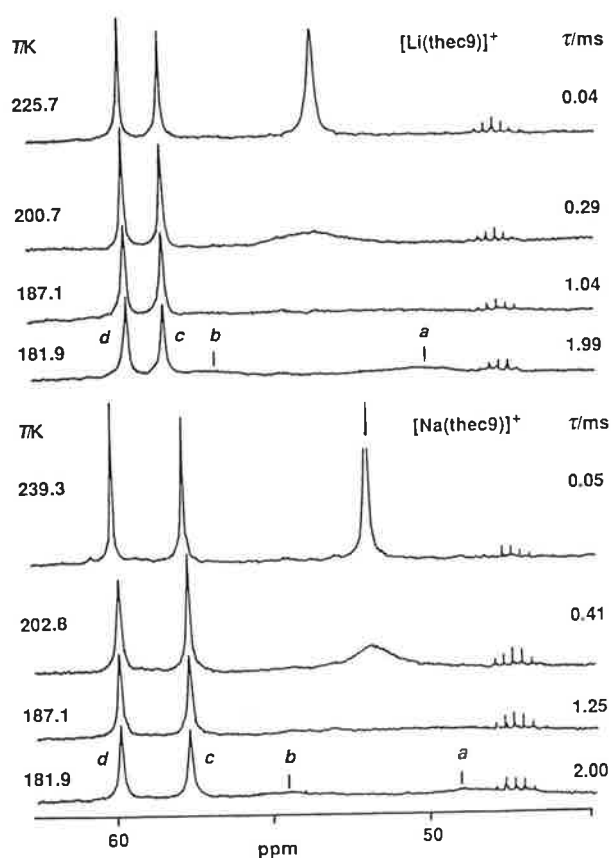
Figure 4.1 Temperature variations of the ^{13}C NMR spectra of [Li(thec9)][+] and [Na(thec9)][+] (0.1 mol dm^{-3}) in ^{12}C enriched [2]H_4 methanol at 75.47 MHz. Experimental temperatures and τ values derived from complete lineshape analysis of coalescing doublet arising from the macrocyclic ring carbons, *a* and *b*, appear to the left and the right of the figure, respectively.[16]
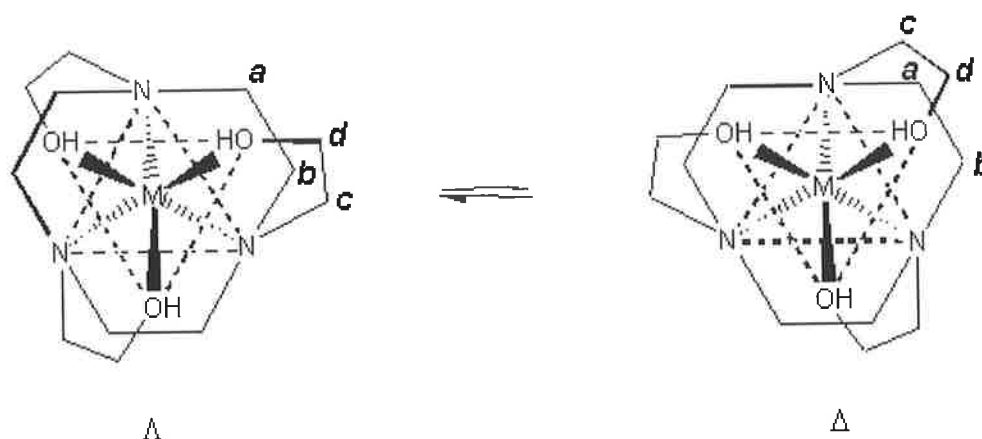
Figure 4.2 The delta (Δ) and lambda (Λ) enantiomers of [M(thec9)]$^{m+}$ shown in equilibrium. The twist angle from trigonal prismatic stereochemistry is exaggerated for the purposes of the illustration.

This enantiomerisation process requires a single inversion at each nitrogen centre occurring through either a concerted or sequential process without displacement of the metal centre from between the oxygen and nitrogen planes of thec9 (Figure 4.2).

It was anticipated that the incorporation of chiral pendant arms would result in either the Λ or the Δ conformation to be thermodynamically favoured and that it may exist solely in solution.

4.2 Introduction to Dynamic Nuclear Magnetic Resonance Spectroscopy

DNMR is founded on the effects of the chemical exchange process on the NMR lineshape. To quantitatively describe how this can be used to measure this kinetic process a mathematical description along with spectroscopic theory is required and is outlined below.

4.2.1 Theoretical treatment of DNMR for two-site chemical exchange

The level of theoretical treatment of DNMR varies from case to case. The following treatment uses a classical mechanical model and applies only for two-site chemical exchange and uncoupled nuclei.

In a typical NMR experiment a magnetic field, B_0, is applied to the sample along the z axis. This causes the individual magnetic moments, μ, of the sample nuclei to precess about the z axis at the Larmor frequency, ω_0, so that the lowest energy state occurs when the nuclear spins of the nuclei are aligned with B_0. This state is favoured by the Boltzman distribution and leads to a net magnetic moment M consisting of only the z component, M_z, while the x and y components, M_x and M_y, remain zero.

The application of a second and smaller oscillating magnetic field, B_1, rotating clockwise in the xy plane at frequency ω gives rise to a total magnetic field B, where;

$$B = (B_1\cos\omega t,\ B_1\sin\omega t,\ B_0) \qquad \textbf{4.1}$$

Consequently, M is deviated towards the xy plane resulting in non-zero M_x and M_y values (both have a maximum when $\omega = \omega_0$) and a diminished M_z.

The relaxation process whereby M_z regains its initial equilibrium value M_{zeq} is a first order process characterised by the spin lattice or longitudinal relaxation time, T_1. The decay of the transverse components of M, M_x and M_y, to an equilibrium value of zero is characterised by the transverse relaxation time, T_2.

The time dependence of M in the stationary frame (with Cartesian co-ordinates (x, y, z)) is described by the Bloch equations[17] which incorporate the effect of B_1 on M and also the effect of the longitudinal and transverse relaxation.

$$\frac{dM_x}{dt} = \gamma(M_y B_0 + M_z B_1 \sin \omega t) - \frac{M_x}{T_2} \qquad \textbf{4.2}$$

$$\frac{dM_x}{dt} = \gamma(-M_x B_0 + M_z B_0 \cos \omega t) - \frac{M_y}{T_2} \qquad \textbf{4.3}$$

$$\frac{dM_z}{dt} = \gamma(-M_x B_1 \sin \omega t - M_y B_1 \sin \omega t) - \frac{(M_z - M_{zeq})}{T_2} \qquad \textbf{4.4}$$

where γ is the gyromagnetic ratio.

The Bloch equations can be conveniently reformulated using a rotating frame of reference, (x', y', z'), so that they may be expressed as;

$$\frac{dM_{xy}}{dt} = -\alpha M_{xy} - i\gamma B_1 M_{zeq} \qquad \textbf{4.5}$$

$$\frac{dM_z}{dt} = \gamma v B_1 + \frac{(M_{zeq} - M_z)}{T_1} \qquad \textbf{4.6}$$

where;　　　M_{xy} is the transverse magenetisation,

　　　　　　v is the component of M along the y' axis 90° out of phase with B_1

and　　　　$\alpha = \frac{1}{T_2} - i(\omega_0 - \omega)$,

Thus, it can now be seen that the variation of M_z and hence the energy of the system, is dependant on v which corresponds to the absorption mode of the NMR signal.

The NMR measurements performed in this work were carried out using the pulsed Fourier Transform technique. The NMR absorption mode lineshape obtained from the pulsed Fourier transform experiment is equivalent to that obtained from continuous wave slow passage experiment. As the continuous wave experiment is more easily visualised, the following discussion will be based on this technique.

Under continuous wave slow passage conditions, ω is swept slowly through ω_0 so that $\dfrac{dMxy}{dt} = \dfrac{dMz}{dt} = 0$. If B_1 is small, so that $M_z \sim M_{zeq}$ and M_{xy} is small, the form of the absorption mode lineshape is given by;

$$v = -M_{zeq} \frac{\gamma B_1 T_2}{1 + T_2^2 (\omega_0 - \omega)^2 + \gamma^2 B_1^2 T_1 T_2} \qquad \textbf{4.7}$$

Generally, B_1 is so small that the term $\gamma^2 B_1^2 T_1 T_2$ is negligible and can be ignored so that the absorption mode lineshape is described by a Lorentzian function;

$$v = -M_{zeq} \frac{\gamma B_1 T_2}{1 + T_2^2 (\omega_0 - \omega)^2} \qquad \textbf{4.8}$$

The Bloch equations may now be modified to incorporate the effects of chemical exchange. These modifications are only applicable where the exchange of nuclear spins induces transverse relaxation only (adiabatic exchange) and where there is no occurrence of spin-spin coupling between exchanging nuclear spins. In an uncoupled two site exchange case, the nucleus exchanges between sites **a** and **b** at a rate given by;

$$k_a\chi_a = k_b\chi_b; \quad k_a = \frac{1}{\tau_a}, \quad k_b = \frac{1}{\tau_b} \qquad \text{4.9}$$

where χ_a and χ_b are the relative populations and τ_a and τ_b are the mean lifetimes of the nucleus at sites **a** and **b** respectively.

It is assumed that the time required for a nuclear spin to transfer from site **a** to site **b** is so small that no nuclear spin precession occurs and that a nucleus arrives at site **b** with it's phase memory of site **a** intact, and vice versa. This transfer causes dephasing of the nuclear spins at site **b** and to an increase in M_{xyb}, the tranverse magnetisation of site **b** at the rate M_{xya}/τ_a and a decrease in M_{xya} at the same rate. Similarly, transfer of a nuclear spin from site **b** to **a,** causes dephasing at site **a** and an increase in M_{xya} at the rate M_{xyb}/τ_b and decreases M_{xyb} at the same rate;

$$\frac{dM_{xya}}{dt} = \frac{M_{xyb}}{\tau_b} - \frac{M_{xya}}{\tau_a}$$

$$\frac{dM_{xyb}}{dt} = \frac{M_{xya}}{\tau_a} - \frac{M_{xyb}}{\tau_b} \qquad \text{4.10}$$

Incorporation of these effects into the Bloch equations leads to the following;

$$\frac{dM_{xya}}{dt} = -\alpha_a M_{xya} - i\gamma B_1 M_{zeqa} + \frac{M_{xyb}}{\tau_b} - \frac{M_{xya}}{\tau_a} \qquad \text{4.11}$$

$$\frac{dM_{xyb}}{dt} = -\alpha_b M_{xyb} - i\gamma B_1 M_{zeqb} + \frac{M_{xya}}{\tau_a} - \frac{M_{xyb}}{\tau_b} \qquad \text{4.12}$$

where; $\qquad \alpha_a = \frac{1}{T_{2a}} - i(\omega_0 - \omega) \qquad\qquad$ **4.13**

and
$$\alpha_b = \frac{1}{T_{2b}} - i(\omega_0 - \omega)$$
4.14

Under continuous wave slow passage conditions, the M_z components do not differ significantly from M_{zeq} and therefore;

$$M_{za} = M_{zeqa} = \chi_a M_{zeq} \quad \text{and} \quad M_{zb} = M_{zeqb} = \chi_b M_{zeq}$$
4.15

$$\frac{dM_{xya}}{dt} = \frac{dM_{xyb}}{dt} = 0$$
4.16

The total transverse magnetisation $M_{xy}=M_{xya}+M_{xyb}$ may now be expressed in terms of τ_a and τ_b;

$$M_{xy} = \frac{-i\gamma B_1 M_{zeq}[\tau_a + \tau_b + \tau_a \tau_b (\alpha_a \chi_a + \alpha_b \chi_b)]}{(1 + \alpha_a \tau_a)(1 + \alpha_a \tau_b) - 1}$$
4.17

The NMR absorption lineshape v at frequency ω (rads^{-1}) is proportional to the imaginary part of M_{xy} and can be expressed in the form;

$$v = \frac{-\gamma B_1 M_{zeq} \left\{ Y \left[1 + \tau \left(\frac{\chi_b}{T_{2a}} + \frac{\chi_a}{T_{2b}} \right) \right] + QR \right\}}{Y^2 + R^2}$$
4.18

where;
$$\tau = \chi_b \tau_a + \chi_a \tau_a$$

$$\Delta\omega = \omega_{0a} - \omega_{0b}$$

$$\delta\omega = \frac{1}{2}|\omega_{0a} - \omega_{0b}| - \omega$$

$$Y = \tau \left(\frac{1}{T_{2a}T_{2b}} - \delta\omega^2 + \frac{\Delta\omega^2}{4} \right) + \frac{\chi_a}{T_{2a}} + \frac{\chi_a}{T_{2a}}$$

$$Q = \tau \left(\delta\omega - \frac{\Delta\omega}{2}(\chi_a - \chi_b) \right)$$

$$R = \delta\omega \left[1 + \tau \left(\frac{1}{T_{2a}} + \frac{1}{T_{2b}} \right) \right] + \frac{\Delta\omega\tau}{2} \left(\frac{1}{T_{2b}} - \frac{1}{T_{2a}} \right) + \frac{\Delta\omega}{2}(\chi_a - \chi_b)$$

The NMR lineshape for systems undergoing chemical exchange may be calculated from the above expression. When the rate of exchange is slow (when τ_a and τ_b are large) the NMR spectrum consists of two Lorentzian lineshapes centred at ω_{0a} and ω_{0b}. As the rate of exchange increases, τ_a and τ_b decrease which causes to the two resonances to broaden and coalesce to form a single resonance. The very slow exchange limit occurs when the rate of exchange between sites **a** and **b** is too slow to cause any measurable broadening of the two resonances. The very fast exchange limit occurs when the rate of exchange between sites **a** and **b** is significantly fast so that the coalesced lineshape is characterised by a chemical shift and linewidth that is simply the weighted average of those characterising sites **a** and **b** in the absence of exchange.

The variation in lineshape as a function of exchange rate will now be considered in more detail.

4.2.1.1 Slow exchange

Very Slow Exchange Limit

Under these conditions;

$$\tau_a^{-1}, \tau_b^{-1} \ll |\omega_{0a} - \omega_{0b}|, T_{2a}^{-1}, T_{2b}^{-1}$$

That is, the rate of exchange between sites **a** and **b** is sufficiently small compared with the chemical shift difference (frequency separation) between the two sites and Equation 4.17 approximates to;

$$v = \frac{-\gamma B_1 \chi_a M_{zeq} T_{2a}^{-1}}{T_{2a}^{-2} + (\omega_{0a} - \omega)^2} + \frac{-\gamma B_1 \chi_b M_{zeq} T_{2b}^{-1}}{T_{2b}^{-2} + (\omega_{0b} - \omega)^2} \qquad \textbf{4.19}$$

Equation 4.19 contains no chemical exchange parameters and describes two lorentzian lineshapes centered at ω_{0a} and ω_{0b}.

Slow Exchange Limit

Under these conditions;

$$\tau_a^{-1}, \tau_b^{-1} << |\omega_{0a} - \omega_{0b}|, \tau_{2a}^{-1} \approx T_{2a}^{-1}, \tau \approx T_{2b}^{-1}$$

The exchange rate is now greater than the previous case, although still small compared with the chemical shift difference between sites **a** and **b**. In this case the NMR lineshape becomes;

$$v = \frac{-\gamma B_1 \chi_a M_{zeq} T_{2a}^{-1}}{T_{2a}^{'-2} + (\omega_{0a} - \omega)^2} + \frac{-\gamma B_1 \chi_b M_{zeq} T_{2b}^{-1}}{T_{2b}^{'-2} + (\omega_{0b} - \omega)^2} \qquad \textbf{4.20}$$

where $T_{2a}^{'-2}$ and $T_{2b}^{'-2}$ are the observed transverse relaxation times of sites **a** and **b**;

$$T_{2a}^{'-1} = T_{2a}^{-1} + \tau_a^{-1} \text{ and } T_{2b}^{'-1} = T_{2b}^{-1} + \tau_b^{-1} \qquad \textbf{4.21}$$

Equation 4.20 once again describes two Lorentzian lineshapes centred at ω_{0a} and ω_{0b} but because the observed transverse relaxation times are shorter than T_{2a} and T_{2b}, the tranverse relaxation times characterising these sites in the absence of

exchange. The difference between $W_{1/2a}$, the full width at half maximum amplitude in the absence of exchange, and $W'_{1/2a}$, the corresponding width of the exchange broadened resonance can be used to estimate τ_a;

$$\pi W_{1/2a} = \frac{1}{T_{2a}} \qquad\qquad\qquad \textbf{4.22}$$

$$\pi W'_{1/2a} - \pi W_{1/2a} = \frac{1}{T'_{2a}} - \frac{1}{T_{2a}} = \frac{1}{\tau_a} \qquad \textbf{4.23}$$

For exchanging systems in the very slow exchange limit of the NMR time scale, Equation 4.23 may be used to provide an estimate of the lower limit of either τ_a or τ_b (hence an upper limit of k, the exchange rate constant) by calculating the lifetime which would cause a broadening of each resonance by 50%;
and so,

$$W'_{1/2a} = 1.5 W_{1/2a} \quad \tau_a = \frac{2}{\pi W_{1/2a}} \qquad \textbf{4.24}$$

A similar expression applies for τ_b.

4.2.1.2   Intermediate Rates of Exchange; Coalescence

From the slow exchange limit, the resonances characterising sites **a** and **b** broaden further and coalesce to form a single resonance when the lifetimes τ_a and τ_b are of the order of $(\omega_{0a} - \omega_{0b})^{-1}$. From this point, the fast exchange limit is experienced, with τ_a and τ_b decreasing further until the very fast exchange limit is met. If the restraints $\chi_a = \chi_b$ and $\tau_a = \tau_b$ are introduced and $\dfrac{1}{T_{2a}} = \dfrac{1}{T_{2b}} = 0$, then;

$$M_{za} = M_{zb} = \frac{1}{2} M_{zeq} \qquad\qquad \textbf{4.25}$$

Thus, the absorption mode lineshape becomes;

$$v = \frac{\frac{1}{2}\gamma B_1 M_{zeq} \tau_a (\omega_{0a} - \omega_{0b})^2}{(\omega_{0a} + \omega_{0b} - 2\omega)^2 + \tau_a^2 (\omega_{0a} - \omega)^2 (\omega_{0b} - \omega)^2} \qquad \textbf{4.26}$$

In frequency units ν(Hz) $(=\omega/2\pi)$

$$g(\nu) = \frac{2\tau_a(\nu_a - \nu_b)^2}{[\nu - \frac{1}{2}(\nu_a - \nu_b)]^2 + \pi^2\tau_a^2(\nu - \nu_a)^2(\nu - \nu_b)^2}$$　　　　**4.27**

Equation 4.27 can be simplified (ref) by expressing the absorption lineshape as a function of the dimensionless quantity $x = \frac{\Delta\nu}{\Delta}$, where $\Delta\nu - \frac{1}{2}(\nu_a + \nu_b)$, $q = \pi\tau_a\Delta$

and $\Delta = \frac{1}{2}(\nu_a - \nu_b)$;

$$g(x) = \frac{2\tau_a}{[x^2 + q^2(x^2 - 1)^2]}$$　　　　**4.28**

The lineshapes predicted by Equation 4.28 are identical to those derived from Equation 4.17 (with $\chi_a = \chi_b$). For $q \gg 1$ (slow exchange), Equation 4.28 predicts two Lorentzian signals centred at ν_a and ν_b. As q decreases (τ_a decreases), the two signals broaden and their maxima draw closer together until $q = \frac{1}{\sqrt{2}}$, where the two resonances coalesce to form a single broad signal with maximum amplitude at the mean of the frequency of the individual resonances $\frac{1}{2}(\nu_a + \nu_b)$. For conditions of faster exchange (where fast exchange has $q \ll 1$), Equation 4.28 predicts that the single broad resonance centred at $\frac{1}{2}(\nu_a + \nu_b)$ narrows further until the fast exchange limit is reached.

Thus, for systems undergoing chemical exchange, an estimate of the lifetime of the exchanging species $\tau_a = \tau_b$, may be calculated at the coalescence temperature, where the two resonances of the spectrum coalesce into a single broad resonance;

At coalescence;

$$q = \frac{1}{\sqrt{2}} \text{ and } \tau_a = \tau_b = \frac{\sqrt{2}}{\pi(v_a - v_b)}$$ **4.29**

If the chemical shifts characterising sites **a** and **b** in the absence of exchange (va and vb) are known, then an approximate value of τ_a may be calculated using Equation 4.29. This method was used to determine approximate values of τ_c at coalescence temperature), the mean lifetime (τ_a) of sites **a** and **b** at the coalescence temperature.

4.2.1.3   Fast Exchange

Very Fast Exchange Limit;

Under these conditions;

$$\tau_a^{-1}, \tau_b^{-1} \gg |\omega_{0a} - \omega_{0b}|, T_{2a}^{-1}, T_{2b}^{-1}$$

Here, the two broadened resonances centred at ω_{0a} and ω_{0b} have coalesced to form a single Lorentzian resonance centred at $\omega = \chi_a \omega_{0a} + \chi_b \omega_{0b}$ (the population weighted mean of the individual resonances ω_{0a} and ω_{0b}) and with linewidth also the weighted average of the individual resonances in the absence of exchange;

$$W_{1/2} = \frac{1}{\pi T_{2a}} + \frac{\chi_b}{\pi T_{2b}}$$ **4.30**

The absorption mode lineshape is given by;

$$v = \frac{-\gamma B_1 M_{zeq} T'_2}{1 + (T'_2)^2 (\chi_b \omega_{0b} - \omega)^2}$$ **4.31**

where
$$\frac{1}{T'_2} = \frac{\chi_a}{\pi T'_{2a}} + \frac{\chi_b}{T_{2b}}$$
4.32

As in the very slow exchange limit, Equation 4.31 contains no exchange information; the rate of exchange is so fast that the exchanging nuclear spins experience the weighted average of the environments **a** and **b**. If the rate of exchange is slightly slower ($\tau_a^{-1}, \tau_b^{-1} > |\omega_{0a} - \omega_{0b}|$; the fast exchange limit) then a single Lorentzian lineshape centred at $\omega = \chi_a \omega_{0a} + \chi_b \omega_{0b}$ is observed but the linewidth $W'_{1/2}$ will be greater than that given in Equation 4.29;

$$\frac{1}{T'_2} = \frac{\chi_a}{T_{2a}} + \frac{\chi_b}{T_{2b}} + \chi_a^2 \chi_b^2 (\omega_{0a} - \omega_{0b})^2 (\tau_a + \tau_b)$$
4.33

$$\pi W'_{1/2} = \pi \chi_a W_{1/2a} + \pi \chi_b W_{1/2b} + \chi_a^2 \chi_b^2 \Delta \omega_0^2 (\tau_a + \tau_b)$$
4.34

where $\Delta \omega_0 = |\omega_{0a} - \omega_{0b}|$

In frequency units ν(Hz) $(=\omega/2\pi)$;

$$\pi W'_{1/2} = \pi \chi_a W_{1/2a} + \pi \chi_b W_{1/2b} + 4\pi^2 \chi_a^2 \chi_b^2 \Delta \nu_0^2 (\tau_a + \tau_b \tau)$$
4.35

If the linewidths, $W_{1/2a}$ and $W_{1/2b}$, and the chemical shift difference, $\Delta \nu_0$, of the two resonances in the absence of exchange are known, then τ_a (and τ_b) may be determined from Equation 4.35 and the relationship; $\frac{\tau_a}{\chi_a} = \frac{\tau_b}{\chi_b}$.

4.2.2 Pulsed Fourier Transform NMR

Under pulsed NMR conditions (in the rotating frame (x', y', z')), B_0 is still applied continuously along the z' axis but now B_1 is applied along the x' axis in a high intensity pulse of short duration (10^{-6}-10^{-4}s), whose frequency is centred about ω_0. This applies torque to M, causing it to rotate towards the y' axis (about x') hence

generating a transverse component of M; M_{xy}. Immediately after the cessation of the pulse ($B_1 = 0$), spin lattice relaxation causes M to relax back to its equilibrium position aligned along the z' axis. Transverse relaxation causes the transverse component of M, M_{xy}, to decay to zero, generating a free induction decay signal (FID). By setting $B_1 = 0$, the modified Bloch equations may be solved to give an equation describing the FID;

$$M_{xy} = C_1 e^{-\phi + t} + C_2 e^{-\phi - t} \qquad\qquad \textbf{4.36}$$

where C_1 and C_2 are constants of integration and;

$$2\phi\pm = \left(\alpha_a + \frac{1}{\tau_a} + \alpha_b + \frac{1}{\tau_b} \right) \pm \left[\left(\alpha_a + \frac{1}{\tau_a} - \alpha_b - \frac{1}{\tau_b} \right)^2 + \frac{4}{\tau_a \tau_b} \right]^{1/2} \qquad \textbf{4.37}$$

The Fourier transform of the FID, S, is given by;

$$S = \int_0^\infty M_{zeq} e^{-i(\omega - \omega_1)t} dt \qquad\qquad \textbf{4.38}$$

$$= \frac{iM_{zeq}(\tau_a + \tau_b + \tau_a \tau_b (\alpha_a \chi_a + \alpha_b \chi_b))}{(1 + \alpha_a \tau_a)(1 + \alpha_b \tau_b)^{-1}} \qquad\qquad \textbf{4.39}$$

where; $\alpha_a = \dfrac{1}{T_{2a}} + i(\omega_{0a} - \omega)$

$\alpha_b = \dfrac{1}{T_{2b}} + i(\omega_{0b} - \omega)$

ω = the variable frequency

ω_1 = the fixed pulse carrier frequency

The absorption mode lineshape is derived from the imaginary part of Equation 4.3 and is the same as that derived from the continuous wave slow passage case (Equation 4.17). In general, the lineshape obtained for a pulsed Fourier transform experiment for an uncoupled spin system undergoing chemical exchange is

equivalent to that obtained under continuous wave slow passage conditions. All systems undergoing chemical exchange in this study fall into this category.

4.2.3 Lineshape Analysis

For two site uncoupled intermolecular exchange or intramolecular exchange, a theoretical NMR spectrum was generated using the non-interactive FORTRAN-77 program LINSHP[18] using the following input parameters;

- ν_a and ν_b, the frequency (Hz) of the two coalescing resonances characterising sites **a** and **b** in the absence of exchange

- $W_{1/2a}$ and $W_{1/2b}$, the full width at half maximum amplitude of each resonance in the absence of exchange

- χ_a and χ_b, the relative populations (mole fraction) of each site and R, the estimate rate exchange

- and $R = (\tau_a \chi_b)^{-1} = (\tau_b \chi_a)^{-1}$

The frequencies (ν_a and ν_b) and linewidths ($W_{1/2a}$ and $W_{1/2b}$) of the two site resonances in the absence of exchange must be found accurately over the temperature range over which the NMR measurements of the exchange process are carried out. Thus, the variations in these were determined by extrapolation from data in the very slow exchange region.

The intra or intermolecular exchange rate constant, k, was determined at each temperature by complete lineshape analysis of the corresponding experimental spectrum. The theoretical spectrum created by LINSHP was calculated from the value of R that minimised the residuals of the fit between the theoretical and experimental spectra. Both theoretical spectra and experimental were displayed simultaneously for comparison.

4.2.4 Calculation of Activation Parameters

The variation of the exchange rate constant k with temperature is given by the Eyring equation of transition state theory;[19]

$$k = \frac{1}{\tau} = \frac{k_B T}{h} \exp\left(\frac{-\Delta H^{\ddagger}}{RT} + \frac{\Delta S^{\ddagger}}{R} \right)$$ **4.40**

where; k_B = Boltzman's constant ($1.38062 \times 10^{-23} JK^{-1}$)

h = Planck's constant ($6.62620 \times 10^{-34} Js$)

R = Gas constant ($8.31434 Jmol^{-1}K^{-1}$)

$\Delta H^{\ddagger}$ = enthalpy of activation ($Jmol^{-1}$)

$\Delta S^{\ddagger}$ = entropy of activation ($Jmol^{-1}K^{-1}$)

T = Temperature (K)

Equation 4.40 can also be expressed in a linear form;

$$\ln(T.\tau) = \frac{\Delta H^{\ddagger}}{RT} - \frac{\Delta S^{\ddagger}}{R} + \ln\left(\frac{h}{k_B} \right)$$ **4.41**

Thus, a linear plot of $\ln(T.\tau)$ against $\frac{1}{T}$ gives a straight line with a slope of $\frac{\Delta H^{\ddagger}}{R}$

and an intercept of $\left(\frac{-\Delta S^{\ddagger}}{R} + \ln\left(\frac{h}{k_B} \right) \right)$.

4.3   Diastereomeric Exchange of 1,4,7-Tris((2S)-hydroxypropyl)-1,4,7-triazacyclononane (S-thpc9) and its Lithium(I) and Sodium(I) Complexes

The Λ and Δ diastereomers of S-thpc9 and [M(S-thpc9)]$^+$ may be interconverted by a single inversion at each of three nitrogen centres of the macrocycle where there is no equivalence between carbons for each of the diastereomers. Thus, the Δ and Λ diastereomers of S-thpc9 and [M(S-thpc9)]$^+$ should be characterised by separate spectra each consisting of five resonances arising from five unique carbons, *a-e*, for each diastereomer.

The ^{13}C spectra of S-thpc9 (Figure 4.3), [Li(S-thpc9)]$^+$ (Figure 4.4) and [Na(S-thpc9)]$^+$ (Figure 4.5) in ^{12}C enriched ^{2}H$_4$ show only one set of peaks indicating the presence of only one of the Λ and Δ isomers in solution.
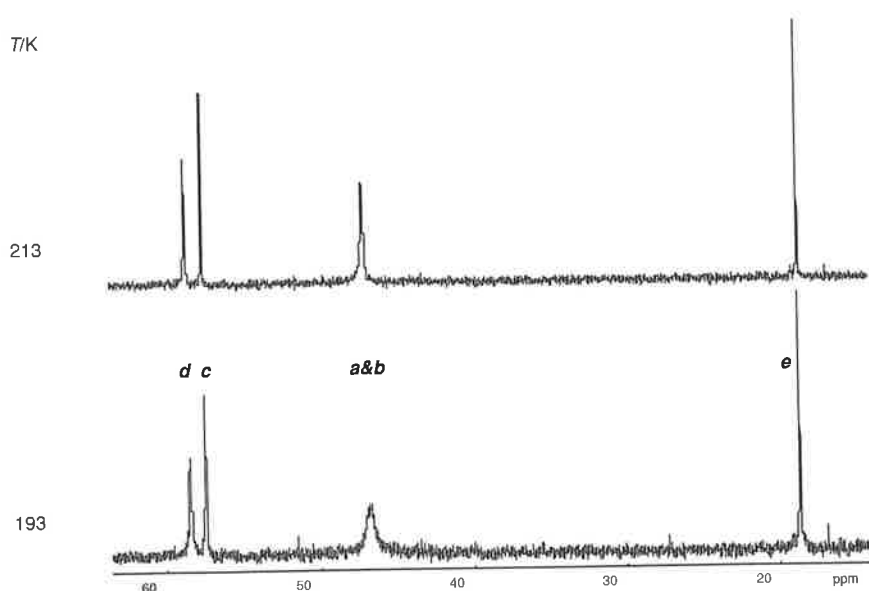
Figure 4.3 Temperature variations of ^{13}C spectra of S-thpc9 (0.1 mol dm^{-3}) in ^{12}C enriched ^{2}H$_4$ methanol at 75.47MHz. Experimental temperatures appear to the left of the figure.
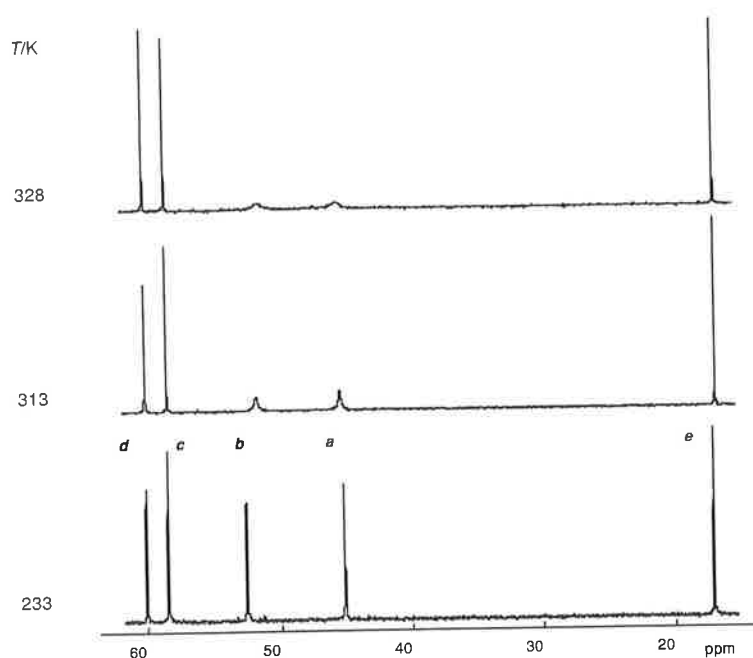
Figure 4.4 Temperature variations of ^{13}C spectra of $[Li(S\text{-thpc9})]^+$ $(0.1 \text{ mol dm}^{-3})$ in ^{12}C enriched $^2H_4$ methanol at 75.47MHz. Experimental temperatures appear to the left of the figure.
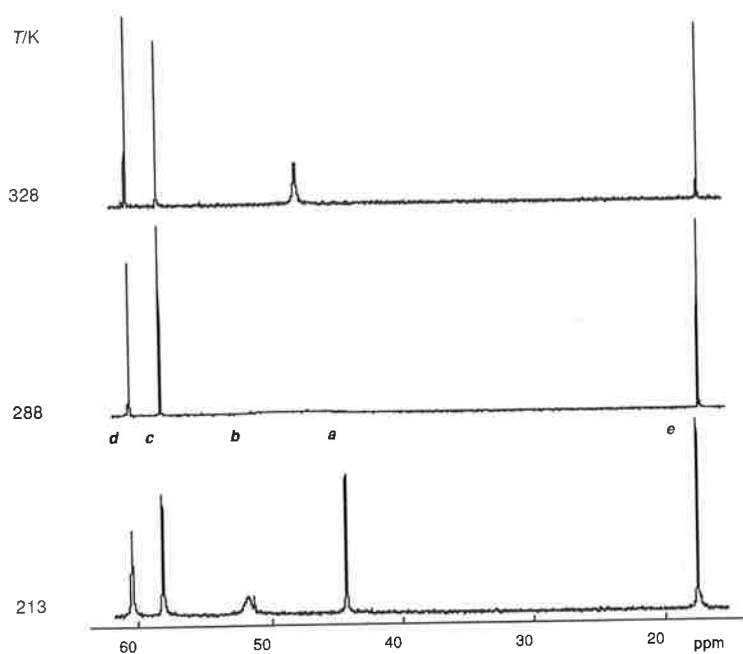
Figure 4.5 Temperature variations of ^{13}C spectra of $[Na(S\text{-thpc9})]^+$ $(0.1 \text{ mol dm}^{-3})$ in ^{12}C enriched $^2H_4$ methanol at 75.47MHz. Experimental temperatures appear to the left of the figure.

Gaussian 94 *ab initio* geometry optimisation calculations of *S*-thpc9 show the Δ diastereomer to be the lowest energy gas phase conformation. For the alkali and zinc metal complexes, the Λ complex was found to be of minimum energy. Further evidence of this can be seen in the X-ray crystal structure of Λ-[Zn(*S*-thpc9)]$^{2+}$ and is discussed in Chapter 2. A combination of the steric effects of the phenyl group and the nature of the metal ion govern this lowest energy conformation. As these are gas-phase calculations and do not take solvation effects into account, they do not provide conclusive evidence of the diastereomeric conformation in solution and so it remains speculative as to which particular diastereomer is dominant.

The variable temperature ^{13}C NMR spectra of [Li(*S*-thpc9)]$^{+}$ and [Na(*S*-thpc9)]$^{+}$, displayed in Figures 4.3 and 4.4, respectively, show two macrocyclic ring ^{13}C resonances, **a** and **b**, at low temperature which gradually broaden and eventually coalesce to a singlet with increasing temperature. No modifications of the ^{13}C resonances, **c** and **d**, assigned to the pendant arm carbons $-CH_2N-$ and $-OCH_2-$, occur apart from some narrowing as the temperature increases and viscosity decreases. This is consistent with a diastereomeric exchange process through a double inversion at the nitrogen centre causing macrocyclic ring carbon exchange between inequivalent environments **a** and **b**, while pendant arm carbons $-CH_2N-$ and $-OCH_2-$ exchange between equivalent environments (Figure 4.6). This double inversion process has also been observed for [Yb(*R*-DOTMA)]$^{-}$ (where DOTMA is 1,4,7,10-tetrakis((*R*)-methylacetato)-1,4,7,10-tetraazacyclo-dodecane)[20] and metal complexes of other chiral ligands such as *S*-thpc12[10, 21] and, more recently, *R*-thpec12.[7] This nitrogen double inversion has now been observed in the intramolecular exchange process of *S*-thpc9 as well as the other two ligands discussed later in this chapter (Figure 4.6).
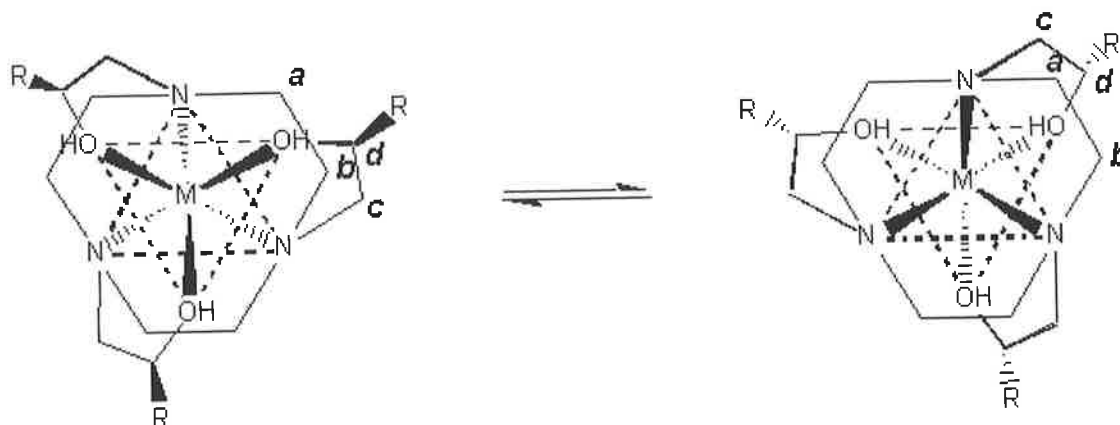
Fig 4.6 Exchange between equivalent diastereomeric conformations showing the double inversion at the three nitrogen centres where R = CH_3, C_6H_6 and $CH_2C_6H_6$ for S-thpc9, S-thpec9 and S-thppc9, respectively.

In the absence of a complexed metal ion, the intramolecular exchange processes of S-thpc9 are too rapid to be quantified on the NMR time scale. However, significant broadening of the coalesced resonance due to macrocyclic carbons **a** and **b** is a result of diastereomeric exchange occurring just within the fast exchange regime (Figure 4.3).

In comparison with the free ligand spectra of thec9, where no broadening was detected at low temperature, it appears the addition of the methyl substituent to the pendant arms of S-thpc9 has slowed the macrocyclic ring carbon exchange sufficiently so that it can just be detected on the NMR time scale at low temperature.

A complete lineshape analysis of the variable temperature spectra of [Li(S-thpc9)]$^+$ and [Na(S-thpc9)]$^+$ was carried out to afford the site lifetimes, τ, of macrocyclic ring carbons **a** and **b**, such that:

$$\frac{1}{\tau} = k = \frac{k_B T}{h \exp\left(\dfrac{-\Delta H^{\ddagger}}{RT} + \dfrac{\Delta S^{\ddagger}}{R}\right)} \qquad \textbf{4.41}$$

where k is the rate constant for interconversion between the two equivalent forms of the diastereomers of each complex.

The experimental spectra and theoretical lineshapes of the two resonances due to the macrocyclic ring carbons a and b of [Li(S-thpc9)]$^+$ and [Na(S-thpc9)]$^+$ are shown along with the derived site lifetimes in Figures 4.7 and 4.8, respectively. The derived τ values (ms) and the temperatures (K) in brackets are 4.17 (328.1), 5.75 (323.2), 7.81 (318.2), 10.16 (313.3), 15.02 (308.3), 21.51 (303.3), 31.25 (298.4) and 43.1 (292.3) for [Li(S-thpc9)]$^+$ and 0.23 (303.4), 0.41(293.1), 0.93 (287.1), 1.62 (276.8), 2.56 (271.6), 6.60 (261.3), 18.6 (250.9) and 59.5 (240.6) for [Na(S-thpc9)]$^+$.
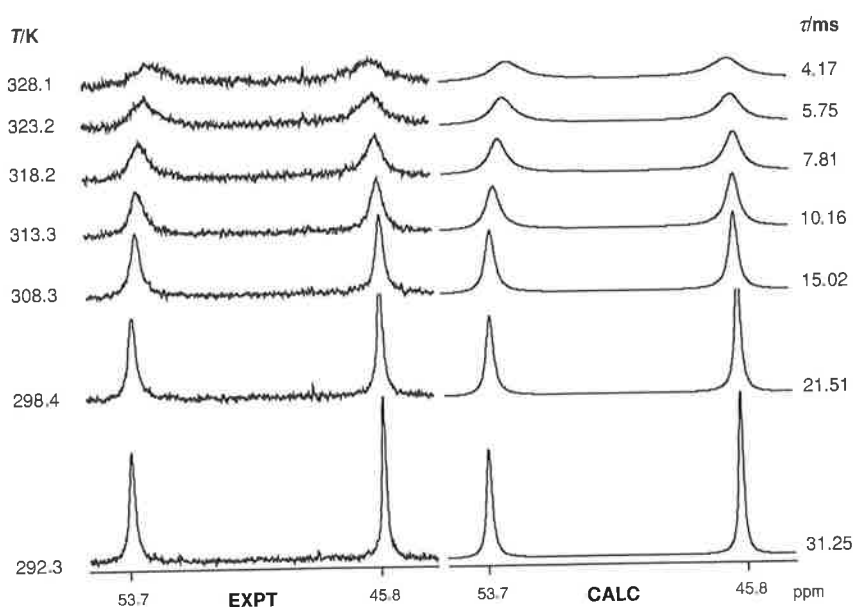
Figure 4.7 Temperature variations of the experimental and calculated ^{13}C spectra of [Li(S-thpc9)]$^+$ (0.1 mol dm^{-3}) in ^{12}C enriched $^2H_4$ methanol at 75.47MHz. Experimental temperatures and τ values derived from complete lineshape analysis of the coalescing doublet arising from the macrocyclic ring carbons, a and b, appear to the left and the right of the figure, respectively.
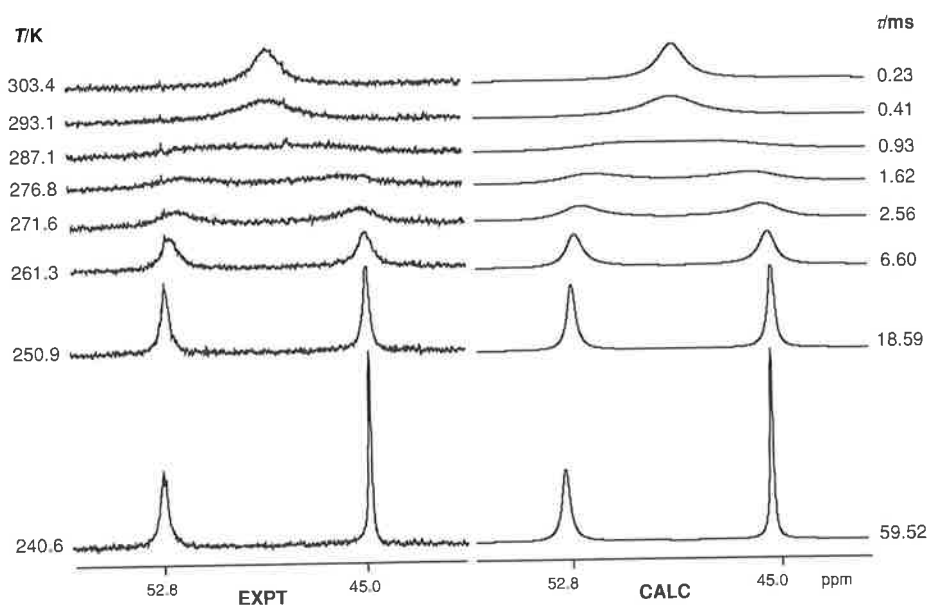
Figure 4.8 Temperature variations of the experimental and calculated ^{13}C spectra of $[Na(S\text{-thpc9})]^+$ (0.1 mol dm^{-3}) in ^{12}C enriched $^2H_4$ methanol at 75.47MHz. Experimental temperatures and τ values derived from complete lineshape analysis of the coalescing doublet arising from the macrocyclic ring carbons, **a** and **b**, appear to the left and the right of the figure, respectively.

The thermodynamic activation parameters of the diastereomeric exchange process of the lithium(I) and sodium(I) complexes of S-thpc9 are tabulated in Table 4 along with those of the enantiomeric exchange process of those complexes of thec9 for comparison.
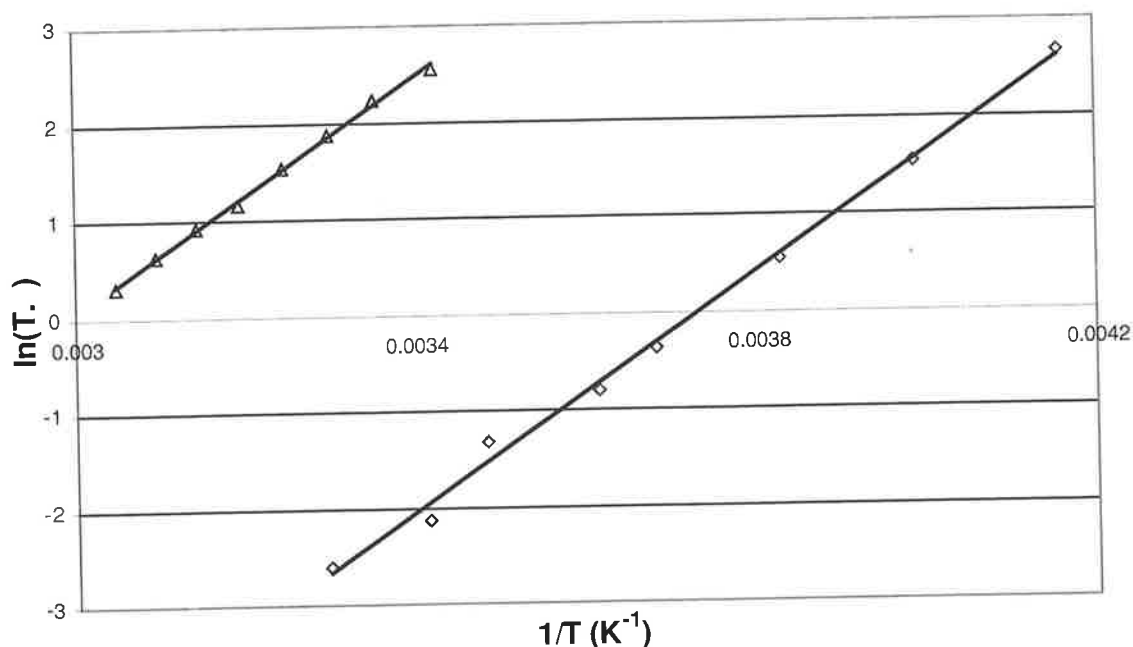
Figure 4.9   Temperature variations of τ for intramolecular diastereomeric exchange in ^{12}C enriched $^{2}H_4$ methanol of [Li(S-thpc9)]$^+$ ($\triangle$) and [Na(S-thpc9)]$^+$ ($\lozenge$). The solid lines represent the best fit of the data to Equation 4.41 for each system.

Table 4.1   Activation parameters for the enantiomeric and diastereomeric exchange processes in ^{12}C enriched $^{2}H_4$ methanol of the Li$^+$ and Na$^+$ complexes of thec9[16] and S-thpc9, respectively, at 0.1 mol dm^{-3}.

Ligand	Metal	$\Delta H^{\ddagger}$ (kJ mol^{-1})	$\Delta S^{\ddagger}$ (kJ mol^{-1} K^{-1})	$k_{298.2}$ (s^{-1})
thec9	Li$^+$	27.2	-36.3	1.11 x 10^6
	Na$^+$	21.7	69.6	2.27 x 10^5
S-thpc9	Li$^+$	50.6±1.0	-46.1±3.4	33.5±0.8
	Na$^+$	50.9±1.3	-7.6±4.7	3030±80

The rate of exchange for the lithium(I) complex of *S*-thpc9 is slower than that of its sodium(I) analogue, as indicated by the greater $k_{298.2}$. However, the variation of the magnitudes of $\Delta H^{\ddagger}$ and $\Delta S^{\ddagger}$ with the exchanging system gives greater insight into the factors controlling the rate of the exchange process at any temperature. The $\Delta H^{\ddagger}$ values are approximately the same within experimental error. The slower diastereomeric exchange of $[\text{Li}(S\text{-thpc9})]^{+}$ is reflected in the more negative value of $\Delta S^{\ddagger}$ which reflects substantial ordering in the transition state.

The rates of interchange at 298.2 K of macrocyclic carbons *a* and *b* for $[\text{Li}(S\text{-thpc9})]^{+}$ and $[\text{Na}(S\text{-thpc9})]^{+}$ are much slower than those determined for $[\text{Li}(\text{thec9})]^{+}$ and $[\text{Na}(\text{thec9})]^{+}$. The larger $\Delta H^{\ddagger}$ and more negative $\Delta S^{\ddagger}$ for $[\text{Li}(S\text{-thpc9})]^{+}$ and $[\text{Na}(S\text{-thpc9})]^{+}$ reflect this (Table 4.1). A possible explanation for this lies in the mechanism of the exchange process.

The much greater lability of $[\text{Li}(\text{thec9})]^{+}$ and $[\text{Na}(\text{thec9})]^{+}$ by comparison with their *S*-thpc9 analogues probably arises because the exchange process in the thec9 complex only involves a single inversion at each nitrogen (Figure 4.2), whereas the exchange process in the *S*-thpc9 complexes involves a double nitrogen inversion at each nitrogen (Figure 4.6). Thus, the metal centres of $[\text{Li}(\text{thec9})]^{+}$ and $[\text{Na}(\text{thec9})]^{+}$ need not move out from the between the trigonal oxygen and trigonal nitrogen planes of the complexes for the exchange process to occur. In contrast, the metal centres of $[\text{Li}(S\text{-thpc9})]^{+}$ and $[\text{Na}(S\text{-thpc9})]^{+}$ must move from one side of the trigonal nitrogen plane to the other in the proposed exchange process. Both lithium(I) and sodium(I) are too large to pass through the centre of the plane containing the three nitrogen atoms so that the double inversion requires the detachment of the metal centre from each of the oxygen and nitrogen donor atoms either in an intra- or intermolecular process. Although the detailed mechanism of the exchange process in neither set of complexes is fully understood, it appears that there is likely to be more steps and more bond breaking in the exchange process of the *S*-thpc9 complexes and that this is the origin of their relatively decreased lability.

Thermodynamically, the above differences in lability are reflected in $\Delta H^{\ddagger}$ for the thec9 system being less than half those for the *S*-thpc9 systems. This may reflect a greater degree of bond breaking in the latter system. The interpretation of the $\Delta S^{\ddagger}$ data is less certain.

In principle the exchange process in the thec9 system could occur through an intramolecular mechanism where sequential single nitrogen inversion occurred. Alternatively, an intermolecular process where the Li^+ and Na^+ ions dissociate from thec9 would produce the same NMR coalescence phenomena. Similarly, either an intra- or intermolecular mechanisms may operate for the *S*-thpc9 systems. However, because the proposed process leading to the NMR coalescence phenomena requires the Li^+ and Na^+ to move from one side of the trigonal plane to the other, a substantial amount of sequential bond breaking and bond making would be required if an intramolecular process operates. Similar arguments apply for the *S*-thpec9 and *S*-thppc9 systems discussed later.

The ^{13}C NMR of $[Zn(S\text{-}thpc9)]^{2+}$ in ^{12}C enriched $^{2}H_4$ methanol shows the two resonances due to macrocyclic carbons *a* and *b* completely resolved at room temperature. This decrease in lability of the zinc(II) complex when compared to those of the alkali metal ions is due to the increased charge density of zinc(II) so that it has a larger electrostatic attraction to the donor atoms of the ligand. In addition, as zinc(II) is a borderline-hard Lewis acid, it tends to form bonds with a more covalent nature. Similar results were found with the $[Zn(S\text{-}thpec9)]^+$ and $[Zn(S\text{-}thppc9)]^+$ discussed later.

4.4   Diastereomeric Exchange of 1,4,7-Tris((2*S*)-hydroxyphenyl-ethyl)-1,4,7-triazacyclononane (*S*-thpec9)

Due to the lack of solubility of *S*-thpec9 in methanol, the variable temperature NMR work was carried out in dimethylformamide.

The ^{13}C spectra of *S*-thpec9 (Figure 4.10), [Li(*S*-thpec9)]$^+$ (Figure 4.11) and [Na(*S*-thpec9)]$^+$ (Figure 4.12) in ^{2}H$_7$ dimethylformamide show only one set of peaks (eight resonances arising from eight unique carbons, *a-e*) indicating the presence of only one out of the Λ and Δ isomers to exist in solution.

Gaussian 94 *ab initio* geometry optimisation calculations afforded the Δ diastereomeric conformation of the free ligand and the Λ diastereomeric conformation of its alkali metal complexes. This is due to a combination of the steric effects of the phenyl group and the nature of the metal ion. As these calculations do not take solvation effects into account they do not provide conclusive evidence of the diastereomeric conformation in solution.
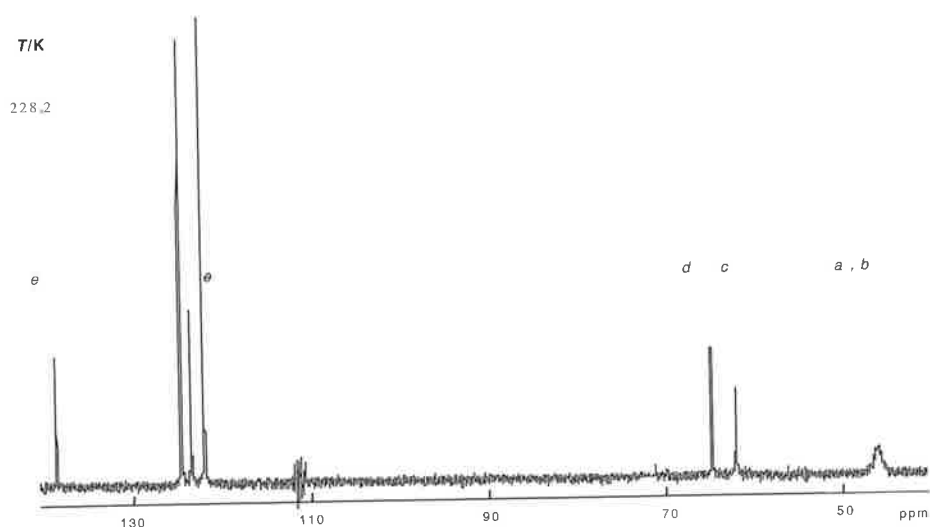
Figure 4.10   Low temperature ^{13}C NMR spectra of *S*-thpec9 in ^{2}H$_7$ dimethylformamide at 75.47 MHz.

In the free ligand spectra, the significant broadening and minor splitting of the coalesced resonance due to macrocyclic carbons *a* and *b* at low temperature is the result of diastereomeric exchange occurring just within the fast exchange regime (Figure 4.10).
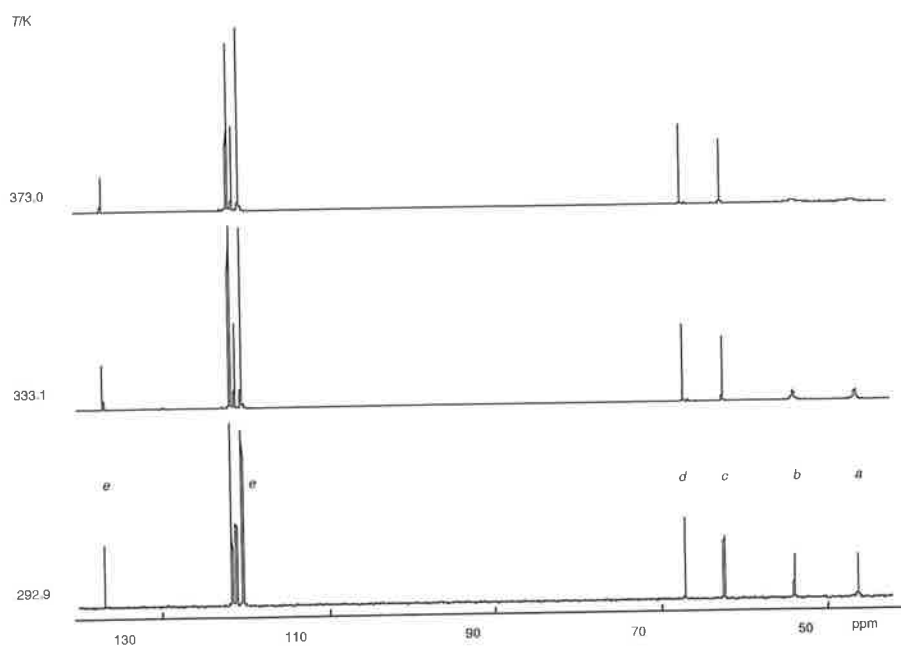
Figure 4.11 Temperature variations of ^{13}C spectra of [Li(S-thpec9)]$^+$ (0.1 mol dm^{-3}) in $^2H_7$ dimethylformamide at 75.47MHz. Experimental temperatures appear to the left of the figure. (All resonances in the spectra shown are singlets, although some may appear as mutiplets due to the diagram format).

The variable temperature ^{13}C NMR spectra of [Li(S-thpec9)]$^+$ [Na(S-thpec9)]$^+$, displayed in Figures 4.11 and 4.12, respectively, are again consistent with a double inversion at the nitrogen centre (Figure 4.6) causing macrocyclic ring carbon exchange between inequivalent environments *a* and *b*.
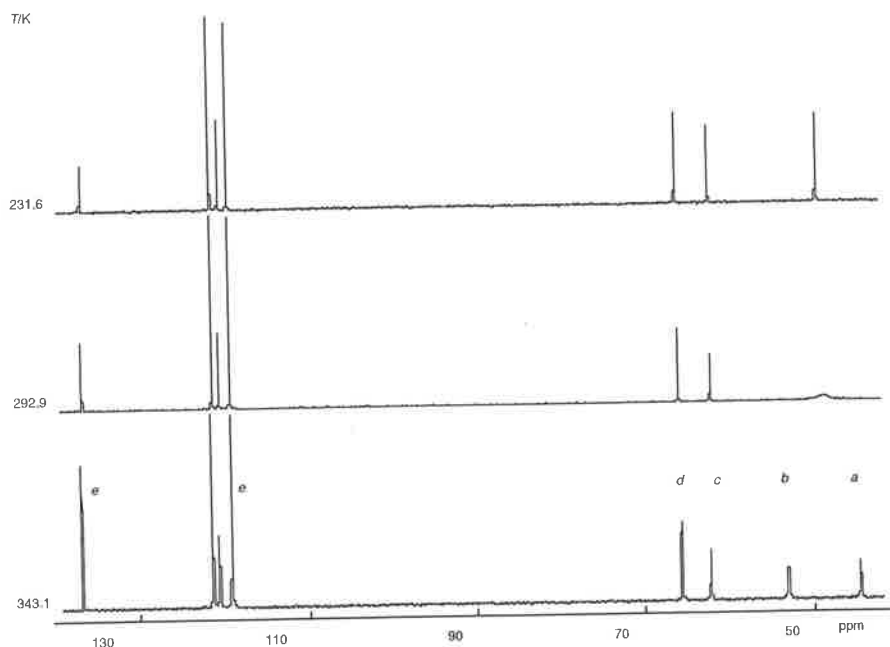
Figure 4.12 Temperature variations of ^{13}C spectra of [Na(S-thpec9)]$^+$ (0.1 mol dm^{-3}) in $^2H_7$ dimethylformamide at 75.47MHz. Experimental temperatures appear to the left of the figure. (All resonances in the spectra shown are singlets, although some may appear as mutiplets due to the diagram format).

A complete lineshape analysis of the variable temperature spectra of [Li(S-thpec9)]$^+$ and [Na(S-thpec9)]$^+$ was carried out to afford the site lifetimes of macrocyclic ring carbons **a** and **b**, and subsequently the thermodynamic activation parameters of the diastereomeric exchange process.

The experimental spectra and theoretical lineshapes of the two resonances due to the macrocyclic ring carbons **a** and **b** of [Li(S-thpec9)]$^+$ and [Na(S-thpec9)]$^+$ are shown along with the derived site lifetimes in Figures 4.13 and 4.14, respectively. The derived τ values (ms) and the temperature (K) in brackets are 3.80 (362.9), 4.40 (358.0), 5.23 (353.0), 6.39 (348.1). 7.82 (343.2), 8.63 (338.3) and 10.82 (333.4) for [Li(S-thpec9)]$^+$ and 8.25 (250.9), 3.39 (261.3), 1.91 (266.4), 1.07 (271.6), 0.67 (276.8), 0.42 (281.9), 0.16 (292.9) and 0.09 (303.3) for [Na(S-thpec9)]$^+$.
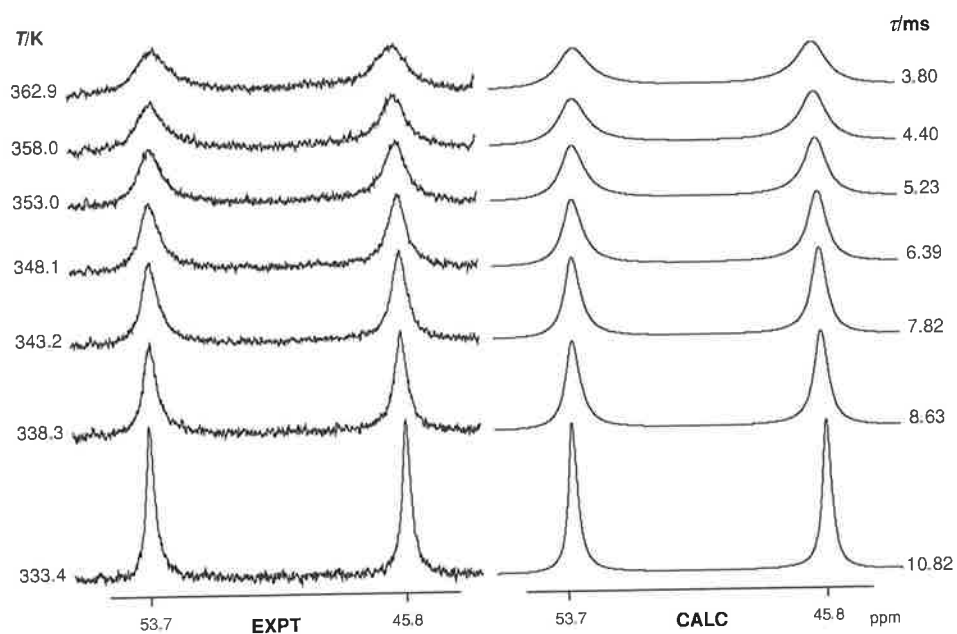
Figure 4.13 Temperature variations of the experimental and calculated ^{13}C spectra of [Li(S-thpec9)]$^+$ (0.1 mol dm^{-3}) in ^{2}H$_7$ dimethylformamide at 75.47 MHz. Experimental temperatures and τ values derived from complete lineshape analysis of coalescing doublet arising from the macrocyclic ring carbons, **a** and **b**, appear to the left and the right of the figure, respectively.
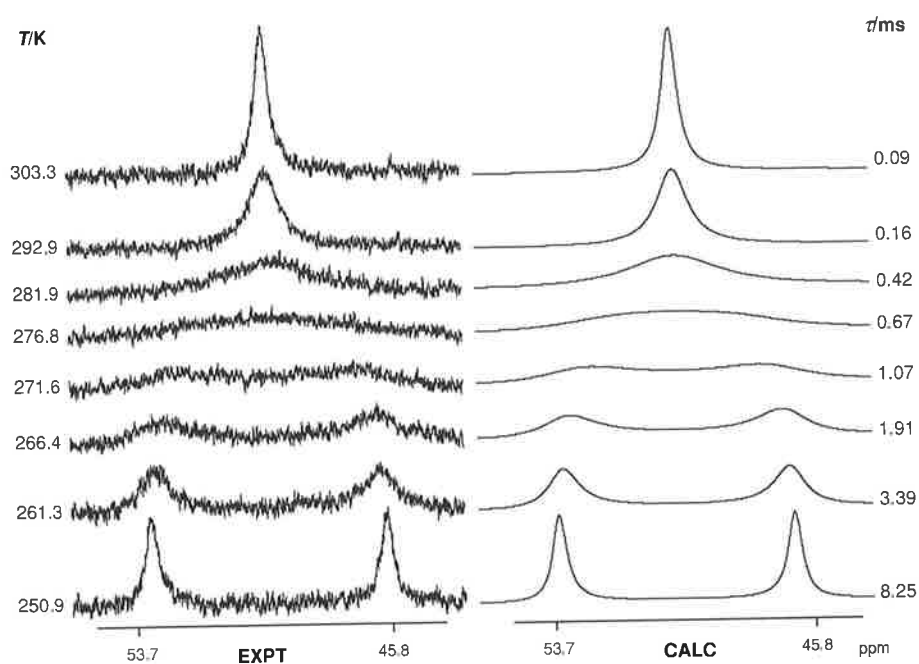
Figure 4.14 Temperature variations of the experimental and calculated ^{13}C spectra of [Na(S-thpec9)]$^+$ (0.1 mol dm^{-3}) in ^{2}H$_7$ dimethylformamide at 75.47MHz. Experimental temperatures and τ values derived from complete lineshape analysis of coalescing doublet arising from the macrocyclic ring carbons, *a* and *b*, appear to the left and the right of the figure, respectively.
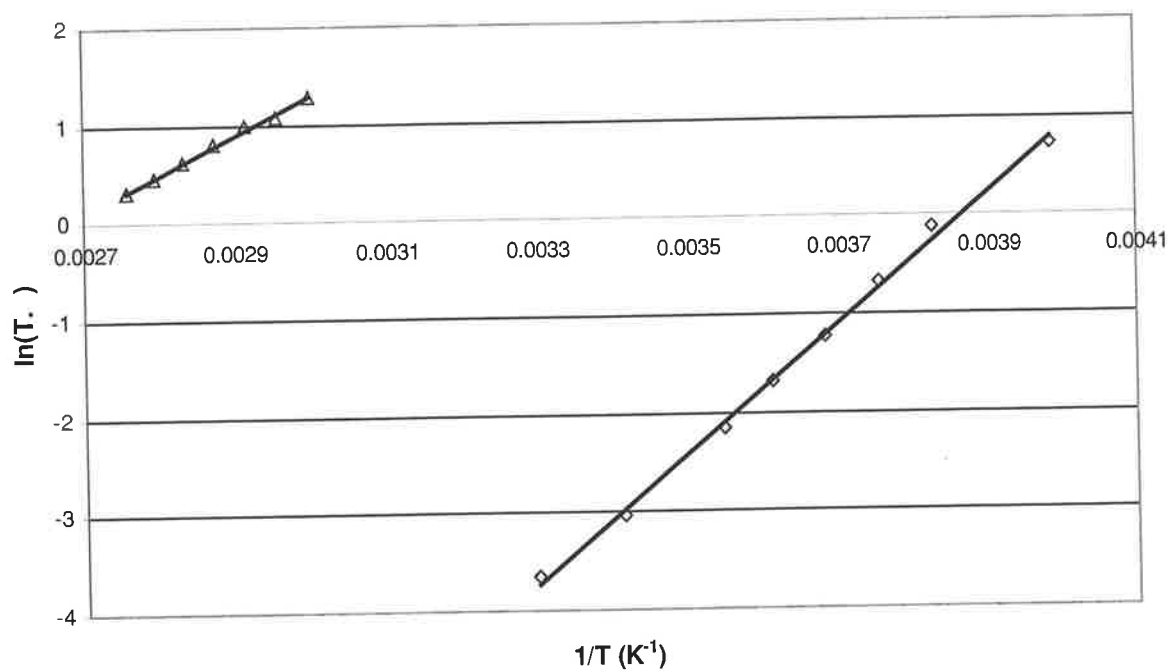
Figure 4.15   Temperature variations of τ for intramolecular diastereomeric exchange in $^2H_7$ dimethylformamide of [Li(S-thpec9)]$^+$ ($\triangle$) and [Na(S-thpec9)]$^+$ ($\Diamond$). The solid lines represent the best fit of the data to Equation 4.41 for each system.

Table 4.2 Activation parameters for the diastereomeric exchange process in $^2H_7$ dimethylformamide of the Li$^+$ and Na$^+$ complexes of S-thpec9 and R-thpec12[7] at 0.1 mol dm^{-3} concentration.

Ligand	Metal	$\Delta H^{\ddagger}$ (kJ mol^{-1})	$\Delta S^{\ddagger}$ (kJ mol^{-1} K^{-1})	$k_{298.2}$ (s^{-1})
S-thpec9	Li$^+$	32.8 ± 1.1	-110.0 ± 3.2	20.5 ± 0.8
	Na$^+$	54.7 ± 1.2	-7.56 ± 4.7	8600 ± 200
R-thpec12	-	46300 ± 1800	40.8 ± 0.4	18.8 ± 1.7
	Li$^+$	34.6 ± 0.3	-83.5 ± 1.1	233 ± 2
	Na$^+$	46.1 ± 0.2	-52.2 ± 0.7	98 ± 1

In the absence of a complexed metal ion, the diastereomeric exchange of S-thpec9 occurs only just within the slow exchange regime so that the peaks due to macrocyclic carbons *a* and *b* are not fully resolved at low temperature. This implies that the exchange process is much more rapid than that of its twelve-membered macrocyclic ring analogue for which the resonances due to macrocyclic ring carbons *a* and *b* are completely resolved at low temperature.[7]
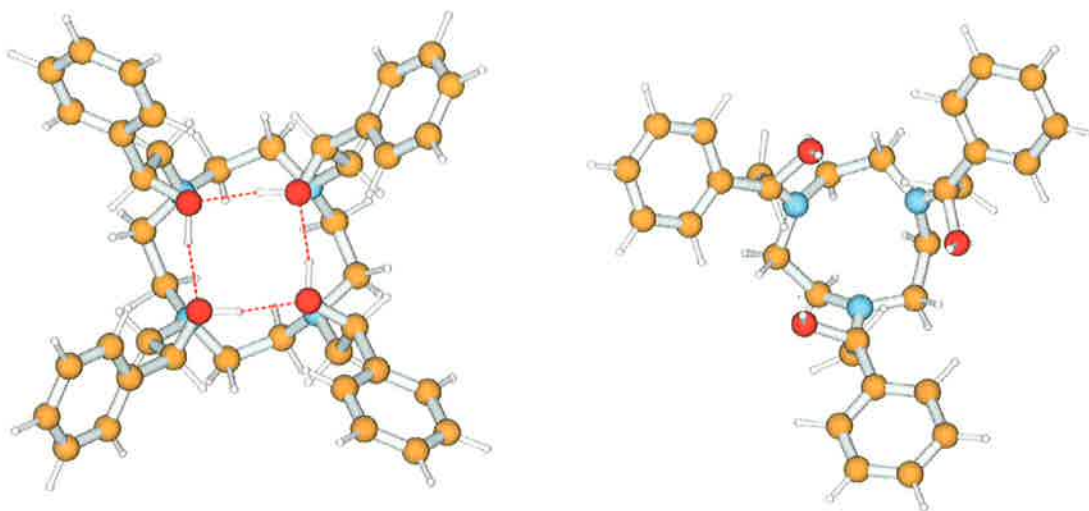
Figure 4.16 Minimum energy gas phase conformations of S-thpec12[7] (on the left) and S-thpec9 (on the right) viewed down the C_4 and C_3 axes, respectively, as determined by Gaussian94 geometry optimisation calculations using the LANL2DZ basis set.[22]

The gas phase geometry optimised structure of S-thpec12 shows the four hydroxyl groups to be hydrogen bonded to each other in a right handed fashion, whereas S-thpec9 shows no hydrogen bonding (Figure 4.16). It could be speculated that if this were the case in dimethylformamide, the diastereomeric exchange process for S-thpec12 (which is similar to that of R-thpec12) would be slowed relative to that of S-thpec9. However, this argument remains inconclusive, as there are no

solvation effects taken into account in the calculations. Alternatively, the slower diastereomeric exchange of *R*-thpec9 could be due to the double inversion of four nitrogens, as opposed to only three for *S*-thpec9, or it could be a combination of both of these effects.

The rate of exchange for the lithium(I) complex of *S*-thpec9 is slower than that of its sodium(I) analogue, as indicated by the greater $k_{298.2}$. This may also be reflected in the more negative value of $\Delta S^{\ddagger}$ for $[Li(S\text{-thpec9})]^{+}$ which indicates substantial ordering in the transition state.

The diastereomeric exchange of the lithium(I) and sodium(I) complexes of *S*-thpec9 involves a similar process to those of *S*-thpc9 and involves the translation of the metal centre from one side of the trigonal nitrogen plane to the other. The decreased lability of the lithium(I) and sodium(I) complexes of *R*-thpec12 is probably due to the double inversion of four nitrogens as opposed to three in the case of *S*-thpec9.

The ^{13}C NMR of $[Zn(S\text{-thpec9})]^{2+}$ in $^{2}H_{7}$ dimethylformamide shows the two resonances due to macrocyclic carbons *a* and *b* completely resolved at room temperature. This was as expected due to the tendency of zinc(II) to form less labile complexes than the alkali metal ions.

4.5 Diastereomeric Exchange of 1,4,7-Tris((2*S*)-hydroxy-3-phenylpropyl)-1,4,7-triazacyclononane (*S*-thppc9)

The variable temperature ^{13}C NMR study of *S*-thppc9 was carried out in dimethylformamide.

The ^{13}C spectra of *S*-thppc9 (Figure 4.21), [Li(*S*-thppc9)]$^+$ (Figure 4.22) and [Na(*S*-thppc9)]$^+$ (Figure 4.23) in $^2H_7$ dimethylformamide show only one set of resonances indicating the presence of only one out of the Λ and Δ isomers to exist in solution.
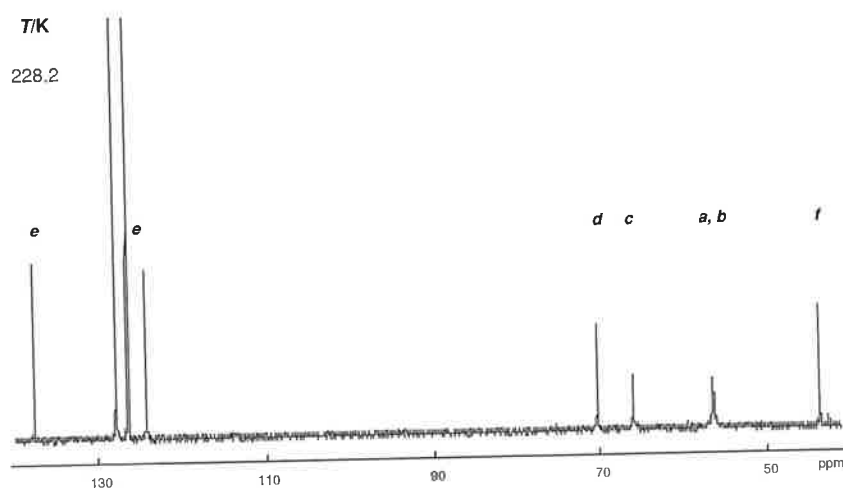
Figure 4.17 Low temperature ^{13}C NMR spectra of *S*-thppc9 in $^2H_7$ dimethylformamide at 75.47 MHz. All resonances shown here are singlets, although some may appear as multiplets due to the format of the diagram.

Gaussian 94 *ab initio* geometry optimisation calculations show the minimum energy conformation for the free ligand and its alkali metal complexes to adopt the Δ conformation. This is thought to be due to a combination of the steric effects of the benzyl group and the nature of the metal ion (see Chapter 2).

The low temperature spectrum of S-thppc9 shows a slight broadening of the coalesced resonance due to macrocyclic carbons **a** and **b** which is again, the result of diastereomeric exchange occurring just within the fast exchange regime (Figure 4.17).   The broadening is not as significant as that seen in the low temperature spectrum of S-thpec9 (Figure 4.10). This is consistent with a faster exchange rate of S-thppc9 when compared with S-thpec9 that is probably attributable to the greater flexibility of the pendant arms.

The variable temperature ^{13}C NMR spectra of [Li(S-thppc9)]$^+$ and [Na(S-thppc9)]$^+$, displayed in Figures 4.18 and 4.19, respectively, are again consistent with a double inversion at the nitrogen centre (Figure 4.6) causing macrocyclic ring carbon exchange between inequivalent environments **a** and **b**.
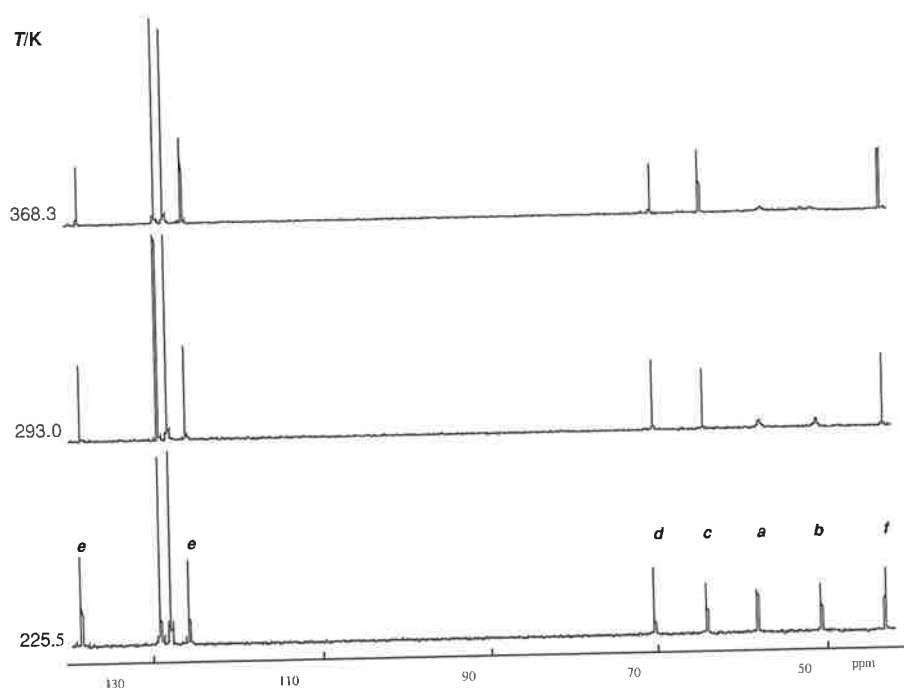
Figure 4.18 Temperature variations of ^{13}C spectra of [Li(S-thppc9)]$^+$ (0.1 mol dm^{-3}) in ^{2}H$_7$ dimethylformamide at 75.47 MHz. Experimental temperatures appear to the left of the figure. All resonances shown here are singlets, although some may appear as multiplets due to the format of the diagram
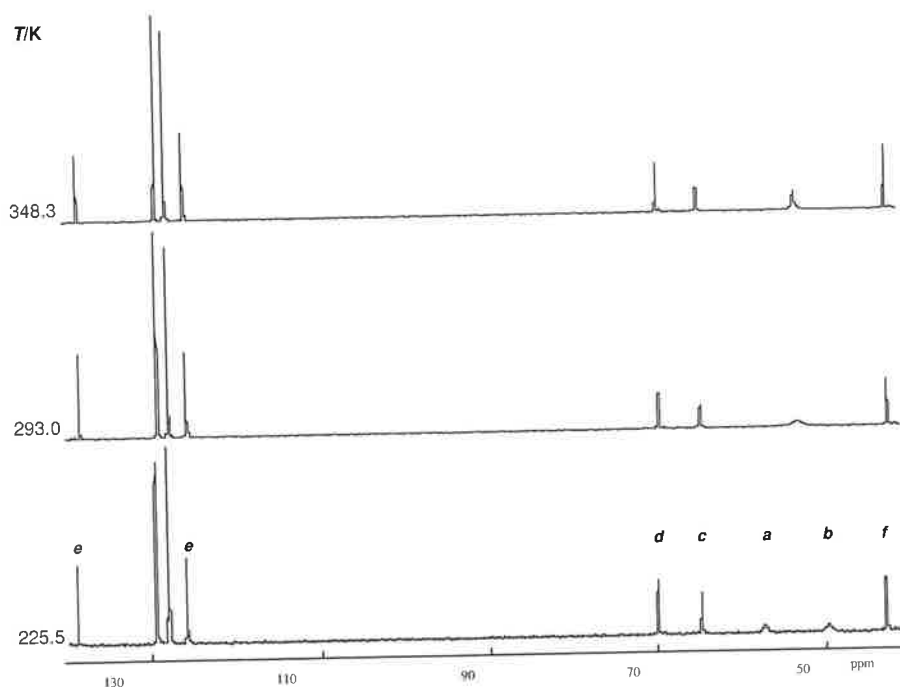
Figure 4.19 Temperature variations of ^{13}C spectra of [Na(S-thppc9)]$^+$ (0.1 mol dm^{-3}) in $^2H_7$ dimethylformamide at 75.47 MHz. Experimental temperatures appear to the left of the figure. All resonances shown here are singlets, although some may appear as multiplets due to the format of the diagram

A complete lineshape analysis of the variable temperature spectra of [Li(S-thppc9)]$^+$ and [Na(S-thppc9)]$^+$ was carried out to afford the site lifetimes of macrocyclic ring carbons **a** and **b**, and subsequently the activation parameters of the diastereomeric exchange process.

The experimental spectra and theoretical lineshapes of the two resonances due to the macrocyclic ring carbons **a** and **b** of [Li(S-thppc9)]$^+$ and [Na(S-thppc9)]$^+$ are shown along with the derived site lifetimes in Figures 4.20 and 4.21, respectively. The derived τ values (ms) and the temperatures (K) in brackets are 5.66 (323.6), 5.03 (328.5), 4.37 (333.4), 4.09 (338.3), 3.14 (343.2), 2.92 (348.2), 2.57 (353.1) and 2.37 (358.0) for [Li(S-thppc9)]$^+$ and 3.16 (225.5), 2.02 (230.1), 1.60 (235.9), 0.80 (246.3), 0.43 (256.7), 0.36 (261.8), 0.20 (272.2), 0.17 (277.4) and 0.14 (282.6) for [Na(S-thpec9)]$^+$.
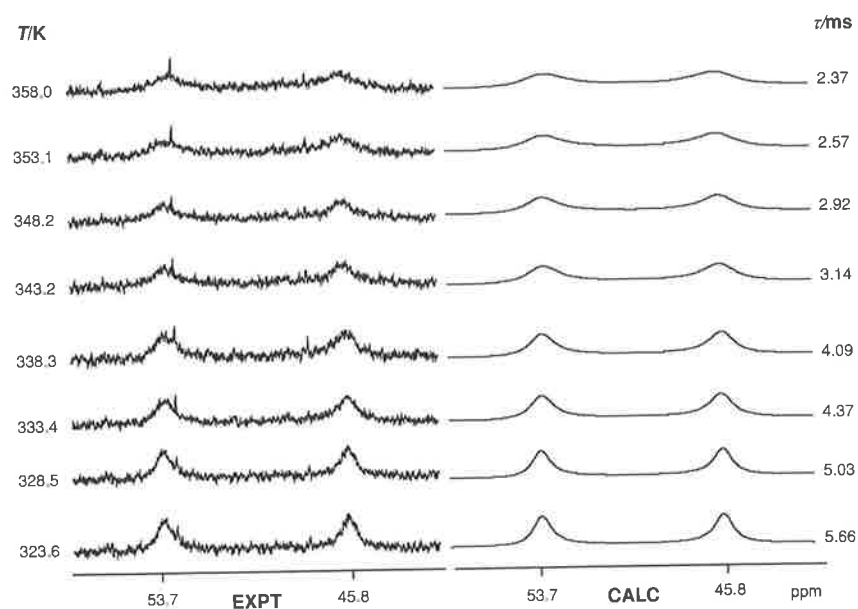
Figure 4.20 Temperature variations of the experimental and calculated ^{13}C spectra of [Li(S-thppc9)]$^+$ (0.1 mol dm^{-3}) in $^2H_7$ dimethylformamide at 75.47 MHz. Experimental temperatures and τ values derived from complete lineshape analysis of the coalescing doublet arising from the macrocyclic ring carbons, *a* and *b*, appear to the left and the right of the figure, respectively.
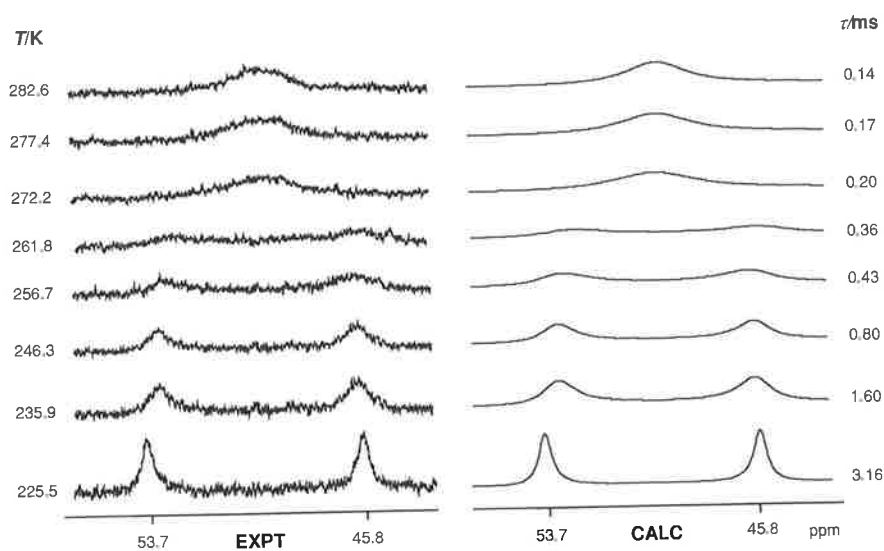
Figure 4.21 Temperature variations of the experimental and calculated ^{13}C spectra of [Na(S-thppc9)]$^+$ (0.1 mol dm^{-3}) in ^{2}H$_7$ dimethyformamide at 75.47 MHz. Experimental temperatures and τ values derived from complete lineshape analysis of the coalescing doublet arising from the macrocyclic ring carbons, **a** and **b**, appear to the left and the right of the figure, respectively.
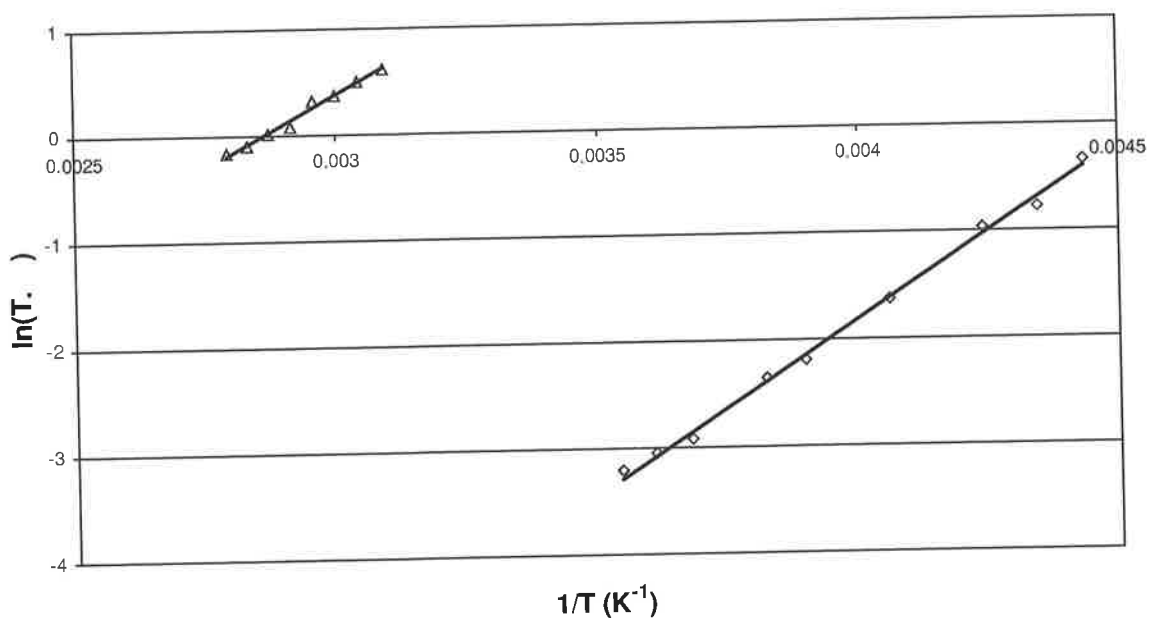
Figure 4.22 Temperature variations of τ for intramolecular diastereomeric exchange in $^2H_7$ dimethylformamide of $[Li(S\text{-thppc9})]^+$ ($\triangle$) and $[Na(S\text{-thppc9})]^+$ ($\diamondsuit$). The solid lines represent the best fit of the data to Equation 4.41 for each system.

Table 4.3 Activation parameters for the diastereomeric exchange processes in $^2H_7$ dimethylformamide of the Li^+ and Na^+ complexes of S-thpec9 and S-thppc9 at 0.1 mol dm^{-3} concentration.

Ligand	Metal	$\Delta H^\ddagger$ (kJ mol^{-1})	$\Delta S^\ddagger$ (kJ mol^{-1} K^{-1})	$k_{298.2}$ (s^{-1})
S-thpec9	-	-	-	-
	Li^+	32.8 ± 1.1	-110 ± 3	20.5 ± 0.8
	Na^+	54.7 ± 1.2	-7.6 ± 4.7	8600 ± 200
S-thppc9	-	-	-	-
	Li^+	22.5 ± 1.6	-133 ± 5	43 ± 5
	Na^+	33.8 ± 1.6	-59 ± 6	2980 ± 90

The rate of exchange for the lithium(I) complex of S-thppc9 is slower than that of its sodium(I) analogue, as indicated by the greater $k_{298.2}$. This may also be reflected in the more negative $\Delta S^{\ddagger}$ for the $[\text{Li}(S\text{-thppc9})]^{+}$ system that indicates substantial ordering in the transition state (Table 4.3).

At 298.2 K $[\text{Li}(S\text{-thppc9})]^{+}$ is more labile than is $[\text{Li}(S\text{-thpec9})]^{+}$ while $[\text{Na}(S\text{-thppc9})]^{+}$ is less labile than $[\text{Na}(S\text{-thpec9})]^{+}$. These differences in lability depend on the variation in magnitude of $\Delta G^{\ddagger}$ (= $\Delta H^{\ddagger}$ - T$\Delta S^{\ddagger}$) and it is seen that the relative labilities of the systems in Table 4.3 are temperature dependant.

The ^{13}C NMR of $[\text{Zn}(S\text{-thppc9})]^{2+}$ in ^{2}H$_7$ dimethylformamide shows the two resonances due to macrocyclic carbons **a** and **b** completely resolved at room temperature (similarly to that of $[\text{Zn}(S\text{-thpc9})]^{2+}$ and $[\text{Zn}(S\text{-thpec9})]^{2+}$). This was as expected due to the tendency of zinc(II) to form less labile complexes than the alkali metal ions.

References

1.   K. P. Wainwright, *Journal of the Chemical Society, Dalton Transactions*, 1980, 2117.

2.   R. W. Hay, M. P. Pujari, W. T. Moodie, S. Craig, D. T. Richens, A. Perotti and L. Ungaretti, *Journal of the Chemical Society, Dalton Transactions*, 1987, 2605.

3.   R. D. Hancock, R. Bhaven, P. W. Wade, J. C. A. Boyens and S. M. Dobson, *Inorganic Chemistry*, 1989. **28**, 187.

4.   C. M. Madeyski, J. P. Michael and R. D. Hancock, *Inorganic Chemistry*, 1984. **23**, 1487.

5.   J. M. Lehn and J. P. Sauvage, *Journal of the American Chemical Society*, 1975. **97**, 6700.

6.   P. Clarke, S. F. Lincoln and K. P. Wainwright, *Inorganic Chemistry*, 1990. **30**, 134.

7.   S. L. Whitbread, P. Valente, M. A. Buntine, P. Clements, S. F. Lincoln, M. R. Taylor and K. P. Wainwright, *Journal of the American Chemical Society*, 1998. **43**, 120.

8.   A. K. W. Stephens, R. S. Dhillon, S. E. Madbak, S. L. Whitbread and S. F. Lincoln, *Inorganic Chemistry*, 1996. **35**, 2019-2024.

9.   S. F. Lincoln, G. S. Laurence, P. A. Pittet, M. L. Turonek and K. P. Wainwright, *Journal of the Chemical Society, Chemical Communications*, 1991, 1205.

10.   R. Dhillon, S. E. Madbak, F. G. Ciccone, M. A. Buntine, S. F. Lincoln and K. P. Wainwright, *Journal of the American Chemical Society*, 1997. **119**, 6126.

11.   R. J. Day and C. N. Reilley, *Analytical Chemistry*, 1965. **37**, 1326.

12.   Y. Ba, R. F. Song and Z. W. Qiu, *Magnetic Resonance in Chemistry*, 1989. **27**, 916.

13.   P. Mirti, M. C. Genaro and M. Vallinotto, *Transition Metal Chemistry*, 1982. **2**, 2.

14.   M. C. Gennaro, P. Mirti and C. Casolino, *Polyhedron*, 1983. **2**, 13.

15.   L. M. Jackman and F. A. Cotton, *DNMR Spectroscopy*. 1975, London and New York: Academic Press.

16.   S. L. Whitbread, J. M. Weeks, P. Valente, M. A. Buntine, S. F. Lincoln and K. P. Wainwright, *Australian Journal of Chemistry*, 1997. **50**, 853.

17.   F. Bloch, *Physical Chemistry Reviews*, 1946. **70**, 460.

18.   P. Clarke, LINSHP; a Fortran-77 Program, *Ph.D Thesis*. 1992, University of Adelaide: Adelaide.

19.   S. Gladstone, K. J. Laidler and H. Eyring, *Theory of Rate Processes*. 1941, New York: McGraw-Hill.

20.   H. G. Brittain and J. F. Desreux, *Inorganic Chemistry*, 1984. **23**, 4459.

21.   R. S. Dhillon, A. K. W. Stephens, S. L. Whitbread, S. F. Lincoln and K. P. Wainwright., *Journal of the Chemical Society, Chemical Communications*, 1995. **1**, 97.

22.   M. J. Frisch, G. W. Trucks, H. B. Schlegel, P. M. w. Gill, B. G. Johnson, M. A. Robb, J. R. Cheeseman, G. A. P. T. Keith, J. A. Mongomery, K. Raghavachari, M. A. Al-Laham, V. G. Ortiz., J. B. Foresman, J. Ciolowski, B. B. Stefanov, A. Nanayakkara, M. Challacombe, C. Y. Peng, P. Y. Ayala, W. Chen, M. W. Wong, J. L. Andres, E. Replogle, R. Gomperts, R. L. Martin, D. J. Fox, J. S. Binkly, D. J. Defrees, J. Baker, J. P. Stewart, M. Head-Gordon, C. Gonzalez and J. A. Polple, *Gaussian 94, Revision D.3,* . 1994.

CHAPTER 5

Host-guest
Complexation
Studies

5.1   General introduction

The structural, kinetic and equilibrium studies of the three pendant arm donor triaza macrocyclic ligands, 1,4,7-tris-((2S)-hydroxypropyl)-1,4,7-triazacyclononane, *S*-thpc9, 1,4,7-tris-((2S)-hydroxyphenylethyl)-1,4,7-triazacyclononane, *S*-thpec9, 1,4,7-tris-((2S)-hydroxy-3-phenylpropyl)-1,4,7-triazacyclononane, *S*-thppc9, and their alkali metal and zinc(II) complexes, have been discussed in this thesis through *ab initio* molecular modeling, X-ray crystallographic studies, potentiometric stability constant determination and NMR kinetic studies. This has provided conclusive evidence of the formation of one preferred diastereomeric conformation in the gas-phase and in solution. The X-ray crystal structure of $[Zn(S\text{-thpc9})]^{2+}$ shows the complex to assume one diastereomeric conformation in the solid-phase.

When the chiral pendant arms carry an aromatic substrate in addition to a donor group, the possibility arises of using the coordination of a metal ion as a way of assembling a molecular receptor with a substantial cavity that arises from the juxtaposition of the aromatic groups (Equation 5.1).

$$M^{m+} + \text{ligand} + \text{guest} \rightleftharpoons [M(\text{ligand})]^{m+} + \text{guest} \rightleftharpoons [M(\text{ligand})(\text{guest})]^{m+} \qquad \textbf{5.1}$$
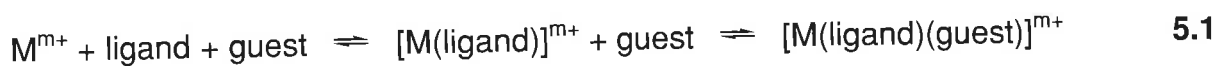
Molecular modeling shows the aromatic groups of the alkali metal and zinc(II) complexes of S-thpec9 and S-thppc9 form a molecular cavity with C_3 symmetry. The complexes of S-thpec9 form a saucer-shaped receptor cavity where S-thppc9 forms a deeper bowl-shaped receptor cavity.

As mentioned in the introduction (Chapter 1), host-guest complexation should be optimal when the symmetry of the guest is similar to that of the receptor. The additional electrostatic attraction of an anionic guest by the overall positive charge of the complex should favour entry into the receptor cavity. Preliminary host-guest complexation studies of [M(S-thpec9]$^{m+}$ and [M(S-thppc9)]$^{m+}$ have been explored with the guest molecules: tetraphenylborate ([B(C$_6$H$_5$)$_4$]$^-$) (pseudo C_3 symmetry), adamantane carboxylate (C$_{10}$H$_{15}$CO$_2$Na) (psuedo C_3 symmetry) and p-nitrophenol (NO$_2$C$_6$H$_4$OH) (C_{2v} symmetry).

5.2 Molecular modeling of a host-guest complex

Molecular modeling has been used here to predict the adopted conformation of a host-guest complex with [Na(S-thpec9)]$^+$ (host) and [(B(C$_6$H$_5$)$_4$]$^-$ (guest) (Figures 5.1 and 5.2). In the Gaussian 94 *ab initio* geometry optimised structure of the ternary complex, Na(S-thpec9)(B(C$_6$H$_5$)$_4$), the C_3 axes of [Na(S-thpec9)]$^+$ and the pseudo C_3 axis of [B(C$_6$H$_5$)$_4$]$^-$ are aligned such that their phenyl groups are arranged in a staggered fashion.

The phenyl groups of the [B(C$_6$H$_5$)$_4$]$^-$ and the phenyl groups of the [Na(S-thpec9)]$^+$ are offset by a centroid to centroid distance of approximately 6Å and are at an angle of approximately 180° to each other. According to the Hunter and Saunders model, these conditions result in a favourable π–π interaction.[1]
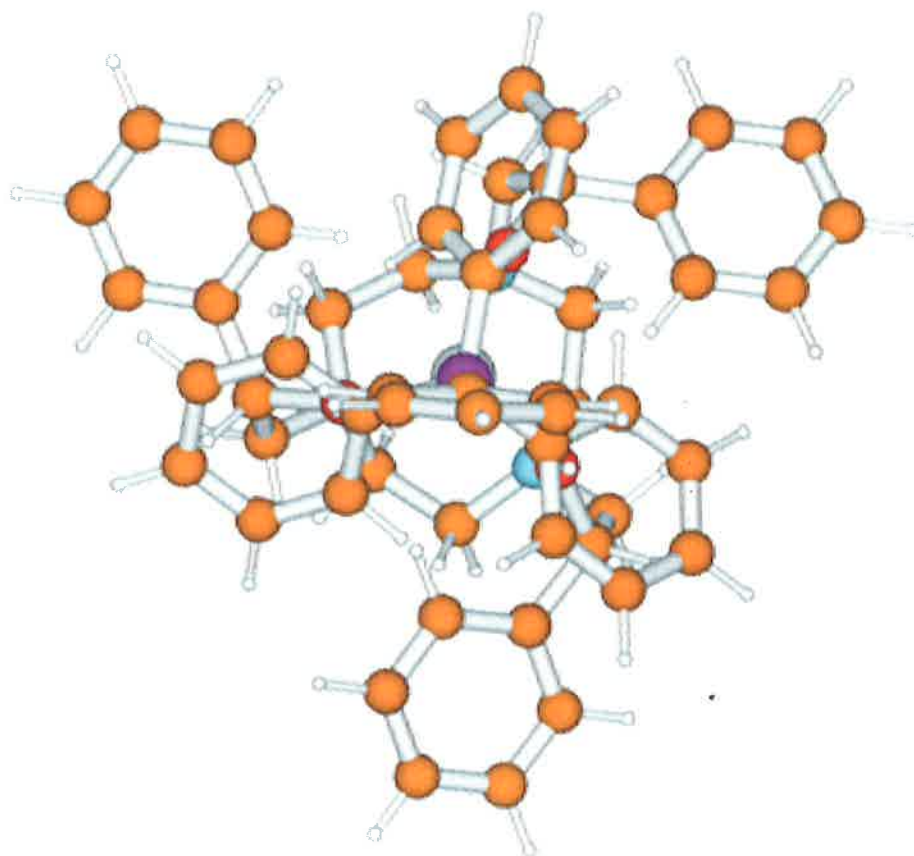
Figure 5.1   A view down the pseudo C_3 axis of the Gaussian 94 6-31G geometry optimised structure of [Na(S-thpec9)(B(C_6H_5)$_4$)].
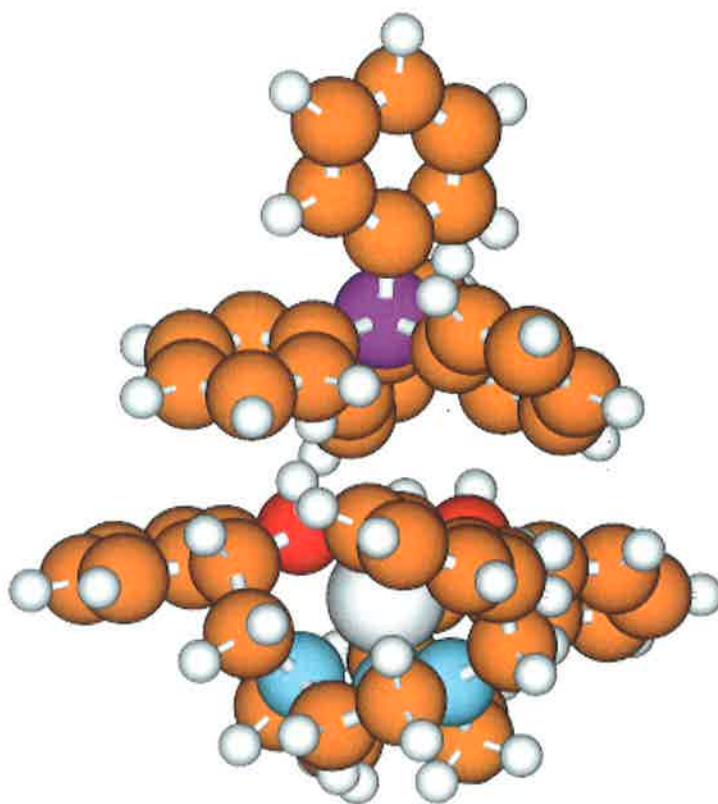
Figure 5.2 A view perpendicular to the pseudo C_3 axis of the space filling diagram of the Gaussian 94 6-31G geometry optimised structure of [Na(S-thpec9)(B(C_6H_5)$_4$)].

Table 5.1   Geometry of the Gaussian 94[2] 6-31G geometry optimised structure of Na(S-thpec9)(B(C_6H_5)$_4$).

Complex	O-O (Å)	N-N (Å)	O_{plane}-N_{plane} (Å)	Na-O_{plane} (Å)	Na-N_{plane} (Å)	Twist Angle (°)	Na-B (Å)
Na(S-thpec9)(B(C_6H_5)$_4$)	3.32	2.98	2.85	1.15	1.66	-3.0	5.51

5.3 ^{13}C NMR and ROESY NMR spectra

Preliminary host-guest interaction studies involved a comparison of the ^{13}C NMR spectra of [Na(S-thpec9)]$^+$ (cationic host) and NaB(C_6H_5)$_4$ (anionic guest) in $^2H_7$ dimethylformamide both separately and together.   No chemical shift change was observed for the resonances arising from either species.

It was anticipated that the complexation of zinc(II) in place of sodium(I) could potentially increase the interaction of host and guest due to its increased electrostatic attraction for the anionic guest.   Significant shifts of the ^{13}C NMR resonances of the [Zn(S-thpec9)]$^{2+}$ in the presence of equimolar NaB(C_6H_5)$_4$ in $^2H_7$ dimethylformamide were observed when compared with those of [Zn(S-thpec9)]$^{2+}$ alone (Figure 5.3). This is consistent with the occurrence of some interaction between [Zn(S-thpec9)]$^{2+}$ and [B(C_6H_5)$_4$]$^-$.   There were no shifts of the ^{13}C resonances of the [B(C_6H_5)$_4$]$^-$.   This is consistent with the [Zn(S-thpec9)]$^{2+}$ having a greater flexibility than the [B(C_6H_5)$_4$]$^-$ and changing its conformation to accommodate for it.   This prompted further investigations through ROESY NMR studies.
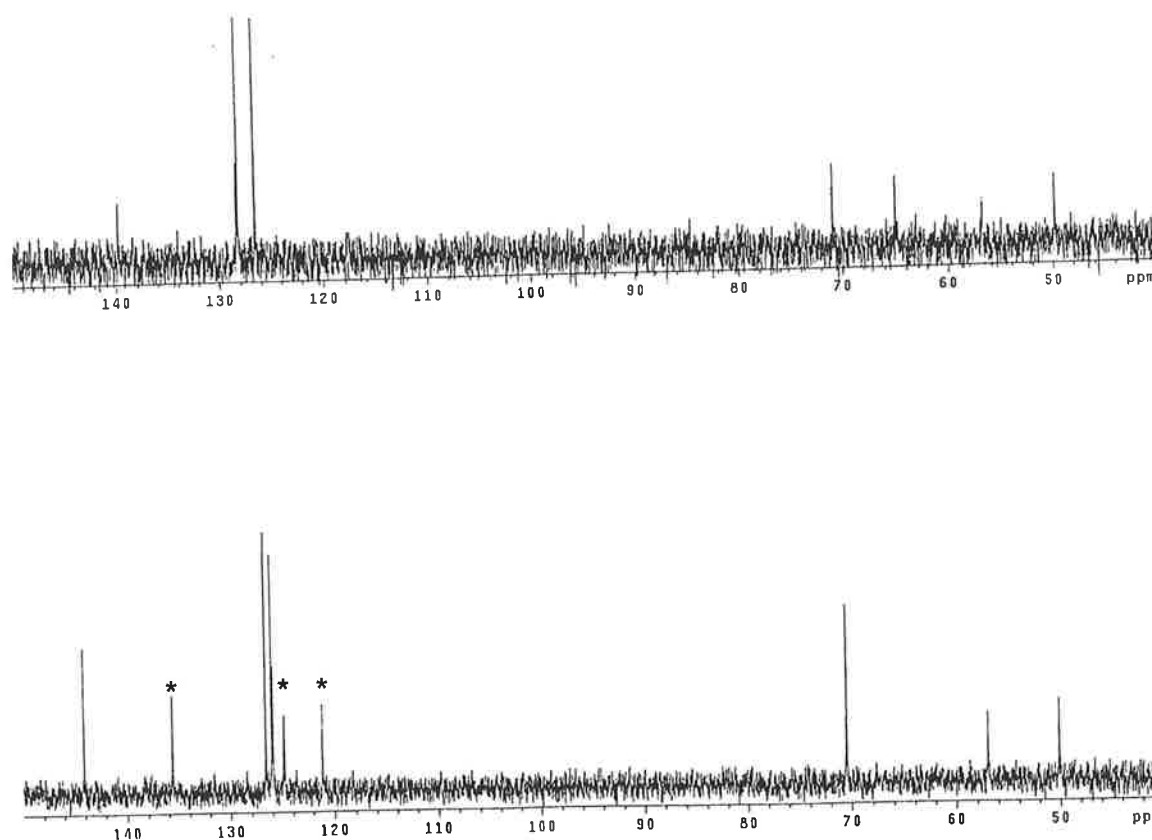
Figure 5.3 The ^{13}C NMR spectra of [Zn(S-thpec9)](ClO$_4$)$_2$ (top) and [Zn(S-thpec9)](ClO$_4$)$_2$ in the presence of NaB(C$_6$H$_5$)$_4$ in ^{2}H$_7$ dimethylformamide (0.1 mol dm^{-3}) at 75.47 MHz (0.1 mol dm^{-3}). The peaks due to the NaB(C$_6$H$_5$)$_4$ are marked with an asterisk (*).

The ROESY spectra of [Zn(S-thpec9)]$^{2+}$ and [Zn(S-thppc9)]$^{2+}$ were recorded in the presence of each of the guest molecules; Na(B(C$_6$H$_5$)$_4$), p-NO$_2$C$_5$H$_4$OH and C$_{10}$H$_{15}$CO$_2$Na in a 1:1 host:guest mole ratio. It was hoped that the some interaction of the aromatic protons of [Zn(S-thpec9)]$^{2+}$ or [Zn(S-thppc9)]$^{2+}$ with protons from each guest would be detected in the form of cross peaks in the ROESY spectra. However, no interaction was observed.

5.4 Electrospray ionisation mass spectrometry

Evidence of host-guest complexation in solution was sought by utilising electrospray ionisation mass spectrometry (ESI-MS) techniques. This technique requires an equilibrated solution containing the host and the guest of interest. This solution is introduced into the ESI mass spectrometer, which transfers the preexisting ions gently into the gas-phase resulting in minimal fragmentation into the ion trap.[3, 4] As the host guest complexes under investigation are all cations in this case, it was anticipated that positive ion ESI-MS may be able to be used to detect their presence in solution. The methanol solutions studied were approximately $1 \times 10\text{-}5$ mol dm^{-3} in host and guest concentraions.

A total of six solutions were studied, each containing equimolar amounts of the host, either $[Zn(S\text{-thpec9})]^{2+}$ or $[Zn(S\text{-thppc9})]^{2+}$, and the guest, either $Na(B(C_6H_5)_4)$, or $p\text{-}NO_2C_5H_4OH$ or $C_{10}H_{15}CO_2Na$. The spectra were found to contain strong positive ion signals due to the zinc(II) complexes, with a m/z 277 for $[Zn(S\text{-thpec9})]^{2+}$ and m/z 298 for $[Zn(S\text{-thppc9})]^{2+}$. The ESI mass spectrum of $[Zn(S\text{-thpec9})]^{2+}$ in the presence of $C_{10}H_{15}CO_2^-$ shows a strong positive ion signal at m/z 732 which is consistent with the presence of $[Zn(S\text{-thpec9})(C_{10}H_{15}CO_2)]^+$ in methanol. None of the other host-guest complexes were detected.

These preliminary host-guest complexation investigations show the potential for ligands such as $S\text{-thpec9}$ and $S\text{-thppc9}$ to act as molecular receptors. However, the evidence for the entry of the guests into the receptor cavity is equivocal at this stage. Further investigations of these and related systems are continuing within our research group.[5, 6]

References

1. C. A. Hunter and J. K. M. Saunders, *Journal of the American Chemical Society*, 1990. **112**, 5525.

2. M. J. Frisch, G. W. Trucks, H. B. Schlegel, P. M. w. Gill, B. G. Johnson, M. A. Robb, J. R. Cheeseman, G. A. P. T. Keith, J. A. Mongomery, K. Raghavachari, M. A. Al-Laham, V. G. Ortiz., J. B. Foresman, J. Ciolowski, B. B. Stefanov, A. Nanayakkara, M. Challacombe, C. Y. Peng, P. Y. Ayala, W. Chen, M. W. Wong, J. L. Andres, E. Replogle, R. Gomperts, R. L. Martin, D. J. Fox, J. S. Binkly, D. J. Defrees, J. Baker, J. P. Stewart, M. Head-Gordon, C. Gonzalez and J. A. Polple, *Gaussian 94, Revision D.3,* . 1994.

3. S. J. Gaskell, *Journal of Mass Spectrometry*, 1997. **32**, 677.

4. R. Colton, S. Mitchell and J. C. Traeger, *Inorganica Chimica Acta*, 1995. **231**, 87.

5. C. B. Smith, K. S. Wallwork, J. M. Weeks, M. A. Buntine, S. F. Lincoln, M. R. Taylor and K. P. Wainwright, *Inorganic Chemistry*, 1999. **38**, 4986.

6. S. L. Whitbread, P. Valente, M. A. Buntine, P. Clements, S. F. Lincoln, M. R. Taylor and K. P. Wainwright, *Journal of the American Chemical Society*, 1998. **43**, 120.

Chapter 6

Experimental

6.1   Synthesis of ligands

6.1.1   1,4,7-Triazacyclononane (tacn)[1]

Preparation of Ethyleneglycol Ditosylate

Ethylene glycol (15.5 g, 0.25 mol) was suspended with rapid stirring in dichloromethane (100 cm^3) and the mixture cooled to less than 5°C. Triethylamine (53 g, 0.52 mol) was added slowly so that the temperature did not exceed 10°C after which tosylchloride (95.1g, 0.5 mol in 300 cm^3 dichloromethane) was added drop wise over a period of *ca* 90 minutes so that the temperature did not exceed 10°C. When the addition was complete, the ice bath was removed and the mixture left to stir over night. The solid white triethylamine hydrochloride was filtered off and the filtrate was reduced in volume by rotary evaporation until crystallisation had begun. Diethylether was then added and the white crystalline product collected by filtration and washed with ethanol and diethylether (71.6% yield).

Preparation of Diethylenetriamine Tritosylate

Triethylamine (78 g, 0.77 mol) was added dropwise to a stirred suspension of diethlylenetriamine (25.8g, 0.25 mol) in dichloromethane (250 cm^3) (previously cooled to below 5°C) so that the temperature did not exceed 10°C. After stirring over night at room temperature, the white solid product was collected and retained, and the filtrate taken to dryness and also retained. The crude white solid was recrystallised from a 95% ethanol solution to yield the pure white crystalline product in 78.4% yield.

Preparation of Disodiumdiethylenetriamine Tritosylate

Sodium metal (13 g, 0.56 mol) was added in small portions to a stirred mixture of diethylenetriamine tritosylate (110g, 0.196mol) in absolute ethanol (1200 cm^3) so that the temperature of the solution did not exceed 35°C. The resulting clear solution was covered and refrigerated over night affording a hydroscopic solid product that was collected and dried under high vacuum (92% yield).

Preparation of 1,4,7-Triazacyclononane Tritosylate

Ethylene glycol ditosylate (66.25 g, 0.179 mol in 250 cm^3 dry distilled DMF) was added dropwise to a stirred solution of disodiumdiethylenetriamine tritosylate (108.85 g, 0.179 mol) in dry distilled dimethylformamide (DMF) (500 cm^3) heated to 65°C. The temperature was then raised to 100°C and stirred overnight. This was then evaporated down until crystallisation began, and vigorously stirred whilst a thin stream of ice cold water (3000 cm^3) was added. After about 30 minutes the solid was collected by filtration and washed with water and absolute ethanol and dried under vacuum (94% yield).

De-Tosylation of 1,4,7-Triazacyclononane Tacntritosylate

1,4,7-Triazacyclononane tritosylate (110 g, 0.118 mol) was refluxed in 90% sulphuric acid solution for three days. The resulting solution was then cooled and poured into a 4/1 volume/volume chloroform/ether solution (1000 cm^3) and the resulting hydroscopic grey solid collected by vacuum filtration under nitrogen. The grey solid (tacn hydrogen sulphate) was dissolved in water (50 cm^3) and hydrobromic acid added causing the precipitation of 1,4,7-triazacyclononane hydrobromide. The white solid product was collected by vacuum filtration, dissolved in water (30 cm^3) and sodium hydroxide pellets added to raise the pH of the solution to 14. This was then azeotropically distilled with benzene and the NaOH removed my filtration and the filtrate evaporated to dryness to afford white solid tacn in 62% yield.

6.1.2 Synthesis of Tris-((2S)-hydroxypropyl)-1,4,7-triazacyclononane (*S*-thpc9)

1,4,7-Triazacyclononane (tacn) was prepared as described in section 5.1.1. *S*-(-)-propylene oxide (0.116 g, 0.002 mol) was added to a solution of tacn (0.079 g, 0.0006 mol) in ethanol (10 cm^3) and left to stir at room temperature overnight. The solution was then evaporated to dryness at reduced pressure and the product obtained as a colourless oil in quantitative yield. ^{13}C NMR in CDCl$_3$ δ 66.4, 63.4, 52.7, 19.8 ppm. (Found: C, 55.78, H, 10.35, N, 13.30 ppm. C$_{15}$H$_{30}$N$_3$O$_3$.1.25.H$_2$O requires C, 55.79, H, 10.14, N, 13.01)

6.1.3 Synthesis of Tris-((2S)-hydroxyphenylethyl)-1,4,7-triazacyclononane (*S*-thpec9)

1,4,7-Triazacyclononane (tacn) was prepared as described in section 5.1.1. *S*-(-)-styrene oxide (0.25 g, 0.002 mol) was added to a solution of triazacyclononane (0.079 g, 0.0006 mol) in dimethylformamide (10 cm^3) and was left to stir at 85°C for three days. Upon cooling to room temperature, methanol (5 cm^3) and water (5 cm^3) were added resulting in the formation of a fine white precipitate which was filtered off, washed with water and dried under vacuum. Yield 0.261 g, 89%. ^{13}C NMR in CDCl$_3$ δ 142.5, 128.3, 127.3, 126.0, 70.7, 67.9, 53.7 ppm. (Found: C, 73.49; H, 8.05, N, 8.56 ppm. C$_{30}$H$_{39}$O$_3$N$_3$ requires C, 73.62; H, 7.98; N, 8.59)

6.1.4 Synthesis of Tris-((2S)-hydroxy-3-phenylpropyl)-1,4,7-triazacyclononane (*S*-thppc9)

S-2,3-epoxypropyl benzene was obtained through the utilisation of a kinetic resolution reaction of 2,3-epoxypropyl benzene using Jacobsen's catayst (0.7%)[2, 3] to assist in the selective hydrolysis of the *R*-2,3-Epoxypropyl benzene enantiomer.

The catalyst, (*S,S*)-(+)-*N,N'*-bis(3,5-di-*tert*-butylsalicylidene)-1,2-cyclohexanne-diaminocobalt(II) (2.6 x 10^{-4} mol, 0.1423 g) was activated by stirring with glacial acetic acid (5.2 x 10^{-4} mol, 0.0313 g) in toluene (5 cm^3) for 1 hour at room temperature after which it was evaporated to dryness under reduced pressure and dried *in vacuo*.

The 2,3-epoxypropyl benzene racemate (0.0373 mol, 5 g) was added to the dry, activated catalyst along with water (0.0205 mol, 0.37 g) and stirred for 16 hours at room temperature. The mixture was taken up in pentane (50 cm^3), washed three times with water and then evaporated to dryness under reduced pressure. The resulting oil was purified by distillation at 17 mm Hg and 98-100° (1.4g, 28% yield).

1,4,7-Triazacyclononane (tacn) was prepared as described in section 5.1.1. *S*-2,3-epoxypropyl benzene (0.116g, 0.002mol) was added to a solution of tacn (0.079 g, 0.0006 mol) in ethanol (10 cm^3) and left to stir at room temperature overnight. The solution was then evaporated to dryness at reduced pressure and the product obtained as a colourless oil in quantitative yield. ^{13}C NMR in CDCl$_3$ δ 138.5, 129.3, 128.1, 126.0, 68.6, 64.5, 53.5, 41.2 ppm. (Found: C, 55.78, H, 10.35, N, 13.30. C$_{15}$H$_{30}$N$_3$O$_3$.1.25.H$_2$O requires C, 55.79, H, 10.14, N, 13.01).

6.2   General

6.2.1 Non-aqueous titrations

Materials

The ligands were prepared according to the procedures described in section 6.1. Methanol (AR) was dried and purified using literature methods.[4] Dimethylformamide was dried with $MgSO_4$, filtered and purified by distillation from anhydrous $CuSO_4$. The water level of both solvents was below the Karl-Fischer detection level of *ca* 50 ppm. The metal salts, A.R. $LiClO_4$, $NaClO_4$, $KClO_4$ (Fluka), were purchased and dried under high vacuum over P_2O_5. $RbClO_4$ and $CsClO_4$ were prepared using previously described methods and dried under high vacuum over P_2O_5.[5]

All $MClO_4$ salts were standardised in triplicate using a Dowex AG 50W-X2 cation exchange column. The column (in its H^+ form) was loaded with an aqueous solution of the metal ion and eluted with purified Milli Q water. The eluent was titrated against a NaOH solution (previously standardised using potassium hydrogen phthalate) to determine the total number of moles of H^+ which allowed for the determination of the total number of moles of the metal ion since one mole of metal(I) salt displaces one mole of protons from the column.

Tetraethylammonium perchlorate (NEt_4ClO_4) was prepared by the addition of $HClO_4$ (1.0 mol dm^{-3}, 1.7 dm^3) to NEt_4Br (300 g) (Aldrich) in H_2O (500 cm^3). The resulting white precipitate was recrystallised from H_2O until it was free of bromide and acid. The crystalline white NEt_4ClO_4 was dried under high vacuum over P_2O_5.

All solutions were prepared in 0.05 M NEt_4ClO_4 supporting electrolyte in the appropriate solvent.

Measurements

Potentiometric titrations were carried out under dry nitrogen in a titration vessel connected to a reference vessel by salt bridge containing 0.05 M NEt_4ClO_4 electrolyte in the appropriate solvent. The reference cell contained a reference solution of 20 cm^3 of 0.01 M $AgNO_3$ in the appropriate solvent and a silver wire reference electrode. A silver wire electrode was also used to monitor the Ag^+ concentration in the sample vessel. The vessels were kept at a constant temperature of 298.2 ± 0.1 by an outer water jacket through which water was circulated from a thermostatted water bath. High purity nitrogen was bubbled through a solution of 0.05 M NEt_4ClO_4 in the appropriate solvent (to saturate the nitrogen) and then through the solution in the sample cell to exclude atmospheric gases and moisture. The potential readings during the titration were monitored by an Orion Research 720 Digital voltmeter.

The electrode response to silver ion concentration was determined by a titration of a solution of known concentration and measuring the corresponding potential. The electrode response to metal ion concentration is pseudo Nerstian, and is given by Equation 5.1

$$E = E_0 + Cln[M^+]$$ **5.1**

E_0 (the standard electrode potential) and C (a constant typifying the equilibrium studied) were determined from a linear plot of the potential, E (mV) against the logarithm of the silver concentration, $ln[Ag^+]$.

The stability constants for $[AgL]^+$, where L = *S*-thpc9, *S*-thpec9 and *S*-thppc9, were determined in duplicate by the direct titration of 0.001 mol dm^{-3} ligand (5 cm^3) into 0.0001 mol dm^{-3} $AgNO_3$ (20 cm^3) in the appropriate solvent. Stability constants of $[ML]^+$, where M = Li^+, Na^+, K^+, Rb^+ and Cs^+ where determined in duplicate by the competitive titration of a solution containing ligand (0.001 mol dm^{-3}) of metal salt (0.005 mol dm^{-3}) into $AgNO_3$ (0.001 mol dm^{-3}). The stability constants for $[ML]^+$ were then determined from the data using the VISP program as described in Chapter 7.[6]

6.2.2 NMR Spectroscopy

6.2.2.1   Variable Temperature 13C NMR

Materials

The ligands were prepared according to the procedures described in section 6.1. The metal salts, $LiClO_4$, $NaClO_4$ and $ZnClO_4$ were dried under high vacuum before use. ^{12}C enriched $^2H_4$ methanol (99.95 atom % ^{12}C and 99.5% ^2H, Aldrich), $CDCl_3$ (99.8% ^2H, Aldrich) and $^2H_7$ DMF (99.5% ^2H, Aldrich) were used and stored under nitrogen over the appropriate molecular sieves. ^{12}C enriched $^2H_4$ methanol was used to avoid problems of overlap between the ^{13}C NMR resonances of the complex and those arising from $^2H_4$ methanol.

Measurements

Broad-band ^1H decoupled ^{13}C variable temperature NMR were carried out on a Bruker ACP-300 that was modified by Varian to a Gemini 2000 system, using the original Bruker magnet operating at 300.145 MHz (^1H) or 75.4 MHz (^{13}C). The sample temperature was controlled to within ± 0.03 K using a Bruker B-VT 1000 variable temperature unit that was calibrated using the temperature dependence of the ^1H chemical shifts of neat ethylene glycol (for the temperature range 300-360 K) and neat methanol (for the temperature range 190-300 K).[7, 8] The samples were equilibrated for 20 minutes at each temperature. The data was then subject to a complete lineshape analysis (see Chapter 4) using the FORTRAN-77 program LINSHP[6] to determine the kinetic parameters characterising the exchange process.

6.2.2.2   2D ROESY NMR

Materials

S-thpc9, S-thpec9 and S-thppc9 were prepared as described in section 5.1. Sodium adamantanecarboxylate was prepared by the addition of NaOH to an aqueous solution of adamantanecarboxylic acid (99 %, Aldrich) and crashed out of solution by the drop wise addition of ethanol. The white precipitate was collected and dried under vacuum. Sodium tetraphenylborate and *p*-nitrophenol were commercially available (Aldrich) and the later compound recrystallised before use from 0.1 M aqueous hydrochloric acid (HCl). All compounds were dried under high vacuum before use. All solutions were prepared at 0.1 M concentration in $^2H_7$ dimethylformamide with equimolar amounts of ligand, metal and guest.

All 2-D ROESY NMR spectra were recorded on a Varian Inova 600 Spectrometer operating at 599.957 MHz using a standard sequence with a mixing time of 0.3 seconds. The samples contained equimolar amounts of ligand, metal and guest in $^2H_7$ dimethylformamide at an approximate concentration of 0.1 mol dm^{-3}.

6.2.3 Electrospray ionisation mass spectrometry (ESI-MS)

Materials

The ESI-MS sample solutions were prepared in HPLC grade methanol (Aldrich). The ligands were prepared as described in section 5.1. The guest molecules were prepared as described in section 5.2.2. All compounds were dried under vacuum before use. Each sample solution contained metal, ligand and guest with a 1:1:1 and 1:1:2 metal:ligand:guest ratios for all systems studied at an approximate concentration of 1 x 10^{-6} mol dm^{-3}.

Measurements

A Finnigan MAT ion trap LC-Q (Finnigan, San Jose, CA, USA) octapole mass spectrometer fitted with an electrospray ionisation (ESI) source was used. Nitrogen was used as the nebulising gas. The electrospray needle was maintained at 4.25 kV and the capillary temperature maintained at 200°C. The tube lens offset was set at 30V and the capillary voltage was maintained at 35 V. The sample solutions were introduced into the ESI source in positive ion mode by infusion at flow rates of 12-18 μL per minute using a syringe.

6.2.4 Molecular Modelling

Molecular orbital calculations were carried out using the Gaussian 94[9] program with the LANL2DZ, LANL2MB, STO-3G** or 2-31G basis sets[10,11] on a Silicon Graphics Power Challenge work station. MOLDEN software was used to visualise the molecules.

References

1. R. Yang and L. J. Zompa, *Inorganic Chemistry*, 1976. **15**, 1499.

2. R. B. Pettman, *Specialty Chemicals*, 1996, 118.

3. M. Tokunaga, J. F. Larrow, F. Kakiuchi and E. N. Jacobsen, *Science*, 1997. **277**, 936.

4. D. D. Perrin, W. L. F. Aramego and D. R. Perrin, *Purification of Laboratory Chemicals*. 2nd ed. 1980, Oxford, U.K.: Pergamon.

5. A. K. W. Stephens and S. F. Lincoln, *Journal of the Chemical Society, Dalton Transactions*, 1993, 2123.

6. P. Clarke, *Ph. D Thesis*, 1992, The University of Adelaide: Adelaide.

7. A. L. V. Geet, *Analytical Chemistry*, 1970. **42**, 679.

8. D. S. Raiford, C. L. Fisk and E. D. Becker, *Analytical Chemistry*, 1979. **51**, 2050.

9. M. J. Frisch, G. W. Trucks, H. B. Schlegel, P. M. w. Gill, B. G. Johnson, M. A. Robb, J. R. Cheeseman, G. A. P. T. Keith, J. A. Mongomery, K. Raghavachari, M. A. Al-Laham, V. G. Ortiz., J. B. Foresman, J. Ciolowski, B. B. Stefanov, A. Nanayakkara, M. Challacombe, C. Y. Peng, P. Y. Ayala, W. Chen, M. W. Wong, J. L. Andres, E. Replogle, R. Gomperts, R. L. Martin, D. J. Fox, J. S. Binkly, D. J. Defrees, J. Baker, J. P. Stewart, M. Head-Gordon, C. Gonzalez and J. A. Polple, *Gaussian 94, Revision D.3*, .

10. M. J. Frisch, A. Frisch and J. B. Foresman, *Gaussian 94 User's Reference*. 1995, Pittsburgh: Gaussian Inc.

11. J. B. Foresman and A. Frisch, *Exploring Chemistry with Electronic Structure Methods*. 2 ed. 1993, Pittsburgh: Gaussian Inc.

Appendix (i)

Intramolecular bond distances and angles in the X-ray crystal structure of [Zn(S-thpc9)]1.5ClO$_4$.0.5Cl.

Intramolecular Distances Involving the Nonhydrogen Atoms

atom	atom	distance	ADC(*)	atom	atom	distance	ADC(*)
ZN	O1	2.167(5)	1	N1	C9	1.49(1)	1
ZN	O4	2.110(5)	1	N1	C10	1.505(9)	1
ZN	O7	2.119(5)	1	N4	C3	1.50(1)	1
ZN	N1	2.128(4)	1	N4	C5	1.469(9)	1
ZN	N4	2.168(6)	1	N4	C13	1.45(1)	1
ZN	N7	2.175(5)	1	N7	C6	1.51(1)	1
CL1	O11	1.422(5)	1	N7	C8	1.503(9)	1
CL1	O12	1.356(9)	1	N7	C16	1.477(8)	1
CL1	O13	1.466(7)	1	C2	C3	1.49(1)	1
CL1	O14	1.412(6)	1	C5	C6	1.48(1)	1
CL2	O15	1.380(8)	1	C8	C9	1.44(1)	1
CL2	O15	1.380(8)	55602	C10	C11	1.51(1)	1
CL2	O16	1.32(2)	1	C11	C12	1.51(1)	1
CL2	O16	1.32(2)	55602	C13	C14	1.56(1)	1
O1	C11	1.467(8)	1	C14	C15	1.47(1)	1
O4	C14	1.445(9)	1	C16	C17	1.493(9)	1
O7	C17	1.431(8)	1	C17	C18	1.497(9)	1
N1	C2	1.47(1)	1				

Intramolecular Bond Angles Involving the Nonhydrogen Atoms

atom	atom	atom	angle	atom	atom	atom	angle
O1	ZN	O4	87.8(2)	O16	CL2	O16	101(2)
O1	ZN	O7	82.6(2)	ZN	O1	C11	114.5(4)
O1	ZN	N1	78.6(2)	ZN	O4	C14	117.2(4)
O1	ZN	N4	141.0(2)	ZN	O7	C17	110.9(4)
O1	ZN	N7	128.1(2)	ZN	N1	C2	111.0(4)
O4	ZN	O7	89.0(2)	ZN	N1	C9	102.4(4)
O4	ZN	N1	127.5(2)	ZN	N1	C10	108.9(4)
O4	ZN	N4	78.1(2)	C2	N1	C9	112.8(6)
O4	ZN	N7	140.0(2)	C2	N1	C10	107.9(6)
O7	ZN	N1	137.6(2)	C9	N1	C10	113.8(5)
O7	ZN	N4	132.5(2)	ZN	N4	C3	102.7(4)
O7	ZN	N7	80.2(2)	ZN	N4	C5	109.9(4)
N1	ZN	N4	81.6(2)	ZN	N4	C13	108.2(4)
N1	ZN	N7	82.1(2)	C3	N4	C5	111.9(6)
N4	ZN	N7	81.3(2)	C3	N4	C13	113.9(6)
O11	CL1	O12	110.4(5)	C5	N4	C13	109.9(6)
O11	CL1	O13	107.4(4)	ZN	N7	C6	104.2(4)
O11	CL1	O14	110.3(4)	ZN	N7	C8	107.4(4)
O12	CL1	O13	106.6(5)	ZN	N7	C16	107.3(4)
O12	CL1	O14	115.4(6)	C6	N7	C8	113.8(5)
O13	CL1	O14	106.3(4)	C6	N7	C16	111.4(5)
O15	CL2	O15	109.0(7)	C8	N7	C16	112.0(5)
O15	CL2	O16	116(1)	N1	C2	C3	111.7(6)
O15	CL2	O16	107(1)	N4	C3	C2	111.4(6)
O15	CL2	O16	107(1)	N4	C5	C6	113.8(6)
O15	CL2	O16	116(1)	N7	C6	C5	111.3(6)
N7	C8	C9	112.9(6)				
N1	C9	C8	113.7(6)				
N1	C10	C11	110.9(5)				

Appendix (ii)

Intramolecular bond distances and angles in the X-ray crystal structure of S-thpec9.

Intramolecular Distances Involving the Nonhydrogen Atoms

atom	atom	distance	atom	atom	distance
O(1)	C(12)	1.447(9)	C(5a)	C(6b)	1.56(2)
O(4)	C(42)	1.41(1)	C(5a)	C(6a)	0.86(2)
O(7)	C(72)	1.42(1)	C(5b)	C(6a)	1.61(2)
N(1)	C(2b)	1.59(2)	C(6b)	C(6a)	0.83(2)
N(1)	C(2a)	1.36(2)	C(6b)	C(8b)	1.70(3)
N(1)	C(9a)	1.37(2)	C(8b)	C(8a)	0.98(2)
N(1)	C(9b)	1.61(2)	C(8b)	C(9a)	1.76(3)
N(1)	C(11)	1.44(1)	C(8b)	C(9b)	1.56(3)
N(4)	C(3a)	1.34(2)	C(8a)	C(9a)	1.52(2)
N(4)	C(3b)	1.73(2)	C(8a)	C(9b)	0.97(2)
N(4)	C(5a)	1.70(2)	C(9a)	C(9b)	0.70(2)
N(4)	C(5b)	1.35(2)	C(11)	C(12)	1.54(1)
N(4)	C(41)	1.45(1)	C(12)	C(13)	1.49(1)
N(7)	C(6b)	1.28(2)	C(13)	C(14)	1.41(1)
N(7)	C(6a)	1.69(2)	C(13)	C(18)	1.39(1)
N(7)	C(8b)	1.38(2)	C(14)	C(15)	1.38(1)
N(7)	C(8a)	1.67(2)	C(15)	C(16)	1.38(1)
N(7)	C(71)	1.50(1)	C(16)	C(17)	1.41(1)
C(2b)	C(2a)	0.73(2)	C(17)	C(18)	1.36(1)
C(2b)	C(3a)	1.60(2)	C(41)	C(42)	1.51(1)
C(2b)	C(3b)	0.90(2)	C(42)	C(43)	1.52(1)
C(2a)	C(3a)	1.85(2)	C(43)	C(44)	1.37(1)
C(2a)	C(3b)	1.48(3)	C(43)	C(48)	1.41(1)
C(3a)	C(3b)	0.98(2)	C(44)	C(45)	1.42(1)
C(3a)	C(5b)	1.58(2)	C(45)	C(46)	1.38(1)

C(5a)	C(5b)	1.08(2)		C(46)	C(47)	1.36(1)
C(47)	C(48)	1.38(1)				
C(71)	C(72)	1.52(1)				
C(72)	C(73)	1.53(1)				
C(73)	C(74)	1.39(1)				
C(73)	C(78)	1.35(1)				
C(74)	C(75)	1.40(1)				
C(75)	C(76)	1.36(1)				
C(76)	C(77)	1.39(1)				
C(77)	C(78)	1.40(1)				

Intramolecular Bond Angles Involving the Nonhydrogen Atoms

atom	atom	atom	angle	atom	atom	atom	angle
C(2b)	N(1)	C(2a)	27.1(9)	C(6a)	N(7)	C(71)	108.1(9)
C(2b)	N(1)	C(9a)	118(1)	C(8b)	N(7)	C(8a)	35.8(9)
C(2b)	N(1)	C(9b)	142(1)	C(8b)	N(7)	C(71)	114(1)
C(2b)	N(1)	C(11)	108.4(8)	C(8a)	N(7)	C(71)	103.8(9)
C(2a)	N(1)	C(9a)	91(1)	N(1)	C(2b)	C(2a)	58(2)
C(2a)	N(1)	C(9b)	117(1)	N(1)	C(2b)	C(3a)	108(1)
C(2a)	N(1)	C(11)	125(1)	N(1)	C(2b)	C(3b)	127(2)
C(9a)	N(1)	C(9b)	25.5(9)	C(2a)	C(2b)	C(3a)	98(3)
C(9a)	N(1)	C(11)	124(1)	C(2a)	C(2b)	C(3b)	130(3)
C(9b)	N(1)	C(11)	107.0(9)	C(3a)	C(2b)	C(3b)	33(1)
C(3a)	N(4)	C(3b)	34.3(8)	N(1)	C(2a)	C(2b)	94(2)
C(3a)	N(4)	C(5a)	111(1)	N(1)	C(2a)	C(3a)	107(1)
C(3a)	N(4)	C(5b)	72(1)	N(1)	C(2a)	C(3b)	105(2)
C(3a)	N(4)	C(41)	113(1)	C(2b)	C(2a)	C(3a)	59(2)
C(3b)	N(4)	C(5a)	140(1)	C(2b)	C(2a)	C(3b)	28(2)
C(3b)	N(4)	C(5b)	105(1)	C(3a)	C(2a)	C(3b)	31.9(8)
C(3b)	N(4)	C(41)	107.9(9)	N(4)	C(3a)	C(2b)	106(1)
C(5a)	N(4)	C(5b)	39.7(9)	N(4)	C(3a)	C(2a)	116(1)
C(5a)	N(4)	C(41)	104.7(9)	N(4)	C(3a)	C(3b)	95(2)
C(5b)	N(4)	C(41)	112(1)	N(4)	C(3a)	C(5b)	54(1)
C(6b)	N(7)	C(6a)	28.5(9)	C(2b)	C(3a)	C(2a)	23.0(7)
C(6b)	N(7)	C(8b)	79(1)	C(2b)	C(3a)	C(3b)	30(1)
C(6b)	N(7)	C(8a)	115(1)	C(2b)	C(3a)	C(5b)	136(1)
C(6b)	N(7)	C(71)	113(1)	C(2a)	C(3a)	C(3b)	53(2)
C(6a)	N(7)	C(8b)	107(1)	C(2a)	C(3a)	C(5b)	123(1)

C(6a)	N(7)	C(8a)	139.7(9)	C(3b)	C(3a)	C(5b)	146(2)
N(4)	C(3b)	C(2b)	125(2)	N(7)	C(6a)	C(6b)	47(2)
N(4)	C(3b)	C(2a)	116(1)	C(5a)	C(6a)	C(5b)	39(2)
N(4)	C(3b)	C(3a)	51(1)	C(5a)	C(6a)	C(6b)	135(3)
C(2b)	C(3b)	C(2a)	22(2)	C(5b)	C(6a)	C(6b)	96(2)
C(2b)	C(3b)	C(3a)	117(3)	N(7)	C(8b)	C(6b)	47.5(9)
C(2a)	C(3b)	C(3a)	95(2)	N(7)	C(8b)	C(8a)	88(2)
N(4)	C(5a)	C(5b)	53(1)	N(7)	C(8b)	C(9a)	112(1)
N(4)	C(5a)	C(6b)	113(1)	N(7)	C(8b)	C(9b)	103(2)
N(4)	C(5a)	C(6a)	131(2)	C(6b)	C(8b)	C(8a)	135(2)
C(5b)	C(5a)	C(6b)	89(2)	C(6b)	C(8b)	C(9a)	121(1)
C(5b)	C(5a)	C(6a)	111(2)	C(6b)	C(8b)	C(9b)	131(2)
C(6b)	C(5a)	C(6a)	22(2)	C(8a)	C(8b)	C(9a)	60(1)
N(4)	C(5b)	C(3a)	53.8(9)	C(8a)	C(8b)	C(9b)	36(1)
N(4)	C(5b)	C(5a)	87(2)	C(9a)	C(8b)	C(9b)	23.4(9)
N(4)	C(5b)	C(6a)	105(1)	N(7)	C(8a)	C(8b)	56(2)
C(3a)	C(5b)	C(5a)	139(2)	N(7)	C(8a)	C(9a)	110(1)
C(3a)	C(5b)	C(6a)	139(1)	N(7)	C(8a)	C(9b)	120(2)
C(5a)	C(5b)	C(6a)	30(1)	C(8b)	C(8a)	C(9a)	87(2)
N(7)	C(6b)	C(5a)	110(1)	C(8b)	C(8a)	C(9b)	107(2)
N(7)	C(6b)	C(6a)	104(2)	C(9a)	C(8a)	C(9b)	21(2)
N(7)	C(6b)	C(8b)	53(1)	N(1)	C(9a)	C(8b)	113(1)
C(5a)	C(6b)	C(6a)	23(2)	N(1)	C(9a)	C(8a)	109(1)
C(5a)	C(6b)	C(8b)	142(1)	N(1)	C(9a)	C(9b)	97(3)
C(6a)	C(6b)	C(8b)	153(2)	C(8b)	C(9a)	C(8a)	33.8(8)
N(7)	C(6a)	C(5a)	130(2)	C(8b)	C(9a)	C(9b)	63(2)
N(7)	C(6a)	C(5b)	114(1)	C(8a)	C(9a)	C(9b)	29(2)

N(1)	C(9b)	C(8b)	111(1)
N(1)	C(9b)	C(8a)	130(2)
N(1)	C(9b)	C(9a)	57(2)
C(8b)	C(9b)	C(8a)	37(1)
C(8b)	C(9b)	C(9a)	94(3)
C(8a)	C(9b)	C(9a)	131(4)
N(1)	C(11)	C(12)	110.3(6)
O(1)	C(12)	C(11)	108.6(6)
O(1)	C(12)	C(13)	109.7(7)
C(11)	C(12)	C(13)	116.5(6)
C(12)	C(13)	C(14)	122.5(8)
C(12)	C(13)	C(18)	119.5(7)
C(14)	C(13)	C(18)	117.9(8)
C(13)	C(14)	C(15)	120.7(8)
C(14)	C(15)	C(16)	120.8(8)
C(15)	C(16)	C(17)	118.3(8)
C(16)	C(17)	C(18)	121.2(9)
C(13)	C(18)	C(17)	121.1(8)
N(4)	C(41)	C(42)	116.4(8)
O(4)	C(42)	C(41)	112.5(7)
O(4)	C(42)	C(43)	108.1(7)
C(41)	C(42)	C(43)	108.4(7)
C(42)	C(43)	C(44)	123.1(8)
C(42)	C(43)	C(48)	118.9(8)
C(44)	C(43)	C(48)	117.9(8)
C(43)	C(44)	C(45)	121.6(8)

C(44)	C(45)	C(46)	118.4(9)
C(45)	C(46)	C(47)	120.5(9)
C(46)	C(47)	C(48)	121.4(9)
C(43)	C(48)	C(47)	120.2(9)
N(7)	C(71)	C(72)	110.9(8)
O(7)	C(72)	C(71)	109.2(7)
O(7)	C(72)	C(73)	108.9(7)
C(71)	C(72)	C(73)	109.3(7)
C(72)	C(73)	C(74)	119.0(7)
C(72)	C(73)	C(78)	121.4(7)
C(74)	C(73)	C(78)	119.5(8)
C(73)	C(74)	C(75)	119.2(8)
C(74)	C(75)	C(76)	120.3(8)
C(75)	C(76)	C(77)	120.7(8)
C(76)	C(77)	C(78)	118.5(8)
C(73)	C(78)	C(77)	121.5(8)

List of Publications

1999 Metal Ion Activated Supramolecular Receptors. C. Smith, K. S. Wallwork, J. M. Weeks, M. A. Buntine, S. F. Lincoln, M. R. Taylor and K. P. Wainwright, Inorganic Chemistry, 1999, **38**, 4986.

1997 Formation Constants for Complexes of 1,4,7,10-Tetraazacyclododecane-1,7-diacetic acid and the Crystal Structure of its Nickel(II) complex. J. M. Weeks, M. R. Taylor and K. P. Wainwright, *Journal of the Chemical Society, Dalton Transactions,* 1997, **50**, 853.

1997 Enantiomerisation of Pendant Arm Triaza Macrocyclic Lithium(I) and Sodium(I) Complex Ions. S. L. Whitbread, J. M. Weeks. P. Valente, M. A. Buntine, S. F. Lincoln, and K. P. Wainwright, *Australian Journal of Chemistry,* 1997, **50**, 853.